Three-dimensional modelling of Venus photochemistry and clouds

Aurélien Stolzenbach, Franck Lefèvre, Sébastien Lebonnois, Anni Määttänen

Three-dimensional modelling of Venus photochemistry and clouds

Aurélien Stolzenbach[a,c,*], Franck Lefèvre[a], Sébastien Lebonnois[b], Anni Määttänen[a]

[a]*LATMOS, Sorbonne Université, UVSQ Paris-Saclay, CNRS, Paris, France*
[b]*Laboratoire de Météorologie Dynamique, Sorbonne Université, ENS, PSL Research University, École Polytechnique, Institut Polytechnique de Paris, CNRS, Paris, France*
[c]*Instituto de Astrofisica de Andalucia (IAA/CSIC), Granada, Spain*

Abstract

We present here three-dimensional simulations of the Venus photochemistry and clouds from the ground to the bottom of the thermosphere. For that purpose, we have implemented a state-of-the-art photochemical and equilibrium cloud model in the Venus Planetary Climate Model (Venus PCM). The interactive coupling between dynamics, radiation, chemistry and clouds allows a comprehensive description of the CO_2, CO, sulfur, chlorine, oxygen, and hydrogen species, with tracking of the condensed phase. Regarding the clouds, the Venus PCM calculates the composition, number density, and sedimentation rates of the binary H_2SO_4-H_2O liquid aerosols, based on observed altitude-dependent size distributions. The article describes in detail the new components implemented in the Venus PCM. It then presents an overview of the results concerning clouds and atmospheric chemistry, which are compared with a wide range of observations. The modeled cloud characteristics and vertical profiles of minor species are found to be in broad agreement with most of the measurements available between 30 and 100 km. In particular, the Venus PCM reproduces the steep decrease of H_2O and SO_2 mixing ratio inside the cloud layer, as well as the observed vertical distribution of species well identified above the clouds, such as CO and O_3. The model also agrees with the ground-based measurements of HCl, but not with the conflicting HCl vertical profiles derived from *Venus Express*. On the quasi-horizontal plane, latitudinal contrasts in the modeled trace species mostly result from the Hadley-type mean meridional circulation. Large-scale longitudinal variations are essentially created by the diurnal thermal tide above the clouds, and by photolysis above 80 km.

Keywords: Venus, photochemistry, GCM, clouds, modelling, sedimentation

1. Introduction

Owing to its fascinating richness and complexity, modelling the photochemistry of Venus is a difficult task. Some of the challenges still facing current models include the diversity of the chemical families involved, the key role attributed to species not yet measured in the atmosphere, or the incomplete knowledge of the kinetics. Added to this is the thick global cloud cover of Venus, at the origin of strong variations in the chemical composition between the lower and upper atmosphere, which remain poorly understood. The most notable efforts of the modelling community started with the early works of Prinn (1971) and McElroy et al. (1973), who tackled the issue of the CO_2 stability, followed by the studies of Winick and Stewart (1980) and Yung and DeMore (1982), focusing on the implications of the discovery of SO_2, and in the last two decades by the extensive work of V. Krasnopolsky (Krasnopolsky, 2007, 2012b, 2013, 2015, 2018) and the teams using the 1D JPL/Caltech model (Mills, 1998; Zhang et al., 2012; Parkinson et al., 2015; Bierson and Zhang, 2020; Shao et al., 2020, 2022). These studies have highlighted some of the issues that remain unsolved in Venus atmospheric science, such as the photochemical stability of CO_2, the non-detection of ground-state O_2, or the vertical distribution and time variability of SO_2. All the models cited above are 1-dimensional (vertical axis only) models. Owing to their low computational cost, these models are the ideal tools to test numerous hypothesis over long timescales. However, by nature, 1D models are unable to describe complex dynamical patterns or latitudinal

*Corresponding author (Aurélien Stolzenbach) aurelien.stolzenbach@latmos.ipsl.fr

variations. Moreover, up to now, the condensed species (H_2O and H_2SO_4) and the Venus clouds have most of the time been treated in an oversimplified way in photochemical models. We propose here, as a complementary approach to 1D models, to couple a model of photochemistry and clouds to a Venus Planetary Climate Model (named hereafter Venus PCM and formely known as the IPSL Venus Global Climate Model (IPSL VGCM) detailed in Lebonnois et al. (2010)). The resulting model is therefore capable, for the first time on Venus, of rendering the chemistry and three-dimensional transport of minor species in a consistent manner from the ground to the top of the atmosphere. In addition, it allows a complete monitoring of the composition of Venusian clouds and their interaction with the gas phase. The new modelling tool presented here has already been used, although not described in detail, by Gilli et al. (2021) and Navarro et al. (2021) who focused on key species in the thermosphere (> 100 km). The present paper provides a comprehensive description of the photochemical and cloud modules implemented in the Venus PCM. We then present an overview of the model results obtained below 100 km, which are compared to a wide range of observations covering all chemical families.

2. Model description

2.1. The Venus Planetary Climate Model

The Venus Planetary Climate Model (Venus PCM) is based on the dynamical core developed at *Laboratoire de Météorologie Dynamique* (LMD) (Hourdin et al., 2006). We use here the version described by Lebonnois et al. (2010), which evaluates the discrete dynamic equations on an horizontal grid divided into 48 longitudes and 32 latitudes, giving a resolution of $7.5° \times 5.625°$. The vertical grid is made of 50 hybrid pressure levels that take into account the topography. With this resolution, the Venus PCM covers altitudes from the ground of Venus to around 95 km. Thus, in the version used here, the model does not cover the thermosphere where airglows and related phenomena occur.

The radiative transfer module calculates the heating rates derived by means of a pre-computed solar flux file depending on solar zenith angle (0° to 95°) and based on data by Crisp (1986). Interpolation is made at each point of the Venus PCM grid to calculate the solar flux and thus takes into account the daily cycle. For thermal radiation, the radiative transfer model uses the Net Exchange Rate method (Eymet et al., 2009). The cloud and haze vertical distribution in the radiative transfer calculations are fixed in latitude and longitude and extend from 47 to 84 km in altitude.

The ability of the Venus PCM to reproduce the observed characteristics of the Venus atmosphere is fully discussed in Lebonnois et al. (2010). Though updates have been made since 2010, which improve the fit to observations and our understanding of the atmospheric dynamics (Lebonnois et al., 2016; Gilli et al., 2017; Garate-Lopez and Lebonnois, 2018), the results presented here were obtained with the Lebonnois et al. (2010) configuration. The impact on the results is limited, as these are mainly related to robust dynamical features obtained in all configurations. In summary, the Venus PCM is able to reproduce the so-called super-rotation of the atmosphere but the attained wind speed in the version described by Lebonnois et al. (2010) was lower than in the observations by Schubert (1983); Gierasch et al. (1997); Limaye (2007); Peralta et al. (2007); Sánchez-Lavega et al. (2008) and Khatuntsev et al. (2013, 2017). In order to correct this bias, the Exchange Rate matrix used to compute the radiative transfer was updated in the present work. These improvements lead the maximal zonal velocity to be close to $120\,\mathrm{m\,s^{-1}}$ between $60 - 80$ km (Fig. 1), in better agreement with the observations. The mass stream function (Fig. 1) as calculated by the model reveals a mean meridional circulation that consists essentially in equator-to-pole Hadley-type cells. The upward branch of the cells is located at the equator and the downward branch at $70 - 80°$ of latitude (in both hemispheres). We note a layered structure in the meridional circulation, with three different Hadley-type cells organized respectively in the deep atmosphere (below 45 km), in the cloud layers (45 −60 km), and in the mesosphere (above 60 km). The Venus PCM reproduces the temperature profile (see Fig. 2 and Fig. 3) with a reasonable deviation of $\pm 10 - 30$ K relative to the observations (Seiff et al., 1985; Zasova et al., 2006).

Fig. 2 plots the Venus PCM zonally-averaged temperature field, whereas the difference with the VIRA climatology (Seiff et al., 1985; Zasova et al., 2006) is shown in Fig. 3. With the version of the Venus PCM used here, the model is 10-30 K warmer than VIRA in the mesosphere (pressure levels smaller than 10^4 Pa), except at high latitudes where the model is 10-20 K colder than the climatology. In the lower atmosphere, the Venus PCM is colder than VIRA by about 20-30K. The atmospheric scale height is therefore lower in the model than in the climatology. Subsequently, for a given altitude level, the number density is smaller in the model than in VIRA, as shown in Fig. 4 above 40 km.

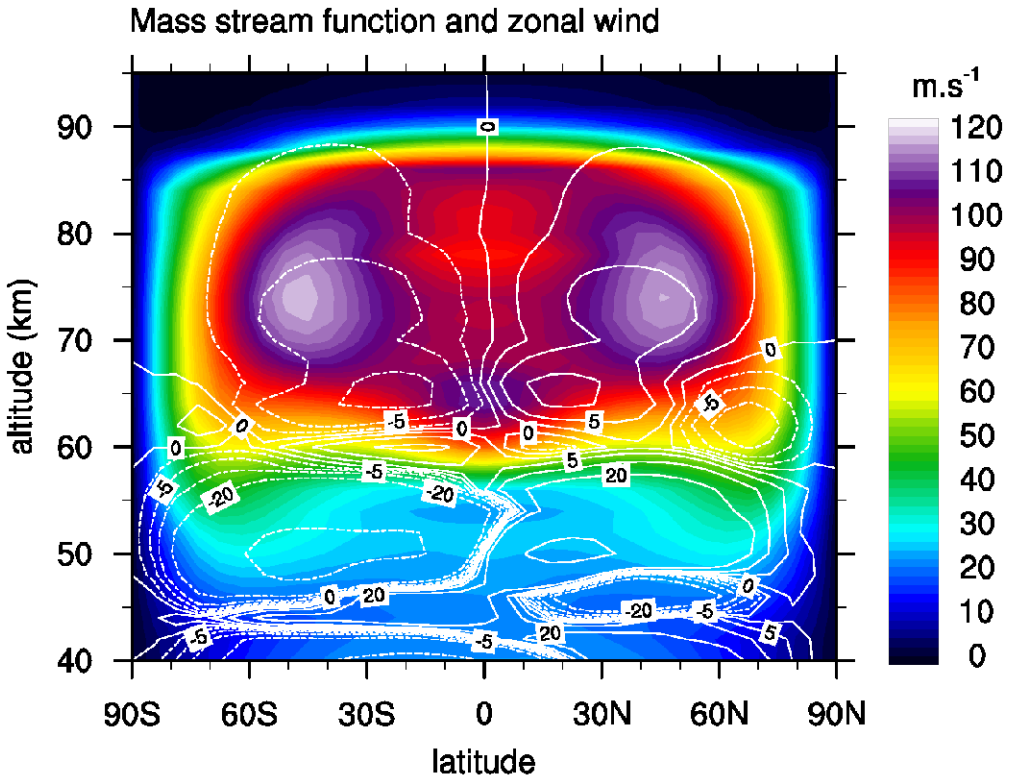

Figure 1: Venus PCM zonal wind ($m\,s^{-1}$). The mass stream function ($kg\,s^{-1}$) is represented by the white isolines (plain and dotted for positive and negative values, respectively).

Another consequence is that when expressed in altitude coordinates, the temperature around 50 km in the model is lower than VIRA by almost 50 K and the cloud base is located about 5 km lower (42 km vs. 47 km) than in the observations (see Section 3.1).

2.2. Photochemical model : gas-phase chemistry

The photochemical model describes the comprehensive chemistries of CO_2, CO, hydrogen, oxygen, chlorine and sulfur down to roughly 35 km. The deep atmosphere chemical timescales are orders of magnitudes longer and the thermochemistry is usually described in separate models (Krasnopolsky, 2007, 2013) even if a recent attempt to a full vertical domain 1D models were made by Bierson and Zhang (2020). When available, the reaction rates and ultraviolet absorption cross sections are taken in the Venus PCM from the JPL compilation (Burkholder et al., 2015) and references within. For the reactions not present in Burkholder et al. (2015), we have in general adopted the kinetics data used in well-established one-dimensional models of Venus photochemistry (Mills, 1998; Krasnopolsky, 2007, 2012b; Zhang et al., 2012; Bierson and Zhang, 2020) in order to facilitate the comparison with results published in the literature. At the present time, the chemistry of nitrogen is not implemented in the photochemical model. Indeed, a credible description of the nitrogen chemistry requires the computation of the N_2 photolysis, which occurs above the top of the Venus PCM in its version presented here (95 km).

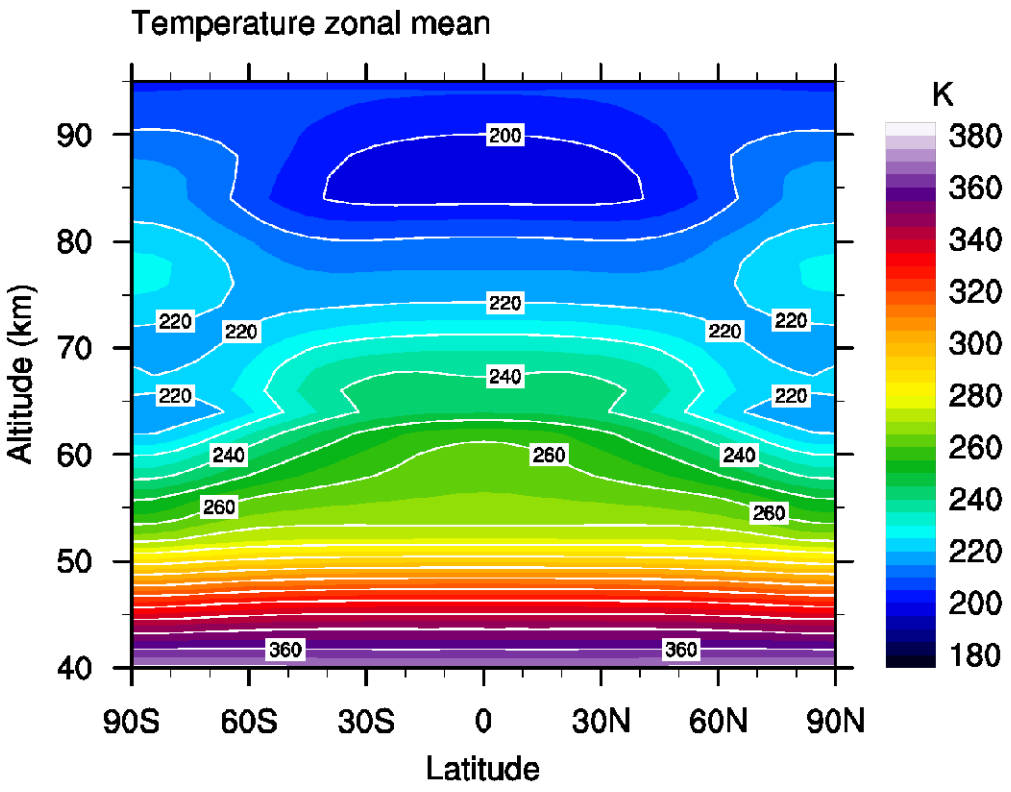

Figure 2: Venus PCM temperature zonal mean (K).

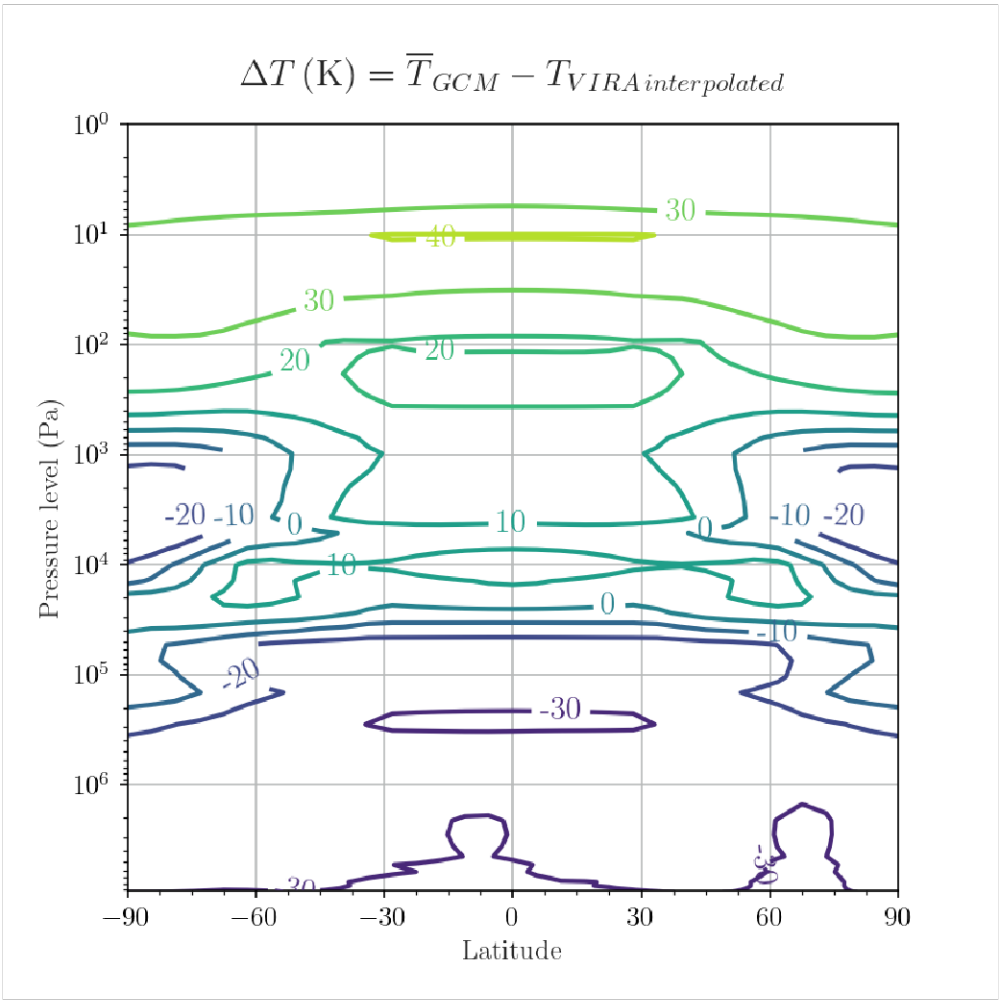

Figure 3: Temperature difference between the Venus PCM and the VIRA climatology, shown here in pressure vertical coordinate.

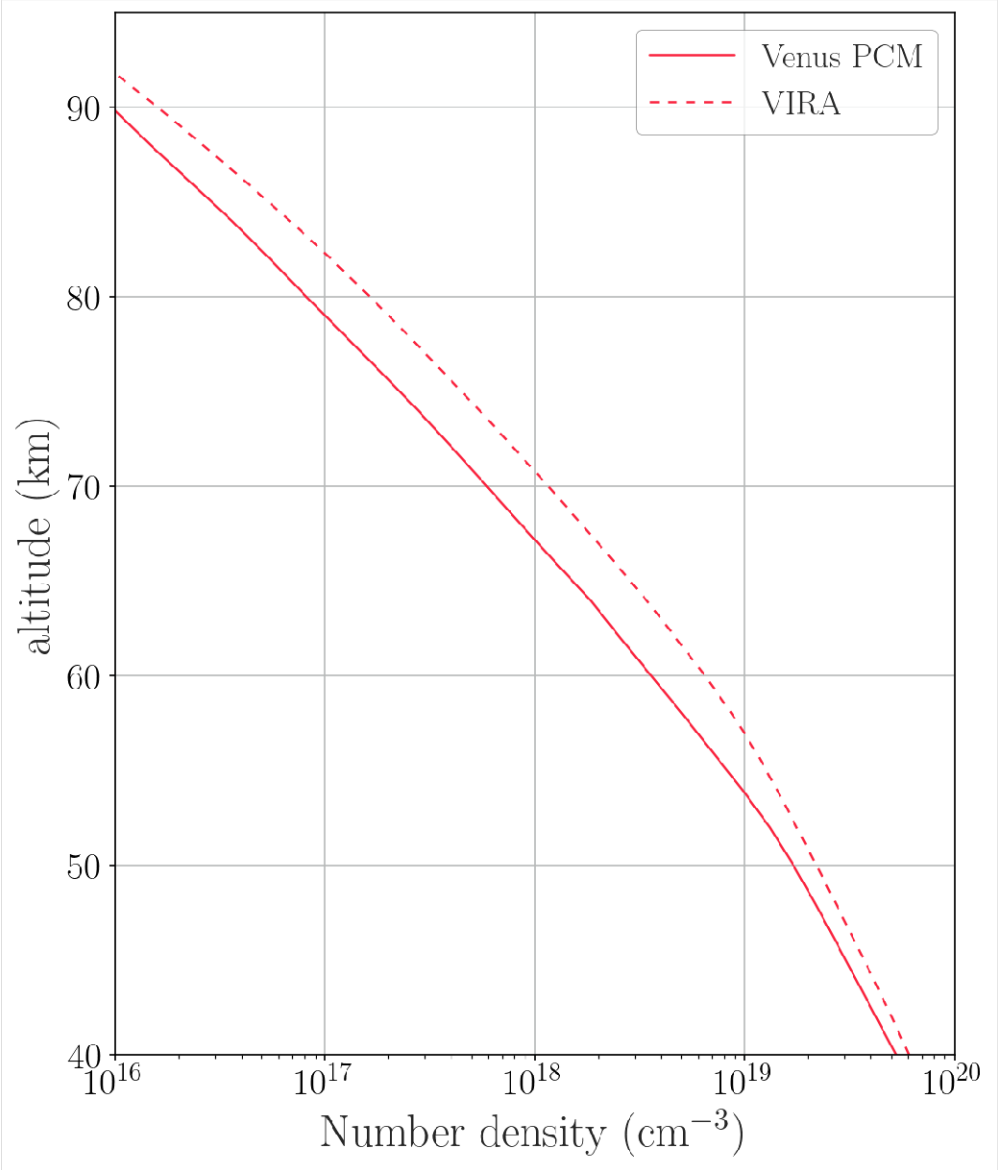

Figure 4: Mean vertical profile of the atmospheric number density (cm^{-3}) calculated by the Venus PCM and given by the VIRA climatology.

Table 1: List of chemical reactions in the Venus PCM

Number	Reaction	Rate coefficient	Reference
R1	$O + O_2 + CO_2 \longrightarrow O_3 + CO_2$	$2.5 \cdot 6.0 \cdot 10^{-34} \cdot \left(\frac{T}{300}\right)^{-2.4}$	Burkholder et al. (2015)
R2	$O + O + CO_2 \longrightarrow O_2 + CO_2$	$2.5 \cdot 9.46 \cdot 10^{-34} \times \exp\left(\frac{485}{T}\right)$	Campbell and Gray (1973)
R3	$O + O_3 \longrightarrow O_2 + O_2$	$8 \cdot 10^{-12} \times \exp\left(-\frac{2060}{T}\right)$	Burkholder et al. (2015)
R4	$O(^1D) + CO_2 \longrightarrow O + CO_2$	$7.5 \cdot 10^{-11} \times \exp\left(\frac{115}{T}\right)$	Burkholder et al. (2015)
R5	$O(^1D) + H_2O \longrightarrow OH + OH$	$1.63 \cdot 10^{-10} \times \exp\left(\frac{60}{T}\right)$	Burkholder et al. (2015)
R6	$O(^1D) + H_2 \longrightarrow OH + H$	$1.1 \cdot 10^{-10}$	Sander et al. (2006)
R7	$O(^1D) + O_2 \longrightarrow O + O_2$	$3.3 \cdot 10^{-11} \times \exp\left(\frac{55}{T}\right)$	Burkholder et al. (2015)
R8	$O(^1D) + O_3 \longrightarrow O_2 + O_2$	$1.2 \cdot 10^{-10}$	Burkholder et al. (2015)
R9	$O(^1D) + O_3 \longrightarrow O_2 + O + O$	$1.2 \cdot 10^{-10}$	Burkholder et al. (2015)
R10	$O + HO_2 \longrightarrow OH + O_2$	$3.0 \cdot 10^{-11} \times \exp\left(\frac{200}{T}\right)$	Burkholder et al. (2015)
R11	$O + OH \longrightarrow O_2 + H$	$2.2 \cdot 10^{-11} \times \exp\left(\frac{120}{T}\right)$	Sander et al. (2006)
R12	$H + O_3 \longrightarrow OH + O_2$	$1.4 \cdot 10^{-10} \times \exp\left(-\frac{470}{T}\right)$	Burkholder et al. (2015)
R13	$H + HO_2 \longrightarrow OH + OH$	$7.2 \cdot 10^{-11}$	Burkholder et al. (2015)
R14	$H + HO_2 \longrightarrow H_2 + O_2$	$6.9 \cdot 10^{-12}$	Burkholder et al. (2015)
R15	$H + HO_2 \longrightarrow H_2O + O$	$1.6 \cdot 10^{-12}$	Burkholder et al. (2015)
R16	$OH + HO_2 \longrightarrow H_2O + O_2$	$4.8 \cdot 10^{-11} \times \exp\left(\frac{250}{T}\right)$	Burkholder et al. (2015)
R17	$HO_2 + HO_2 \longrightarrow H_2O_2 + O_2$	$1.5 \cdot 10^{-12} \times \exp\left(\frac{19}{T}\right)$	Christensen et al. (2002)
R18	$HO_2 + H_2O_2 \longrightarrow H_2O + HO_2$	$1.8 \cdot 10^{-12}$	Burkholder et al. (2015)
R19	$OH + H_2 \longrightarrow H_2O + H$	$2.8 \cdot 10^{-12} \times \exp\left(-\frac{1800}{T}\right)$	Burkholder et al. (2015)
R20	$H + O_2 + CO_2 \longrightarrow HO_2 + CO_2$	$k_0 = 2.5 \cdot 4.4 \cdot 10^{-32} \cdot \left(\frac{T}{300}\right)^{-1.3}$ $k_\infty = 4.7 \cdot 10^{-11} \cdot \left(\frac{T}{300}\right)^{-0.2}$	Burkholder et al. (2015)
R21	$O + H_2O_2 \longrightarrow OH + HO_2$	$1.4 \cdot 10^{-12} \times \exp\left(-\frac{2000}{T}\right)$	Burkholder et al. (2015)
R22	$OH + OH \longrightarrow H_2O + O$	$1.8 \cdot 10^{-12}$	Burkholder et al. (2015)
R23	$OH + O_3 \longrightarrow HO_2 + O_2$	$1.7 \cdot 10^{-12} \times \exp\left(-\frac{940}{T}\right)$	Burkholder et al. (2015)
R24	$HO_2 + O_3 \longrightarrow OH + O_2 + O_2$	$1.0 \cdot 10^{-14} \times \exp\left(-\frac{490}{T}\right)$	Burkholder et al. (2015)
R25	$HO_2 + HO_2 + CO_2 \longrightarrow H_2O_2 + O_2 + CO_2$	$2.5 \cdot 1.7 \cdot 10^{-33} \times \exp\left(\frac{1000}{T}\right)$	Sander et al. (2003)
R26	$OH + OH + CO_2 \longrightarrow H_2O_2 + CO_2$	$k_0 = 2.5 \cdot 6.9 \cdot 10^{-31} \cdot \left(\frac{T}{300}\right)^{-1.0}$ $k_\infty = 2.6 \cdot 10^{-11}$	Burkholder et al. (2015)
R27	$H + H + CO_2 \longrightarrow H_2 + CO_2$	$2.5 \cdot 1.7 \cdot 10^{-33} \times \exp\left(\frac{1000}{T}\right)$	Baulch et al. (2005)
R28	$CO + OH \longrightarrow CO_2 + H$	see reference	Joshi and Wang (2006)
R29	$CO + O + CO_2 \longrightarrow CO_2 + CO_2$	$2.5 \cdot 6.5 \cdot 10^{-33} \times \exp\left(-\frac{2184}{T}\right)$	Tsang and Hampson (1986)
R30	$HCl + O(^1D) \longrightarrow OH + Cl$	$1.0 \cdot 10^{-10}$	Burkholder et al. (2015)
R31	$HCl + O(^1D) \longrightarrow H + ClO$	$3.6 \cdot 10^{-11}$	Burkholder et al. (2015)
R32	$HCl + O \longrightarrow OH + Cl$	$1.0 \cdot 10^{-11} \times \exp\left(-\frac{3300}{T}\right)$	Burkholder et al. (2015)
R33	$HCl + OH \longrightarrow H_2O + Cl$	$2.6 \cdot 10^{-12} \times \exp\left(-\frac{350}{T}\right)$	Sander et al. (2006)
R34	$ClO + O \longrightarrow Cl + O_2$	$2.8 \cdot 10^{-11} \times \exp\left(\frac{85}{T}\right)$	Burkholder et al. (2015)
R35	$ClO + OH \longrightarrow Cl + HO_2$	$7.4 \cdot 10^{-12} \times \exp\left(\frac{270}{T}\right)$	Burkholder et al. (2015)
R35$_{bis}$	$ClO + OH \longrightarrow HCl + O_2$	$6.0 \cdot 10^{-13} \times \exp\left(\frac{230}{T}\right)$	Burkholder et al. (2015)
R36	$Cl + H_2 \longrightarrow HCl + H$	$3.05 \cdot 10^{-11} \times \exp\left(-\frac{2270}{T}\right)$	Burkholder et al. (2015)
R37	$Cl + O_3 \longrightarrow ClO + O_2$	$2.3 \cdot 10^{-11} \times \exp\left(-\frac{200}{T}\right)$	Burkholder et al. (2015)
R38	$Cl + HO_2 \longrightarrow ClO + OH$	$4.1 \cdot 10^{-11} \times \exp\left(-\frac{450}{T}\right)$	Sander et al. (2006)
R39	$Cl + HO_2 \longrightarrow HCl + O_2$	$1.8 \cdot 10^{-11} \times \exp\left(\frac{170}{T}\right)$	Sander et al. (2006)
R40	$Cl + H_2O_2 \longrightarrow HCl + HO_2$	$1.1 \cdot 10^{-11} \times \exp\left(-\frac{980}{T}\right)$	Burkholder et al. (2015)
R41	$Cl + CO + CO_2 \longrightarrow ClCO + CO_2$	$3.2 \cdot 1.3 \cdot 10^{-33} \cdot \left(\frac{T}{300}\right)^{-3.8}$	Burkholder et al. (2015) and Nicovich et al. (1990)
R42	$ClCO + CO_2 \longrightarrow Cl + CO + CO_2$	$k_{eq} = 1.6 \cdot 10^{-25} \times \exp\left(\frac{4000}{T}\right)$ $k = k_{R41} \cdot [CO_2]/k_{eq}$	Mills (1998)
R43	$ClCO + O_2 + CO_2 \rightleftharpoons ClCO_3 + CO_2$	$a = \left(5.7 \cdot 10^{-15} \times \exp\left(\frac{500}{T}\right)\right)$ $k = a/\left(\left(1.0 \cdot 10^{17} + 0.05 \cdot [CO_2]\right) \cdot [CO_2]\right)$	Yung and DeMore (1982)
R44	$ClCO_3 + Cl \longrightarrow Cl + ClO + CO_2$	$1.0 \cdot 10^{-11}$	Yung and DeMore (1982)
R45	$ClCO_3 + O \longrightarrow Cl + O_2 + CO_2$	$1.0 \cdot 10^{-11}$	Yung and DeMore (1982)
R46	$ClO + HO_2 \longrightarrow HOCl + O_2$	$2.7 \cdot 10^{-12} \times \exp\left(\frac{220}{T}\right)$	Burkholder et al. (2015)
R47	$OH + HOCl \longrightarrow H_2O + ClO$	$3.0 \cdot 10^{-12} \times \exp\left(-\frac{500}{T}\right)$	Burkholder et al. (2015)
R48	$O + HOCl \longrightarrow OH + ClO$	$1.7 \cdot 10^{-13}$	Burkholder et al. (2015)
R49	$Cl + Cl + CO_2 \longrightarrow Cl_2 + CO_2$	$2.6 \cdot 10^{-33} \times \exp\left(\frac{900}{T}\right)$	Mills (1998)
R50	$ClCO + O \longrightarrow Cl + CO_2$	$3.0 \cdot 10^{-11}$	Yung and DeMore (1982)
R51	$Cl_2 + O(^1D) \longrightarrow Cl + ClO$	$2.0 \cdot 10^{-10}$	Burkholder et al. (2015)
R52	$Cl_2 + H \longrightarrow HCl + Cl$	$1.43 \cdot 10^{-10} \times \exp\left(-\frac{591}{T}\right)$	Baulch et al. (1980)
R53	$Cl + ClCO \longrightarrow Cl_2 + CO$	$2.16 \cdot 10^{-9} \times \exp\left(-\frac{1670}{T}\right)$	Baulch et al. (1980)
R54	$ClCO + ClCO \longrightarrow COCl_2 + CO$	$5.0 \cdot 10^{-11}$	Mills (1998)
R55	$Cl + SO_2 + CO_2 \longrightarrow ClSO_2 + CO_2$	$1.3 \cdot 10^{-34} \times \exp\left(\frac{940}{T}\right)$	Mills (1998)
R56	$ClSO_2 + O \longrightarrow SO_2 + ClO$	$1.0 \cdot 10^{-11}$	Mills (1998)

Number	Reaction	Rate coefficient	Reference
R57	$ClSO_2 + H \longrightarrow SO_2 + HCl$	$1.0 \cdot 10^{-11}$	Mills (1998)
R58	$ClSO_2 + ClSO_2 \longrightarrow Cl_2 + SO_2 + SO_2$	$5.0 \cdot 10^{-13}$	Moses et al. (2002)
R59	$Cl + O + CO_2 \longrightarrow ClO + CO_2$	$5.0 \cdot 10^{-32}$	Yung and DeMore (1998)
R60	$Cl_2 + O \longrightarrow ClO + Cl$	$7.4 \cdot 10^{-12} \times \exp\left(-\frac{1670}{T}\right)$	Mills (1998)
R61	$ClCO + OH \longrightarrow HOCl + CO$	$1.5 \cdot 10^{-1}$	Mills (1998)
R62	$Cl_2 + OH \longrightarrow Cl + HOCl$	$2.6 \cdot 10^{-12} \times \exp\left(-\frac{1100}{T}\right)$	Burkholder et al. (2015)
R63	$ClCO + O \longrightarrow ClO + CO$	$3.0 \cdot 10^{-12}$	Yung and DeMore (1982)
R64	$ClCO + Cl_2 \longrightarrow COCl_2 + Cl$	$6.45 \cdot 10^{-2} \cdot k_{R43}$	Ohta (1983)
R65	$HCl + H \longrightarrow H_2 + Cl$	$1.5 \cdot 10^{-11} \times \exp\left(-\frac{1750}{T}\right)$	Mills (1998)
R66	$ClCO + H \longrightarrow HCl + CO$	$1.0 \cdot 10^{-11}$	Yung and DeMore (1982)
R67	$Cl + H + M \longrightarrow HCl + M$	$1.0 \cdot 10^{-32}$	Yung and DeMore (1982)
R68	$S + O_2 \longrightarrow SO + O$	$2.3 \cdot 10^{-12}$	Sander et al. (2011)
R69	$S + O_3 \longrightarrow SO + O_2$	$1.2 \cdot 10^{-11}$	Burkholder et al. (2015)
R70	$SO + O_2 \longrightarrow SO_2 + O$	$1.25 \cdot 10^{-13} \times \exp\left(-\frac{2190}{T}\right)$	Sander et al. (2011)
R71	$SO + O_3 \longrightarrow SO_2 + O_2$	$3.4 \cdot 10^{-12} \times \exp\left(-\frac{1100}{T}\right)$	Burkholder et al. (2015)
R72	$SO + OH \longrightarrow SO_2 + H$	$2.7 \cdot 10^{-11} \times \exp\left(\frac{335}{T}\right)$	Burkholder et al. (2015)
R73	$S + OH \longrightarrow SO + OH$	$6.6 \cdot 10^{-11}$	Burkholder et al. (2015)
R74	$SO + O + CO_2 \longrightarrow SO_2 + CO_2$	$k_0 = 4.2 \cdot 10^{-30}$ $k_\infty = 5.3 \cdot 10^{-11}$	Singleton and Cvetanović (1988)
R75	$SO + HO_2 \longrightarrow SO_2 + OH$	$2.8 \cdot 10^{-11}$	Yung and DeMore (1982)
R76	$SO_2 + O + CO_2 \longrightarrow SO_3 + CO_2$	$k_0 = 5 \cdot 9.5 \cdot 10^{-23}\ T^{-3} \times \exp\left(-\frac{2400}{T}\right)$ $k_\infty = 6.1 \cdot 10^{-13} \times \exp\left(-\frac{850}{T}\right)$ $\tau = (k_0 \cdot [CO_2])/(1. + k_0 \cdot [CO_2]/k_\infty)$ $x = 1/\left(1 + \log^2\left((k_0 \cdot [CO_2])/k_\infty\right)\right)$ $f_T = 0.558 \times \exp(-T/316) + 0.442 \times \exp(-T/7442)$ $k = \tau \cdot {f_T}^x$	Naidoo et al. (2005)
R77	$S + O + CO_2 \longrightarrow SO + CO_2$	$1.5 \cdot 10^{-34} \times \exp\left(\frac{900}{T}\right)$	Moses et al. (2002)
R78	$SO_3 + H_2O + H_2O \longrightarrow H_2SO_4 + H_2O$	$2.26 \cdot 10^{-43} \cdot T \times \exp\left(\frac{6540}{T}\right)$	Lovejoy et al. (1996)
R79	$SO + ClO \longrightarrow SO_2 + Cl$	$2.8 \cdot 10^{-11}$	Burkholder et al. (2015)
R80	$SO + SO_3 \longrightarrow SO_2 + SO_2$	$2.0 \cdot 10^{-15}$	Chung et al. (1975)
R81	$SO_3 + O \longrightarrow SO_2 + O_2$	$2.32 \cdot 10^{-16} \times \exp\left(-\frac{487}{T}\right)$	Jacob and Winkler (1972)
R82	$SO + SO + CO_2 \longrightarrow S_2O_2 + CO_2$	$k_0 = 2.5 \cdot 4.4 \cdot 10^{-31}$ $k_\infty = 1.0 \cdot 10^{-11}$	Herron and Huie (1980)
R83	$S_2O_2 + CO_2 \longrightarrow SO + SO + CO_2$	$k_{eq} = 2.5 \cdot 1.0 \cdot 10^{-28} \times \exp\left(\frac{6000}{T}\right)$ $k = k_{eq}/k_{R82}$	Mills (1998)
R84	$ClCO_3 + SO \longrightarrow Cl + SO_2 + CO_2$	$1.0 \cdot 10^{-11}$	Mills (1998)
R85	$S + CO + CO_2 \longrightarrow OCS + CO_2$	$2.5 \cdot 4.0 \cdot 10^{-33} \times \exp\left(-\frac{1940}{T}\right)$	Zhang et al. (2012)
R86	$S + ClCO \longrightarrow OCS + Cl$	$3.0 \cdot 10^{-12}$	Zhang et al. (2012)
R87	$SO_2 + OH + CO_2 \longrightarrow HSO_3 + CO_2$	$k_0 = 2.5 \cdot 3.3 \cdot 10^{-31} \cdot \left(\frac{T}{300}\right)^{-4.3}$ $k_\infty = 1.6 \cdot 10^{-12}$	Burkholder et al. (2015)
R88	$HSO_3 + O_2 \longrightarrow HO_2 + SO_3$	$1.3 \cdot 10^{-12} \times \exp\left(-\frac{330}{T}\right)$	Burkholder et al. (2015)
R89	$S + S + CO_2 \longrightarrow S_2 + CO_2$	$k_0 = 1.19 \cdot 10^{-29}$ $k_\infty = 1.0 \cdot 10^{-10}$	Nicholas et al. (1979)
R90	$S_2 + O \longrightarrow SO + S$	$2.2 \cdot 10^{-11} \times \exp\left(-\frac{84}{T}\right)$	Moses et al. (2002)
R91	$S + OCS \longrightarrow S_2 + CO$	$6.6 \cdot 10^{-20} \cdot T^{2.57} \times \exp\left(-\frac{1180}{T}\right)$	Lu et al. (2006)
R92	$OCS + O \longrightarrow SO + CO$	$1.6 \cdot 10^{-11} \times \exp\left(-\frac{2150}{T}\right)$	Atkinson et al. (2004)
R93	$S + SO_3 \longrightarrow SO_2 + SO$	$1.0 \cdot 10^{-16}$	Moses et al. (2002)
R94	$S + HO_2 \longrightarrow SO + OH$	$3.0 \cdot 10^{-11} \times \exp\left(\frac{200}{T}\right)$	Yung and DeMore (1982)
R95	$S + ClO \longrightarrow SO + Cl$	$4.0 \cdot 10^{-11}$	Moses et al. (2002)
R96	$H_2SO_4 + H_2O \longrightarrow SO_3 + H_2O + H_2O$	$7.0 \cdot 10^{-14} \times \exp\left(-\frac{5170}{T}\right)$	Krasnopolsky (2007)
R97	$SO_3 + OCS \longrightarrow S_2O_2 + CO_2$	$1.0 \cdot 10^{-11} \times \exp\left(-\frac{10000}{T}\right)$	Krasnopolsky (2007)
R98	$S_2O_2 + OCS \longrightarrow CO + SO_2 + S_2$	$1.0 \cdot 10^{-20}$	Krasnopolsky (2007)
R99	$SO + SO \longrightarrow SO_2 + S$	$1.0 \cdot 10^{-12} \times \exp\left(-\frac{1700}{T}\right)$	Herron and Huie (1980)
R100	$O_2(^1\Delta\ g) + CO_2 \longrightarrow O_2 + CO_2$	$1.0 \cdot 10^{-20}$	Krasnopolsky (2010a)
R101	$O_2(^1\Delta\ g) \longrightarrow O_2 + h\nu$	$2.2 \cdot 10^{-4}$	Lafferty et al. (1998)

the rate coefficient for bimolecular reactions is in $cm^3\ molec^{-1}\ s^{-1}$ and $cm^6\ molec^{-2}\ s^{-1}$ for third-body reaction. k_0 and k_∞ respectively are the coefficient for low and high pressure concerning third-body reactions. The third-body reactions are multiplied by 2.5 or 5 in order to take into account the efficiency of CO_2 comparing to N_2 or Ar respectively.

Based on the recent literature it appears that there is no clear consensus on the broad impact of odd nitrogen chemistry on Venus (Marcq et al., 2018). However, Krasnopolsky (2006) emphasized the possible role of lightnings in the production of NO, measured at 5.5 ppbv below 60 km (Krasnopolsky, 2006), and Krasnopolsky (2012b) calculated that odd nitrogen might be responsible of one-quarter of O_2 production and one-quarter of SO_2 reformation after its photodissociation. In the light of this result, adding nitrogen chemistry will be a future development of the Venus

PCM, which has the ability to compute adequately the N_2 photolysis in its version extended to the thermosphere up to 150 km (Gilli et al., 2017). Our chemical system takes into account 31 gas-phase and 2 liquid-phase species (Table 2) interacting through 101 chemical reactions and 20 photodissociations (Table 1 and 3).

1	CO_2	10	O_3	19	HOCl	28	OCS
2	CO	11	H	20	ClCO	29	HSO_3
3	H_2	12	OH	21	$ClCO_3$	30	$H_2SO_{4\,(g)}$
4	$H_2O_{(g)}$	13	HO_2	22	$COCl_2$	31	$H_2SO_{4(l)}$
5	$H_2O_{(l)}$	14	H_2O_2	23	S	32	S_2
6	$O(^1D)$	15	Cl	24	SO	33	$ClSO_2$
7	O	16	ClO	25	SO_2		
8	O_2	17	Cl_2	26	SO_3		
9	$O_2(a^1\Delta g)$	18	HCl	27	S_2O_2		

Table 2: List of chemical species in the Venus PCM. (*g*) stands for gas phase, (*l*) for liquid phase.

2.2.1. Photochemical model : photodissociation rates

To compute the photodissociation rates, we use the same strategy as the one used in the photochemical model coupled to the LMD Mars GCM (Lefèvre et al., 2004). The rate coefficients (or J values) are calculated by the Tropospheric Ultraviolet and Visible (TUV) model (Madronich and Flocke, 1999) initially developed to compute the actinic flux and photodissociations in the terrestrial atmosphere. We have adapted TUV to the Venus atmosphere by defining CO_2, SO_2, and clouds as the main absorbers of the incident radiation. Solar flux at 1 AU is taken from the high-resolution (0.05 nm) composite spectrum described by Thuillier et al. (2004).

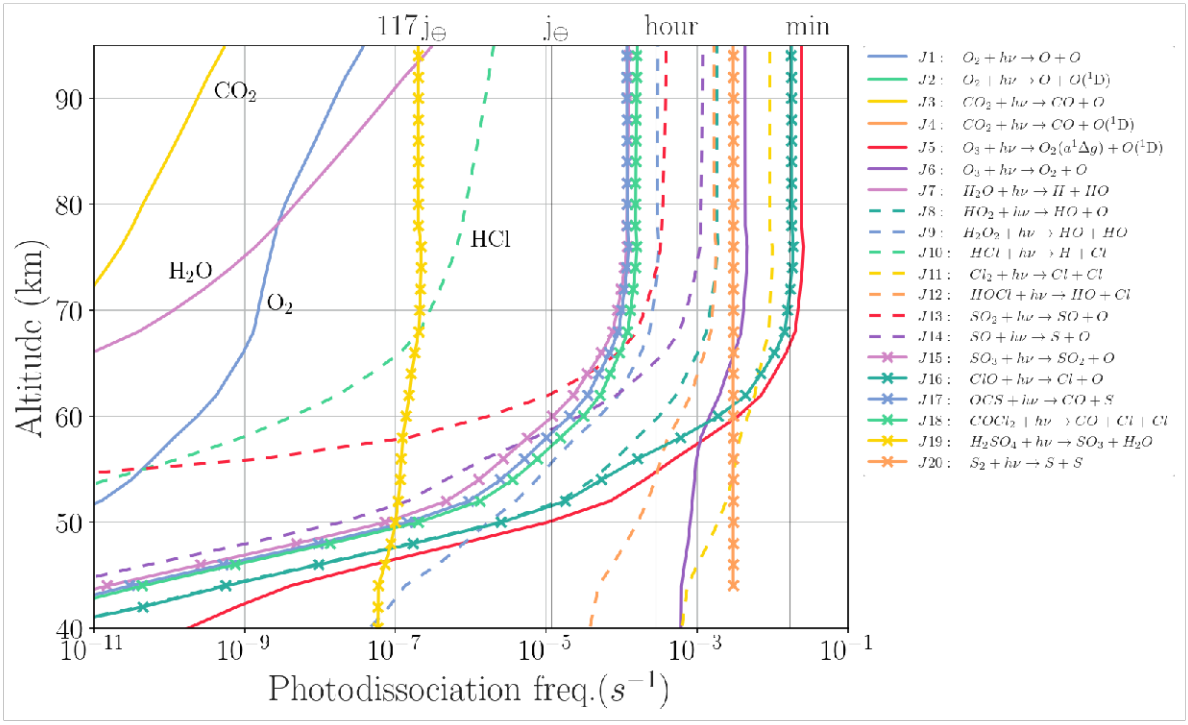

Figure 5: Photodissociation rates (s^{-1}) calculated for a solar zenith angle of 45°. In this example the CO_2 and SO_2 used to compute the rates are taken from typical values from measured vertical profiles. Typical timescales are also indicated on the upper x-axis.

Number	Photodissociation	Reference for cross sections σ_A
J1	$O_2 + h\nu \longrightarrow O + O$	Ogawa and Ogawa (1975); Gibson et al. (1983); Lewis et al. (1983) Yoshino et al. (1988); Minschwaner et al. (1992)
J2	$O_2 + h\nu \longrightarrow O + O(^1D)$	Ogawa and Ogawa (1975); Gibson et al. (1983); Lewis et al. (1983) Yoshino et al. (1988); Minschwaner et al. (1992)
J3	$CO_2 + h\nu \longrightarrow CO + O$	σ_{CO_2} is a function of T $\lambda > 167$ nm Yoshino et al. (1996a); Parkinson et al. (2003)
J4	$CO_2 + h\nu \longrightarrow CO + O(^1D)$	σ_{CO_2} is a function of T $\lambda < 167$ nm Chan et al. (1993); Stark et al. (2007)
J5	$O_3 + h\nu \longrightarrow O_2(^1\Delta\,g) + O(^1D)$	Sander et al. (2006)
J6	$O_3 + h\nu \longrightarrow O_2 + O$	Burkholder et al. (2015)
J7	$H_2O + h\nu \longrightarrow H + OH$	Thompson et al. (1963); Yoshino et al. (1996b); Cheng et al. (1999)
J8	$HO_2 + h\nu \longrightarrow OH + O$	Burkholder et al. (2015)
J9	$H_2O_2 + h\nu \longrightarrow OH + OH$	λ : 125 – 185 nm Schürgers and Welge (1968) λ : 190 – 350 nm Sander et al. (2003)
J10	$HCl + h\nu \longrightarrow H + Cl$	Burkholder et al. (2015)
J11	$Cl_2 + h\nu \longrightarrow Cl + Cl$	Burkholder et al. (2015)
J12	$HOCl + h\nu \longrightarrow OH + Cl$	Burkholder et al. (2015)
J13	$SO_2 + h\nu \longrightarrow SO + O$	σ_{SO_2} is a function of T Wu et al. (2000); Hermans et al. (2009); Vandaele et al. (2009)
J14	$SO + h\nu \longrightarrow S + O$	λ : 190 – 235 nm Phillips (1981) $\lambda > 235$ nm extrapolation of Phillips (1981)
J15	$SO_3 + h\nu \longrightarrow SO_2 + O$	λ : 140 – 294 nm Hintze et al. (2003) λ : 296 – 330 nm Burkholder and McKeen (1997)
J16	$ClO + h\nu \longrightarrow Cl + O$	Trolier et al. (1990)
J17	$OCS + h\nu \longrightarrow CO + S$	Burkholder et al. (2015)
J18	$COCl_2 + h\nu \longrightarrow CO + Cl + Cl$	Burkholder et al. (2015)
J19	$H_2SO_4 + h\nu \longrightarrow SO_3 + H_2O$	Mills et al. (2005)
J20	$S_2 + h\nu \longrightarrow S + S$	Mills (1998)

Table 3: List of photodissociation reactions in the Venus PCM

Absorption and scattering through the atmosphere are treated in spherical geometry by the multistream discrete ordinate method of Stamnes et al. (1988). We have adapted the wavelength resolution to describe accurately the spectral features in the solar flux or the absorption cross sections: 0.1 nm in the Lyman α region, 0.5 nm in the CO_2 band shortward of 175 nm, 0.01 nm in the CO_2 band and the Schumann-Runge bands of O_2 between 175 nm and 205 nm, and 0.5 nm longward of 205 nm where SO_2 absorption occurs. The list of photodissociation processes taken into account in the model, as well as the references used for the absorption cross-sections of each gas, are given in Table 3. When available, the temperature dependence of the absorption cross sections is taken into account, as is Rayleigh scattering.

Our calculations also include the absorption and scattering of radiation by clouds. The optical thickness of each layer of the Venus clouds is tabulated according to the parameters of Crisp (1986). Following the detailed calculations of Zhang et al. (2012), we set the value of the aerosol single scattering albedo to $\omega = 0.99999$, with an asymmetry factor g = 0.74.

In order to save computational resources, the photolysis rates are calculated off-line and are stored in a three-dimensional lookup table that is a function of the overhead CO_2 column, the overhead SO_2 column, and the solar zenith angle. Solar zenith angle (SZA) is tabulated from 0 to 95°, with a resolution of 1° beyond 90° to describe the rapidly varying photolysis rates at sunrise and sunset. During the course of the Venus PCM integration, photolysis rates are obtained for each sunlit grid point by interpolation in the lookup table according to the local SZA and the actual columns of CO_2 and SO_2 calculated by the photochemical model. Fig. 5 plots the photodissociation rates calculated for a SZA of 45°.

In this example, the SO_2 mixing ratio decreases from 130 ppmv to 1 ppmv between 50 to 60 km and is equal to 100 ppbv above 70 km. Shortward of 200 nm, CO_2 is the main ultraviolet absorber and the impact of the CO_2 overhead column on the J values is clearly visible for H_2O, O_2 and HCl, which are primarily photolyzed in the same wavelength range (of course this is also the case for CO_2 by self-screening effect). Between 200 – 340 nm, SO_2 becomes the primary ultraviolet absorber but its weaker opacity only has an effect below 65 km for the species photolyzed at the same wavelengths.

2.2.2. Chemical solver

For solving the ordinary differential equations system of the photochemistry, the Venus PCM uses the ASIS (Adaptative Semi Implicit Scheme) solver described in detail by Cariolle et al. (2017). The solver calculates the

vector of the concentrations of all species $\boldsymbol{C}^{t+\Delta t}$, at time $t + \Delta t$ from $\boldsymbol{C}^t$ at time t:

$$\boldsymbol{C}^{t+\Delta t} = M^{-1}\,\boldsymbol{C}^t \tag{1}$$

where the matrix M is defined by:

$$M = I - \Delta t \cdot\ J^t(\epsilon) \tag{2}$$

I is the identity matrix and $J^t(\epsilon)$ is the discrete Jacobian matrix of the temporal derivative of $\boldsymbol{C}$ at time t. $J^t(\epsilon)$ depends on the adaptative term ϵ defined for the reaction between species i and j as ϵ_{ij}:

$$\epsilon_{ij} = \frac{C_i^t}{\left(C_i^t + C_j^t\right)} \tag{3}$$

ϵ_{ij} is used to weighs the degree of implicity of the numerical treatment of each reaction, which adapts automatically to the relative abundance of each reactant. This method does not require any particular treatment for short- or long-lived species and strictly conserves mass. In addition, a time-stepping module based on the two-steps method (Verwer and Simpson, 1995) controls the accuracy of the solution and reduces the timestep Δt when chemical concentrations vary rapidly, typically at sunrise and sunset.

2.2.3. Initialization of chemical species

Chemical species of the Venus PCM are initialized by setting the mixing ratio of H_2O, OCS and CO to their values observed below the clouds by *Venus Express* or from the Earth (Table 4). At the beginning of the simulation, a uniform mixing ratio is imposed for those three species between 0 and 40 km. The main reservoir of chlorine, HCl, is initialized throughout the atmosphere to the value of 0.4 ppmv observed above the clouds by Krasnopolsky (2010b) and Sandor and Clancy (2012). A more complicated problem concerns the initial value of SO_2 below the clouds. In the simulation presented here, the initial SO_2 mixing ratio was set to 12 ppmv in the deep atmosphere, whereas available observations indicate values around 100 ppmv (e.g., Marcq et al. (2008)). Stolzenbach (2016) showed that the Venus PCM largely overestimated SO_2 above the clouds if initialized with such a large sulfur content in the deep atmosphere. This issue is common to all photochemical models of Venus published to date. In the literature, a typical workaround solution is to set the mixing ratio of SO_2 below the clouds to a value of the order of 10 ppmv, that is one order of magnitude smaller than indicated by the observations (e.g., Winick and Stewart (1980); Yung and DeMore (1982); Mills (1998); Krasnopolsky (2012b); Zhang et al. (2012); Shao et al. (2022)) while the 1D model presented in Bierson and Zhang (2020) simply prevents the SO_2 in the lower atmosphere to diffuse through the clouds. Evidently, the fact that the fate of 90% of the SO_2 found in the deep atmosphere remains unknown reflects a serious problem in the understanding of the sulfur budget on Venus. But, as noted by Krasnopolsky (2012b), there is for the moment no identified process able to deplete SO_2 by one order of magnitude in the lower cloud region. In the context of the current knowledge of Venus photochemistry and microphysics, and in the same spirit as previously published modelling studies, we chose to initialize SO_2 in the deep atmosphere to the low value required to produce realistic values of SO_2 and H_2O above the clouds. The investigation of a missing sulfur reservoir in the Venus clouds, or of the possible interaction between SO_2 and hydroxide salts in the droplets as proposed by Rimmer et al. (2021), is beyond the scope of the present paper and is deferred to a future study. Once the chemical species listed in Table 4 are initialized, the Venus PCM is integrated until all chemical species show stabilized mixing ratios at all altitudes. Because of the long time constants of vertical transport on Venus, this spin-up period is rather long. In the case of the results presented here, the equilibrium state of the Venus PCM was obtained after 50 Venus days of simulation.

2.3. Cloud modelling

Previously published 1D photochemical models of Venus do not calculate the condensation of sulfuric acid and water vapor. The present work aims at an explicit representation of the cloud composition. Our method is a middle way between the simple assumptions of 1D photochemical models and the detailed microphysical models such as those by Toon et al. (1979) or James et al. (1997). Nucleation and growth of liquid particles is not represented, but we do calculate the droplet number density as well as the transfers of H_2SO_4 and H_2O between the gas and the liquid phases. The main hypothesis of the model is that clouds are at all times in a a state of thermodynamic equilibrium.

Species	Volume mixing ratio	Reference
H_2O	30 ppmv	Bézard and de Bergh (2007) Marcq et al. (2008)
HCl	0.4 ppmv	Krasnopolsky (2010b) Sandor et al. (2012)
SO_2	12 ppmv	see text
OCS	3 ppmv	Marcq et al. (2008)
CO	25 ppmv	Cotton et al. (2012)

Table 4: Initial mixing ratios of chemical species in the Venus PCM. The initial mixing ratio of CO_2, not listed here, is initialized as $1 - \sum(others)$. All other species are initialized to zero.

This means that the condensation of H_2SO_4 and H_2O follows exactly the vapor pressure profile of the calculated mixture of H_2SO_4 and H_2O forming the droplets, thus not allowing sub or supersaturation. In addition, we assume that the statistical size distribution of the droplets does not vary too rapidly. This hypothesis is reasonable at the spatial and temporal scales resolved by the Venus PCM .

In the absence of a detailed microphysical modelling of the nucleation and growth of the liquid particles, we chose to constrain vertically the size distribution of the droplets from the measurements of the cloud particle size spectrometer, named hereafter LCPS, instrument on board the Pioneer Venus mission (Knollenberg and Hunten, 1980). This device measured particles sizes from 0.5 µm to 500 µm during the probe descent from 66 km to the ground. A review of known facts about aerosols on Venus after the Pioneer Venus mission can be fond in Ragent et al. (1985). Based on the local atmospheric conditions of a given Venus PCM grid cell (pressure, temperature, H_2SO_4 and H_2O mixing ratios), the cloud model then calculates the saturation vapor pressure of H_2SO_4, the composition of the binary (H_2SO_4,H_2O) liquid phase, and the number density of the droplets. The mixing ratios of the condensed species $H_2SO_{4(l)}$ and $H_2O_{(l)}$ are explicitly calculated and subtracted from the gas phase when condensation occurs. Finally, sedimentation is accounted for the size distribution of the droplets, leading to downward flux of condensed $H_2SO_{4(l)}$ and $H_2O_{(l)}$.

2.3.1. Droplet size distribution

According to the LCPS measurements (Knollenberg and Hunten, 1980), the clouds of Venus exhibit a multimodal size distribution that can be described with three log-normal functions. The log-normal function $n_N(R)$, defined by Eq. (4), represents the number density n_N of droplets of radius R. The usual unit of $n_N(R)$ is $\mu m^{-1}\,cm^{-3}$:

$$n_N(R) = \frac{dN}{dR} = \frac{N}{(2\pi)^{1/2}\,R\,\ln(\sigma_g)} \cdot \exp\left(-\frac{\left(\ln(R) - \ln(\overline{R}_g)\right)^2}{2\ln(\sigma_g)^2}\right) \tag{4}$$

Where R is the droplet radius, $\overline{R}_g$ and σ_g are respectively the median radius and geometric standard deviation of $n_N(R)$. N is the total number of droplets per cm^3 of air.

The so-called mode 1 found by LCPS experiment onboard Pioneer Venus (Knollenberg and Hunten, 1980) represents the smallest droplets with a median radius of 0.1 μm and is present in all layers, from the lower haze below 48 km to the upper haze above 70 km. The mode 2 has a median radius of about 1 μm and is mostly present in the main cloud deck, from 48 to 70 km. Recent studies from *Venus Express* mission instrument SPICAV led Wilquet et al. (2009, 2012) to unravel the bimodal distribution, mode 1 and 2, present in the upper haze. Nonetheless, these studies did not provide key information about the geometric standard deviation σ_g of these two modes. Therefore, the result on the number density is partly based on an assumption since the measurements do not provide an essential information on the log-normal law.

2.3.2. Composition of the liquid phase

According to the local conditions of pressure of temperature in each Venus PCM grid cell, the model determines at each time-step the composition of the clouds by calculating how H_2SO_4 and H_2O are partitioned into the gas and liquid phases. At equilibrium, the number density $n_{H_2SO_4\,(l)}$ of H_2SO_4 in the liquid phase is:

$$n_{H_2SO_4\,(l)} = n_{H_2SO_4} - \frac{p_{sat}}{k_B\,T} \tag{5}$$

Where $n_{H_2SO_4}$ is the total number density of H_2SO_4 (gas and liquid), p_{sat} is the saturation vapor pressure of H_2SO_4 above the binary solution (H_2O, H_2SO_4), k_B is the Boltzmann constant and T the temperature.

The saturation vapor pressure p_{sat} in the expression above is given by:

$$p_{sat} = \Gamma_{H_2SO_4}(T,\ w_{H_2SO_4}) \cdot p_a(T) \tag{6}$$

Where p_a is the saturation vapor pressure of the pure acid, from the equations of Ayers et al. (1980) modified by Kulmala and Laaksonen (1990) at low temperatures. The chemical activity $\Gamma_{H_2SO_4}$ of H_2SO_4 in Eq. (6) is calculated by interpolation of the data from Zeleznik (1991). This activity is a function of T but also of the weight fraction of sulfuric acid $w_{H_2SO_4}$ in the aerosol, which requires to know how much H_2O is also present in the liquid phase. One way to determine $w_{H_2SO_4}$ is to solve the Kelvin equation, which connects p_{sat} to the partial pressure of water vapor p_{H_2O}, in a situation of equilibrium with a binary (H_2O, H_2SO_4) droplet of radius R and density ρ_d:

$$\ln(p_{H_2O}) - \frac{2 M_{H_2O}\, \theta_S}{RT\, R\, \rho_d} - \ln(p_{sat}) = 0 \tag{7}$$

Where θ_S is the surface tension of the aqueous sulfuric acid solution (J m^{-2}) and M_{H_2O} is the molar mass of water. T and R are respectively the temperature and the perfect gas constant. In the Kelvin equation, p_{sat}, θ_S, and ρ_d all depend on $w_{H_2SO_4}$ (see Appendix A), which is one of the unknowns in Eq. (6). The other unknown is p_{H_2O} that is directly related to the number density of H_2O in the gas phase $n_{H_2O\,(g)}$ and is constrained by the conservation of H_2O mass:

$$n_{H_2O} = n_{H_2O\,(g)} + n_{H_2O\,(l)} \tag{8}$$

Where n_{H_2O} is the total number density H_2O and $n_{H_2O\,(l)}$ the number density in the liquid phase. Using the method of Ridders (Ridders, 1979), we solved iteratively Eqs. (7) and (8) for various values of $w_{H_2SO_4}$ until the final values of p_{sat} and p_{H_2O} satisfy both the Kelvin equation and the conservation of H_2O mass. Once p_{sat} is found, the determination of $n_{H_2SO_4\,(l)}$ is straightforward from Eq. (5), whereas $w_{H_2SO_4}$ allows to calculate $n_{H_2O\,(l)}$:

$$n_{H_2O\,(l)} = \frac{n_{H_2SO_4\,(l)} \cdot M_{H_2SO_4} \cdot (1 - w_{H_2SO_4})}{M_{H_2O} \cdot w_{H_2SO_4}} \tag{9}$$

Where $M_{H_2SO_4}$ and M_{H_2O} are the molar masses of H_2SO_4 and H_2O respectively. Finally, the condensed number densities are subtracted from the total number densities in order to consider only the gas phase components of H_2SO_4 and H_2O in the photochemical part of the code:

$$n_{H_2SO_4\,(g)} = n_{H_2SO_4} - n_{H_2SO_4\,(l)}$$
$$n_{H_2O\,(g)} = n_{H_2O} - n_{H_2O\,(l)}$$

2.3.3. Droplet number density

Then, we can calculate the total condensed mass per m^3 of air, M_{tot}:

$$M_{tot} = \frac{n_{H_2SO_4\,(l)}\, M_{H_2SO_4}}{w_{H_2SO_4} \cdot \mathcal{N}_A} \tag{10}$$

With $n_{H_2SO_4\,(l)}$ the number of condensed H_2SO_4 molecules per m^3 of air, $\mathcal{N}_A$ the Avogadro number, $w_{H_2SO_4}$ the weight fraction of sulfuric acid and $M_{H_2SO_4}$ the molar mass of H_2SO_4.

Since we evaluate the total condensed mass M_{tot}, we're looking for the equivalent number density which is the number of droplets per cm^3 of air for each mode of the size distribution and is noted N_i. This number density, N_i, and its corresponding condensed mass per mode M_i, will allow to evaluate the vertical mass flux of sedimentation for the log-normal size distribution and not for a fixed radius. M_i is a fraction k_i of M_{tot}:

$$M_i = k_i \cdot M_{tot} \tag{11}$$

Where for all modes j, $\sum_{i=1}^{j} \mathrm{k}_i = 1$. We are able to estimate for each mode i its k_i with the LCPS measurements from Knollenberg and Hunten (1980). We use the definition of M_i in order to calculate N_i:

$$\mathrm{M}_i = \int_0^\infty n_{\mathrm{M}i}(\mathrm{R})\,\mathrm{dR} \tag{12}$$

With the number density of each mode $n_{\mathrm{M}i}$:

$$n_{\mathrm{M}i}(\mathrm{R}) = \rho_d \cdot n_{Vi}(\mathrm{R}) = \frac{4\pi}{3}\,\rho_d\,\mathrm{R}^3 n_{\mathrm{N}i}(\mathrm{R}) \tag{13}$$

Where ρ_d is the previously calculated density of the solution in the droplet in $\mathrm{kg\,m^{-3}}$. Then we need to evaluate $n_{\mathrm{M}i}$ in order to get M_i. Log-normal law has an useful mathematical property, the moments of order k, noted m_k are defined as follows:

$$\begin{aligned} m_k &= \int_0^\infty \mathrm{R}^k n_{\mathrm{N}}(\mathrm{R})\mathrm{dR} \\ &= \mathrm{N}\overline{\mathrm{R}}_g{}^k \exp\left(\frac{k^2}{2}\ln^2\sigma_g\right) \end{aligned} \tag{14}$$

Finally, for each mode i of the radius size distribution of the cloud we get the droplet number density N_i:

$$\mathrm{N}_i = \mathrm{k}_i \cdot \mathrm{M}_{tot}\,\frac{3}{4\pi\,\rho_d}\,\overline{\mathrm{R}}_{gi}{}^{-3} \exp\left(-4.5\,\ln^2\sigma_{gi}\right) \tag{15}$$

2.3.4. Sedimentation

The sedimentation flux F_{sed}, in $\mathrm{kg\,m^{-2}\,s^{-1}}$, is a downward flux that is added to the transport component of the tracers in our model. It is the product of the condensed mass per m^3 of air times the terminal fall velocity, the Stokes velocity v_{st}:

$$\mathrm{F}_{sed}(\mathrm{R}) = \mathrm{M}(\mathrm{R}) \cdot v_{st}(\mathrm{R}) \tag{16}$$

The sedimentation flux is obviously a function of the droplet radius. We cannot reduce the size distribution to only one characteristic radius that should represent the size distribution as in Krasnopolsky (2015), even if it should be highlighted that Krasnopolsky (2015) use at least the modal radius of order 3, representing the mean radius of the volumetric/mass distribution, to estimate the sedimentation flux. Other models simply do not calculate or evaluate the condensed part (Zhang et al., 2012; Parkinson et al., 2015; Bierson and Zhang, 2020; Shao et al., 2020, 2022) and simulate the sulfur cycle through a flux of sulfur species at the cloud boundaries. Concerning the Stokes velocity v_{st}, we use the typical formulation that takes into account the changes in atmospheric regime through the Knudsen number, Kn :

$$v_{st} = (1 + \beta\mathrm{Kn})\,\frac{2g\mathrm{R}^2(\rho_d - \rho_f)}{9\eta} \tag{17}$$

Where $\beta = 1.246 + 0.42\,\exp(-0.87 \cdot {}^{1}/_{\mathrm{Kn}})$. g is the gravity acceleration of Venus, ρ_d the density of the droplet, ρ_f the density of the fluid the droplet is falling in (here the atmosphere). The dynamic viscosity η of the fluid, in Pa s, is calculated for CO_2 from Jones (1924). Kn is also a function of the radius as $\mathrm{Kn} = {}^{\lambda}/_{R}$, where λ is the mean free path of a CO_2 molecule in the atmosphere of Venus. The total flux due to sedimentation is the sum of the sedimentation fluxes of each mode. This calculation is detailed in Appendix B. Fig. 6 shows the characteristic sedimentation timescales for each mode in our model.

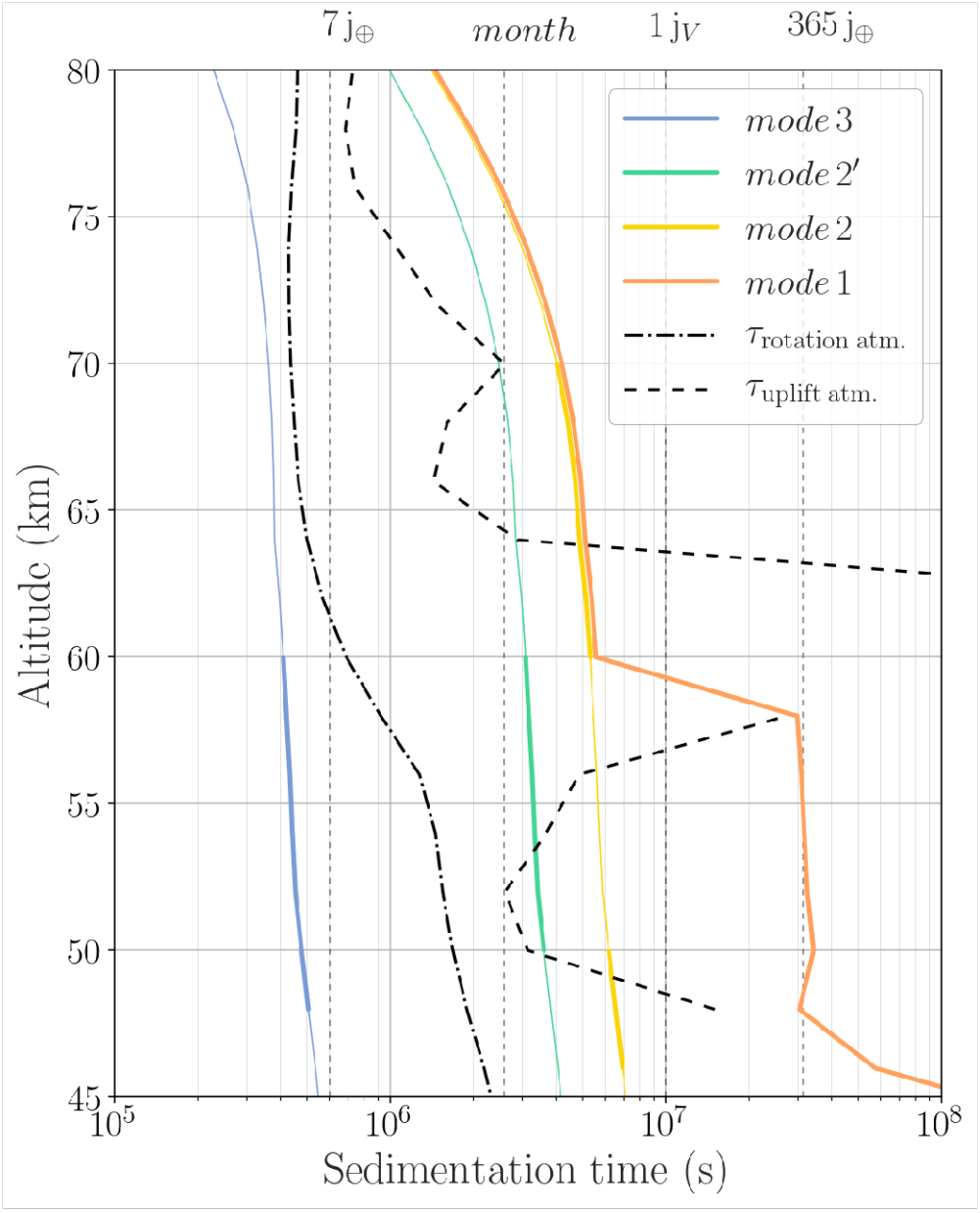

Figure 6: Vertical profiles of the sedimentation timescale (s). Each mode is represented by its fourth order modal radius, $\overline{\mathrm{R}}_g \exp\left(3\ln^2\sigma_g\right)$, or fifth $\overline{\mathrm{R}}_g \exp\left(4\ln^2\sigma_g\right)$, depending on the Knudsen number reflecting the change of dynamic regime. The sedimentation timescale corresponds to H/v_{sed}, where the scale height H is fixed to 5 km as in James et al. (1997). The curve of each mode is thickened at the altitudes where it is present in the model. $\tau_{rotation\,atm}$ is calculated by dividing the equatorial area of Venus by the equatorial average of the zonal wind. $\tau_{uplift\,atm}$ is calculated by dividing the scale height H by the equatorial average of the vertical wind. Only positive values of $\tau_{uplift\,atm}$ (updraft) are shown.

2.3.5. Parametrization of the "mode 3" particles

The vertical structure of the Venus clouds was observed by the LCPS instrument aboard *Pioneer Venus*. The so-called *mode 3* represents the distribution of the largest particles observed by LCPS, with a median radius of 3.65 µm. However, the existence and/or nature of the *mode 3* was debated as soon as it was discovered. Knollenberg and Hunten (1980) and Knollenberg (1984) hypothesized a population of crystals for the *mode 3*. Cimino (1982) described the *mode 3* as a set of solid particles coated with a thin layer of sulfuric acid. Toon et al. (1984) showed that the *mode 3* could also simply result from a LCPS calibration error and be the tail of the *mode 2* distribution. As stated by Mills

	$\overline{R}_g$	σ_g	k_{mass}
Upper Haze: 70 km - 100 km			
mode 1	0.2 µm	2.16	1.0
mode 2	.	.	0.0
mode 3'	.	.	0.0
Upper Cloud: 60 km - 70 km			
mode 1	0.2 µm	2.16	0.72
mode 2	1.0 µm	1.29	0.28
mode 3'	.	.	0.0
Middle Cloud: 50 km - 60 km			
mode 1	0.15 µm	1.9	0.032
mode 2	1.4 µm	1.23	0.781
mode 3'	3.65 µm	1.28	0.187
Lower Cloud: 48 km − 50 km			
mode 1	0.2 µm	1.8	0.146
mode 2	1.0 µm	1.29	0.207
mode 3'	3.65 µm	1.28	0.647
Pre Cloud: 46 km − 48 km			
mode 1	0.15 µm	1.8	0.04
mode 2	1.0 µm	1.29	0.96
mode 3'	.	.	0.0
Lower Haze: 30 km - 46 km			
mode 1	0.1 µm	1.57	1.0
mode 2	.	.	0.0
mode 3'	.	.	0.0

Table 5: Parametrization of the cloud structure in the Venus PCM. Median radius values $\overline{R}_g$ and geometric standard deviations σ_g are taken from Knollenberg and Hunten (1980) and James et al. (1997). *mode 3'* particles are solid particles coated with a thin layer (3% of the radius) of sulfuric acid, as in Cimino (1982). The values of the mass coefficients for the multimodal distribution k_{mass} are calculated assuming, as Knollenberg and Hunten (1980), a droplet acid fraction $w_{H_2SO_4} = 0.85$ and density $\rho_d = 2000\,\mathrm{kg\,m^{-3}}$. k_{mass} is then deduced from the number of droplets measured by the LCPS instrument of *Pioneer Venus* (Knollenberg and Hunten, 1980). We used the average number density values given in Table 1 of Knollenberg and Hunten (1980).

et al. (2013), *mode 3* can be considered in different ways. The first is to adhere strictly to the observations and to consider that the *mode 3* is composed of non-spherical solid particles (Knollenberg, 1984) whose nature and gaseous source are unknown. The second is to consider that the *mode 3* is only the edge of the *mode 2* distribution because the measurements of LCPS would have been misinterpreted (Toon et al., 1984).

If we consider that the *mode 3* is real and fully liquid, then it would represent more than 95% of the mass in the lower cloud and ∼ 80% in the middle cloud. It can be composed of sulfuric acid (Knollenberg and Hunten, 1980) or composed predominantly of non-spherical particles of unknown nature (Knollenberg, 1984; Toon et al., 1984).

A fully liquid *mode 3* is used in the microphysical models of James et al. (1997); Imamura and Hashimoto (2002) and Wilson et al. (2008). In our nominal simulation, we use a *mode 3* composed of a solid particle coated with a layer of sulfuric acid as in Cimino (1982). This mode will be called *mode 3'* thereafter. This assumption provides better results regarding the cloud vertical structure (also see Stolzenbach (2016)) compared to those obtained with the hypothesis of a fully liquid *mode 3*. A detailed study on the nature of the *mode 3* and its impact on the cloud structure is beyond the scope of this present work but will be provided from a newer version of the Venus PCM with a higher vertical resolution.

As suggested by Cimino (1982), we took a solid core of density $\rho_c = 2500\,\mathrm{kg\,m^{-3}}$, corresponding to that of basalt, with a radius that makes 97% of the total radius of the particle. The sulfuric acid coating then represents 3% of the total radius. The cloud parameters for the three modes implemented in the Venus PCM are indicated in the Table 5. The major difference introduced by the *mode 3'* is clearly seen in the middle cloud, where the *mode 3'* represents only about 19% of the condensed mass instead of 78% with a fully liquid *mode 3*. In the lower cloud, the *mode 3'* represents 65% of the condensed mass, versus 97% if the *mode 3* was assumed to be fully liquid.

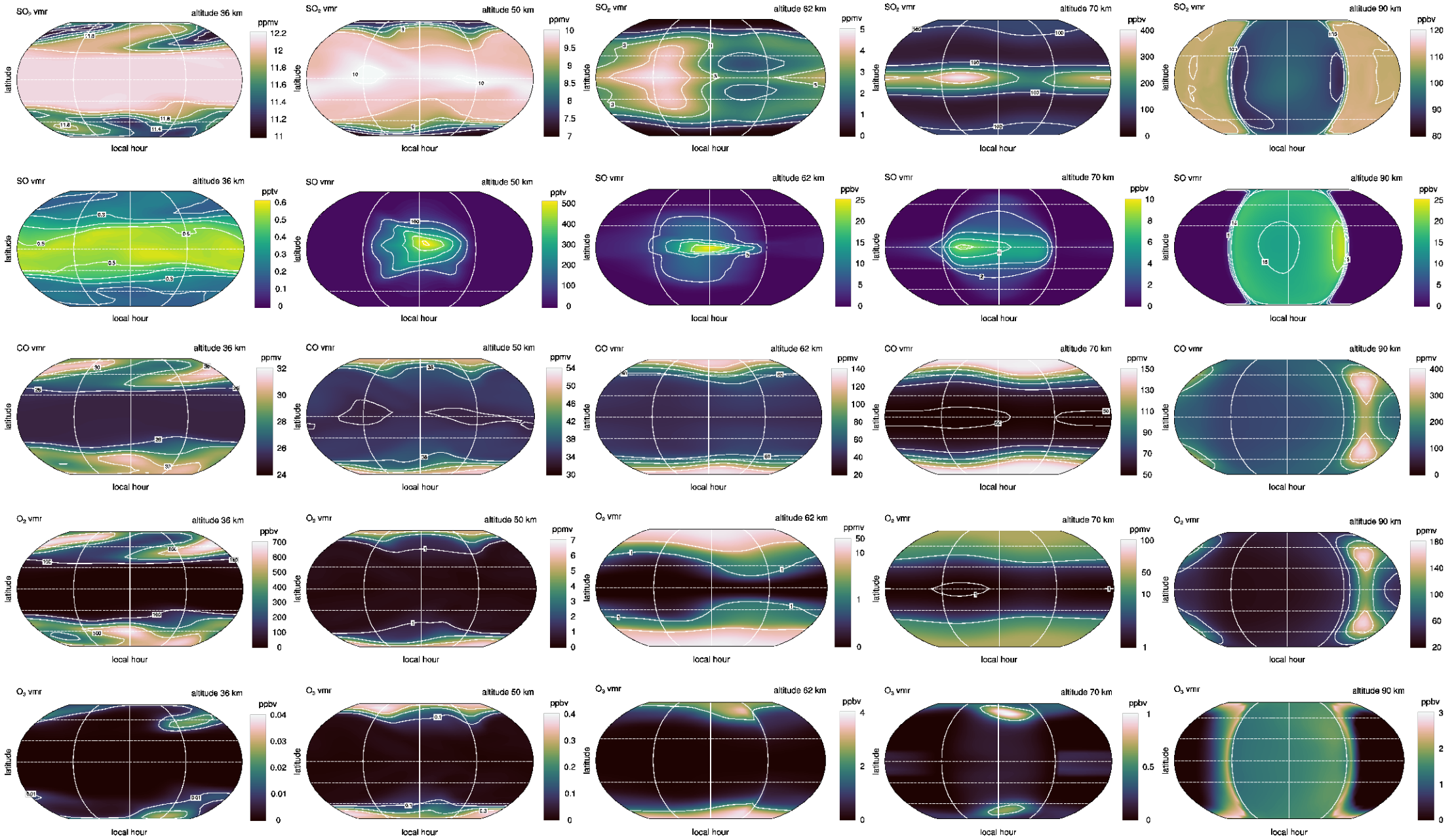

Atlas A: Atlas, pole-to-pole, of the volume mixing ratio of SO_2, SO, CO, O_2 and O_3 for different altitudes between 36 km and 90 km. The local time is noon at the central meridian. North pole is up and South pole is down. Meridians of East/morning terminator and West/evening terminator are also represented by solid white lines.

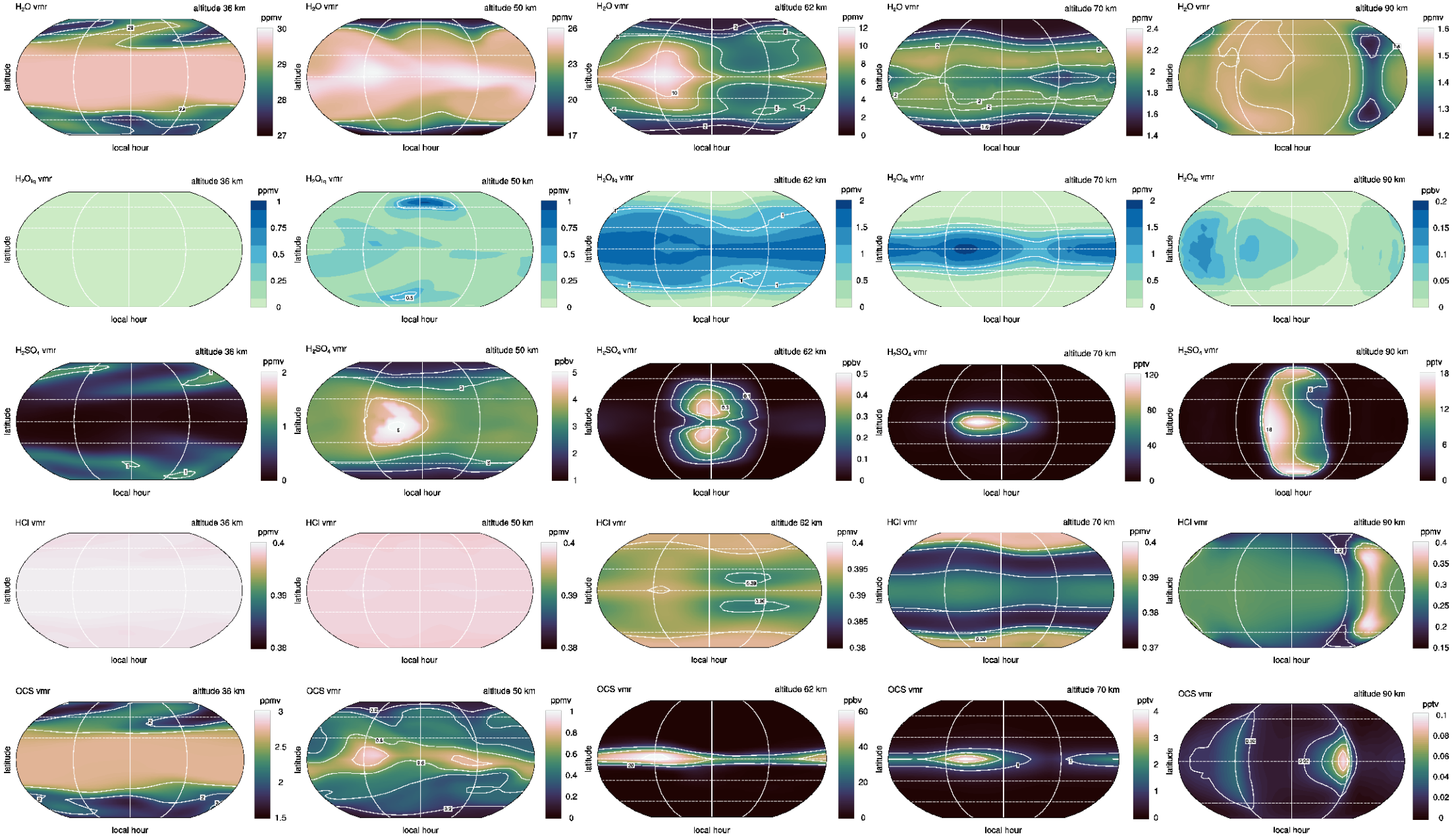

Atlas B: Atlas, pole-to-pole, of the volume mixing ratio of H_2O (gaseous and condensed), H_2SO_4 (gaseous), HCl and OCS for different altitudes between 36 km and 90 km. The local time is noon at the central meridian North pole is up and South pole is down. Meridians of East/morning terminator and West/evening terminator are also represented by solid white lines.

3. Results and discussion

3.1. Cloud characteristics

We present here the cloud characteristics calculated by the Venus PCM cloud model and compare them to available measurements of the H_2SO_4 weight fraction and total mass of aerosols.

3.1.1. H_2SO_4 weight fraction

Fig. 7 shows the zonally-averaged distribution of the aerosol H_2SO_4 weight fraction $w_{H_2SO_4}$ calculated by the Venus PCM. Near-pure H_2SO_4 aerosols ($w_{H_2SO_4} > 0.95$) are predicted in lower haze below 45 km. Above 45 km, in the lowest parts of the cloud deck, $w_{H_2SO_4}$ decreases rapidly to reach a minimum value of about 0.81 at 52 km. Above that altitude, $w_{H_2SO_4}$ remains smaller than 0.84 up to the top of the model at 90 km. Observations of $w_{H_2SO_4}$ at 50 km were performed by the TripleSpec instrument from Earth (Arney et al., 2014) and by VIRTIS-M onboard *Venus Express* (Barstow et al., 2012). Fig. 8 compares the globally-averaged vertical profile of $w_{H_2SO_4}$ calculated by the model to those observations. Arney et al. (2014) show a mean $w_{H_2SO_4}$ value around 0.8 with little latitudinal variation or of the order of the uncertainties. In contrast, Barstow et al. (2012) show a higher $w_{H_2SO_4}$ mean value around 0.9. Moreover, VIRTIS-M detects a significant latitudinal variation, going from ≈ 0.85 at the equator to $w_{H_2SO_4} \approx 0.90$ at 75°N. As shown in Fig. 7, our calculated $w_{H_2SO_4}$ does not vary much with latitude at 50 km.

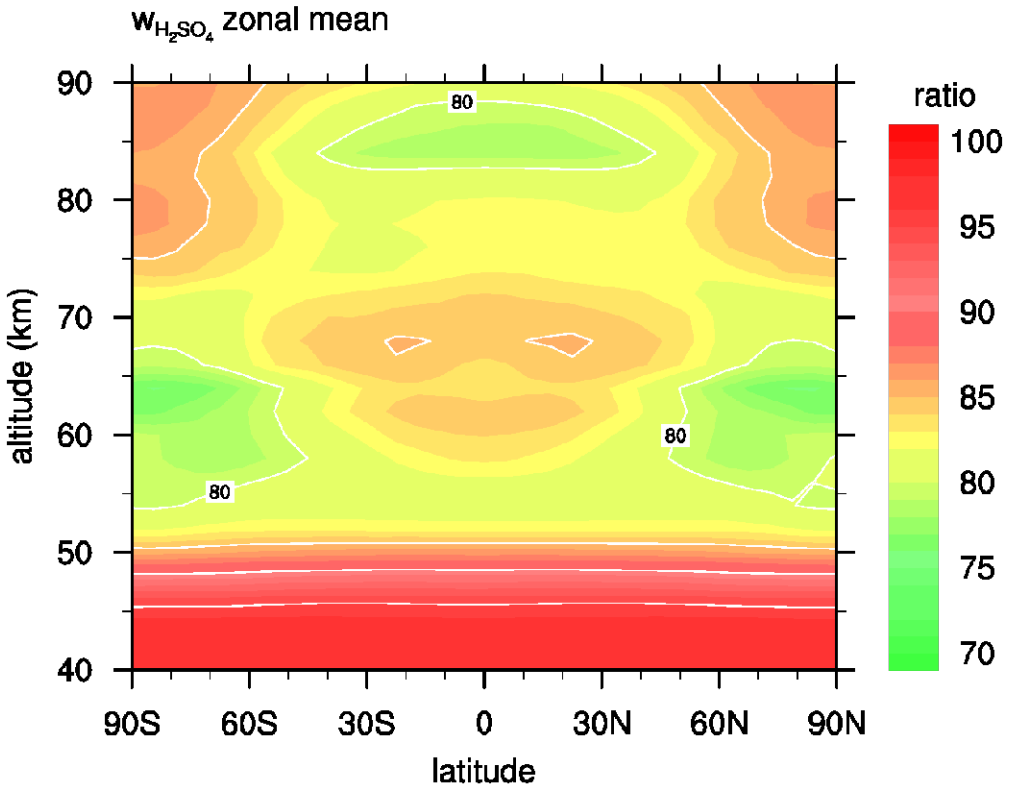

Figure 7: Zonally-averaged distribution of $w_{H_2SO_4}$, the aerosol H_2SO_4 weight fraction (multiplied by 100).

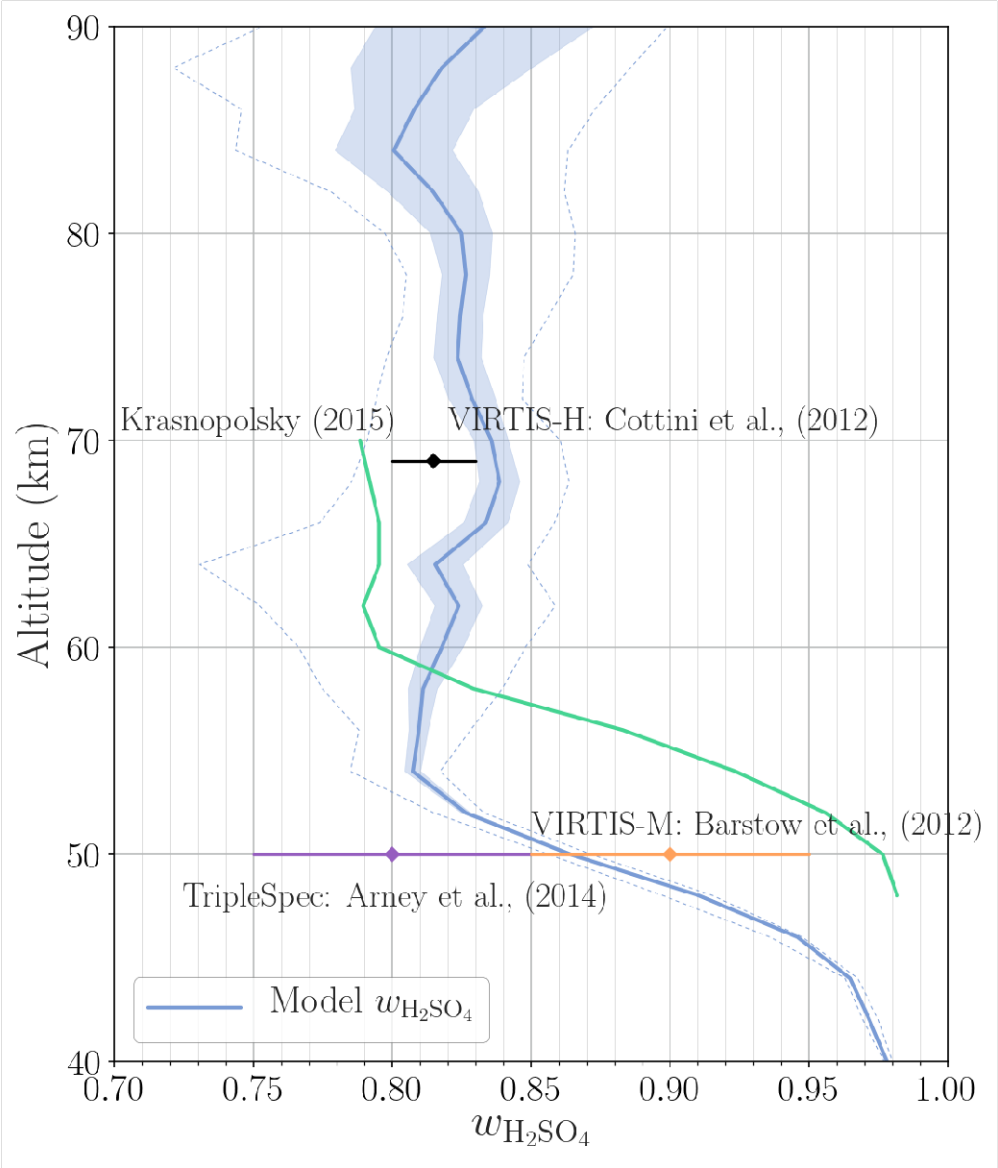

Figure 8: Globally-averaged vertical profile of $w_{H_2SO_4}$ calculated by the Venus PCM (blue curve) and compared to observations. (1) VIRTIS-H onboard *Venus Express* (Cottini et al., 2012) mean value ± maximum values for a latitudinal range 40°S–40°N. (2) TripleSpec Earth-based IR measurements (Arney et al., 2014). (3) VIRTIS-M onboard *Venus Express* (Barstow et al., 2012). (4) 1-D model of Krasnopolsky (2015).

The altitude domain around 50 km is close to the Lower Cloud Boundary (LCB) and is therefore a region of strong vertical gradient of $w_{H_2SO_4}$. Any temperature bias in the model can have important consequences on the results and the comparison with observed data should be considered with caution. In particular, the 30 K cold bias identified in the Venus PCM in Section 2.1 leads to an LCB that is about 5 km too low compared to the observations 42 km vs. 47 km). This explains the apparent disagreement in Fig. 8 with the 1D-model of Krasnopolsky (2015), which has an LCB at 47 km in good agreement with spacecraft data. The difference between both models can be entirely attributed to the too-low temperature in the Venus PCM, which has the effect of shifting the $w_{H_2SO_4}$ profile by 5 km downwards. Despite this difference in altitude, both models show a very similar vertical gradient of $w_{H_2SO_4}$ in the lower cloud and agree on the value calculated at the LCB: $w_{H_2SO_4}$ is equal to 0.97 at 42 km in the Venus PCM and 0.98 at 47 km in the 1D-model of Krasnopolsky (2015).

Near the cloud top at 70 km, our modeled mean value $w_{H_2SO_4} = 0.84$ is close to the one observed by Cottini et al.

(2012) with VIRTIS-H onboard *Venus Express*. Latitudinal changes in the modelled $w_{H_2SO_4}$ can be seen in Fig. 7. Cottini et al. (2012) observed a decrease of $w_{H_2SO_4}$ from $\approx$ 0.82 at the equator to slightly lower than 0.80 at 60 °N. Near the North pole the observed $w_{H_2SO_4}$ increased to $\approx$ 0.84. In Fig. 7, our model reproduces the latitudinal decrease from $\approx$ 0.84 at the equator to $\approx$ 0.80 at latitudes > 60 °N, in good agreement with Cottini et al. (2012). The model does not show however the steep increase of $w_{H_2SO_4}$ observed by VIRTIS-H near the north pole. The spatial resolution of the Venus PCM version used here might be too low to catch this feature, especially regarding the temperature field. Future simulations at higher spatial resolution will assess this issue.

3.1.2. Vertical structure of the clouds

Fig. 9 shows the vertical profile of the condensed mass calculated by the model. With the hypothesis of a mode 3' including a solid core as discussed in 2.3.5, we find that the Venus PCM reproduces rather successfully the only available measurements by the LCPS instrument (Knollenberg and Hunten, 1980). The mass of mode 1, mode 2, as well as the total mass are in reasonable agreement with the observations at all altitudes down to about 47 km. Below that level, a cold bias of about 30 K in the Venus PCM relative to the VIRA profile at the cloud base (Seiff et al., 1985) leads to a condensation that occurs too low in altitude and to the overestimation of the condensed mass compared to LCPS. This problem is therefore well understood and does not necessarily reflect poor conceptual modelling of the Venus clouds. It must be noted that the mass loading profile for mode 1 reconstructed from Table 4 of Knollenberg and Hunten (1980) is, above 60 km, larger by about a factor of 2 than that shown in their Fig. 18.

The vertical profiles of liquid and gas-phase H_2O and H_2SO_4 are compared to available observations in Fig. 10. Zonally-averaged distributions are shown in Fig. 11a and 11b. Maps at various levels are shown in Atlas B. From these results it can be seen that water in the liquid phase ($H_2O_{(l)}$) represents only 10% of total H_2O at 60 km and 20% at 70 km. The maximum mixing ratio of $H_2O_{(l)}$ contained in the clouds is around 1 ppmv between 60-65 km. Regarding the gas-phase, the decrease with altitude of $H_2O_{(g)}$ inside the clouds observed by Fedorova et al. (2016) is particularly well reproduced by the Venus PCM, which tends to corroborate the photochemical and microphysical treatment of water in the cloud deck. The comparison with observations of $H_2O_{(g)}$ below and above the clouds is further discussed in section 3.5.

The mixing ratio of condensed sulfuric acid $H_2SO_{4(l)}$ is close to that of liquid water $H_2O_{(l)}$ in the clouds with a maximum of 1 ppmv between 60-65 km (Fig. 10). This result is expected due to the monohydrate H_2SO_4-H_2O composition of the cloud droplets. However, unlike H_2O, sulfuric acid is entirely condensed in the Venus clouds and the gas-phase fraction $H_2SO_{4(g)}$ becomes negligible in the Venus PCM above 50 km. The comparison with available observations of $H_2SO_{4(g)}$ below the clouds will be discussed in Section 3.6.4.

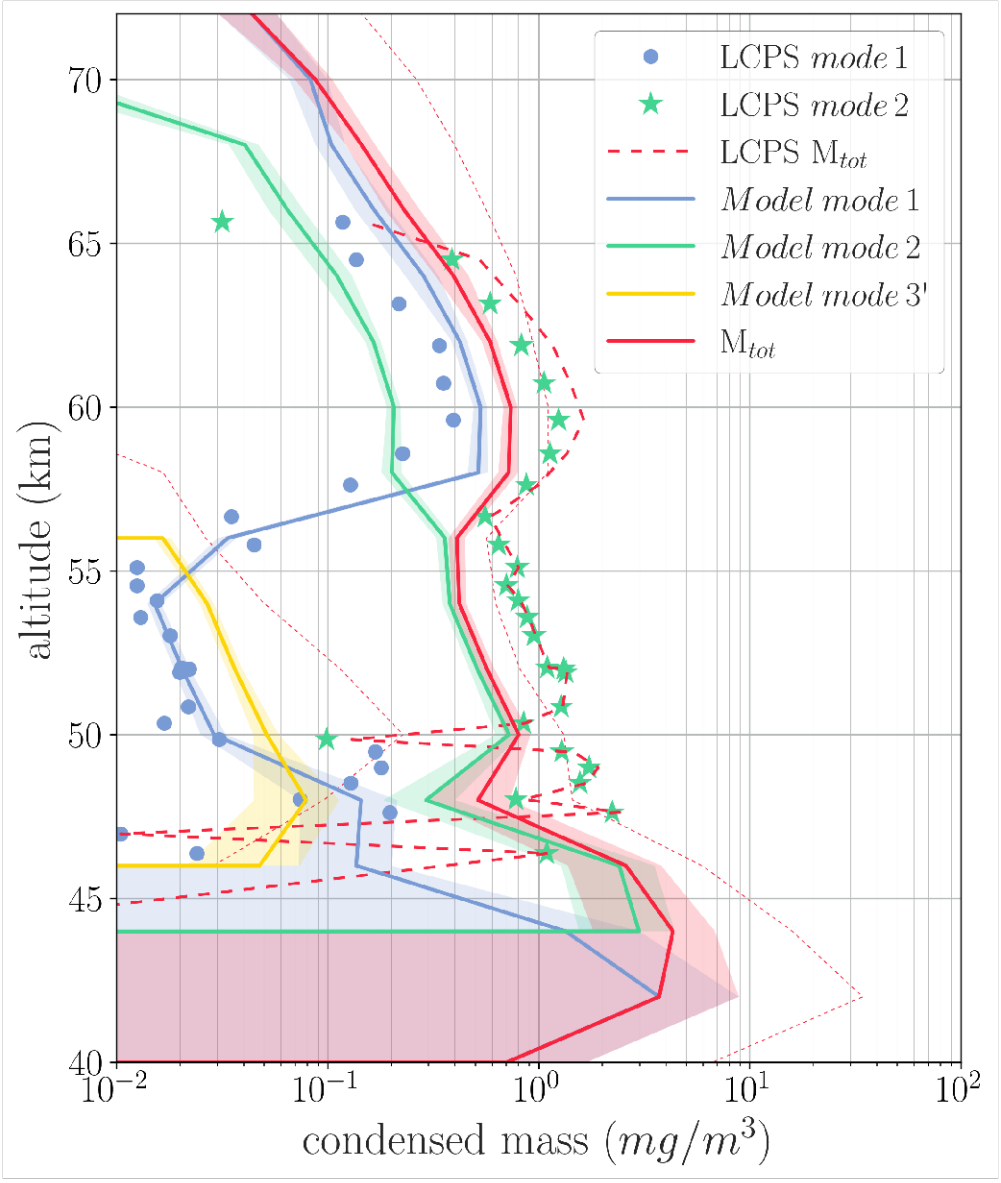

Figure 9: Condensed mass for each droplet mode, zonally-averaged over all latitudes, and compared to LCPS measurements. We use the size distribution parameters of Knollenberg and Hunten (1980) presented in their Table 4 to replicate the condensed mass vertical profile measured by LCPS. The exact same approach was used to evaluate the mass loading of each mode with LCPS data from Knollenberg and Hunten (1980) in McGouldrick and Toon (2007). M_{tot} refers to the total mass. The colored areas correspond to the standard deviation in latitude and local time. The dashed lines indicate the minimum and maximum values.

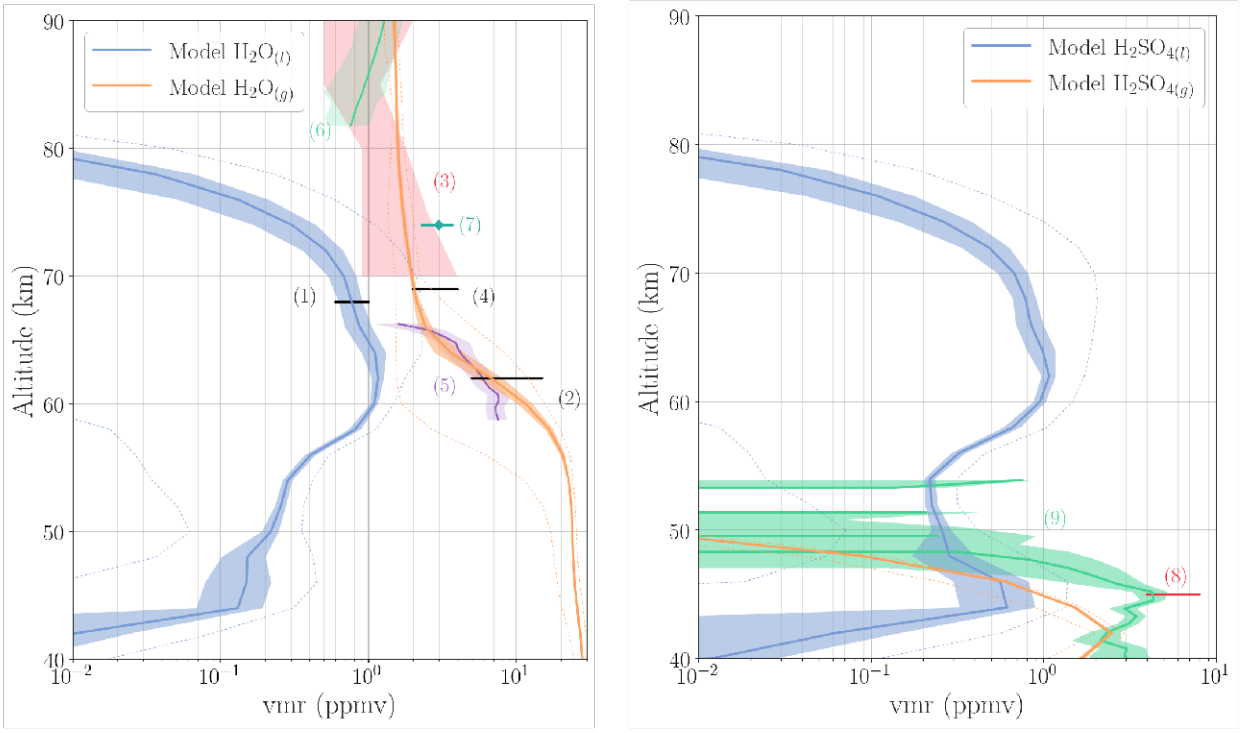

Figure 10: Globally-averaged vertical profiles of the liquid and gas phase of (a) H_2O and (b) H_2SO_4 calculated by the Venus PCM. The colored areas correspond to the standard deviation in latitude and local time. The dashed lines indicate the minimum and maximum values. Observations are: (1) IR Fourier spectrometer observations from Fink et al. (1972). (2) Fourier Spectrometer onboard the Venera 15 orbiter from Ignatiev et al. (1999). (3) SPICAV observations $\pm 1\sigma$ from Fedorova et al. (2008). (4) VEx VIRTIS-H observations from Cottini et al. (2012, 2015). (5) SPICAV IR on VEx $\pm 1\sigma$ from Fedorova et al. (2016). (6) SOIR mean vmr $\pm 1\sigma$ from Chamberlain et al. (2020). (7) Observations from CSHELL spectrograph at NASA IRTF (Krasnopolsky et al., 2013). (8) Multi-wavelength radio frequency observation at VLA from Jenkins et al. (2002). (9) *Venus Express* VeRa observations from Oschlisniok et al. (2021)

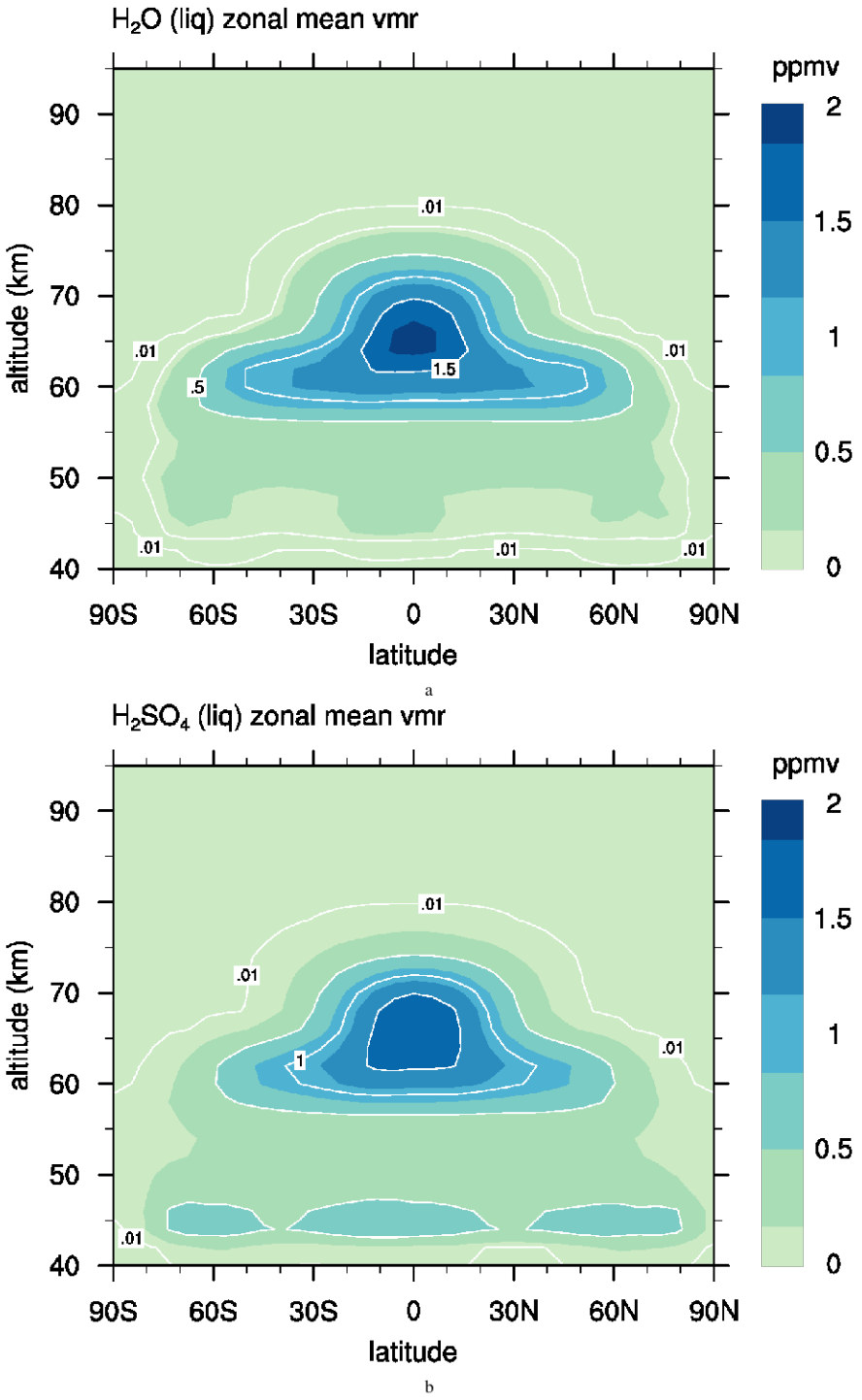

Figure 11: Zonally-averaged distribution of the liquid phase of H_2O (top) and H_2SO_4 (bottom). Unit is ppmv.

3.2. CO distribution

CO is the product of the photolysis of CO_2 in the upper layers of the Venus atmosphere. The CO zonally-averaged distribution, in Fig. 12 and Atlas A, reflects the production of CO at high altitudes, which is then transported by the

Hadley-type mean meridional circulation. Above the poles, the descending branch of the global meridional dynamics leads to an enrichment in CO in the mesosphere, a phenomenon that is typical of the distribution of all long-lived species in the Venus PCM.

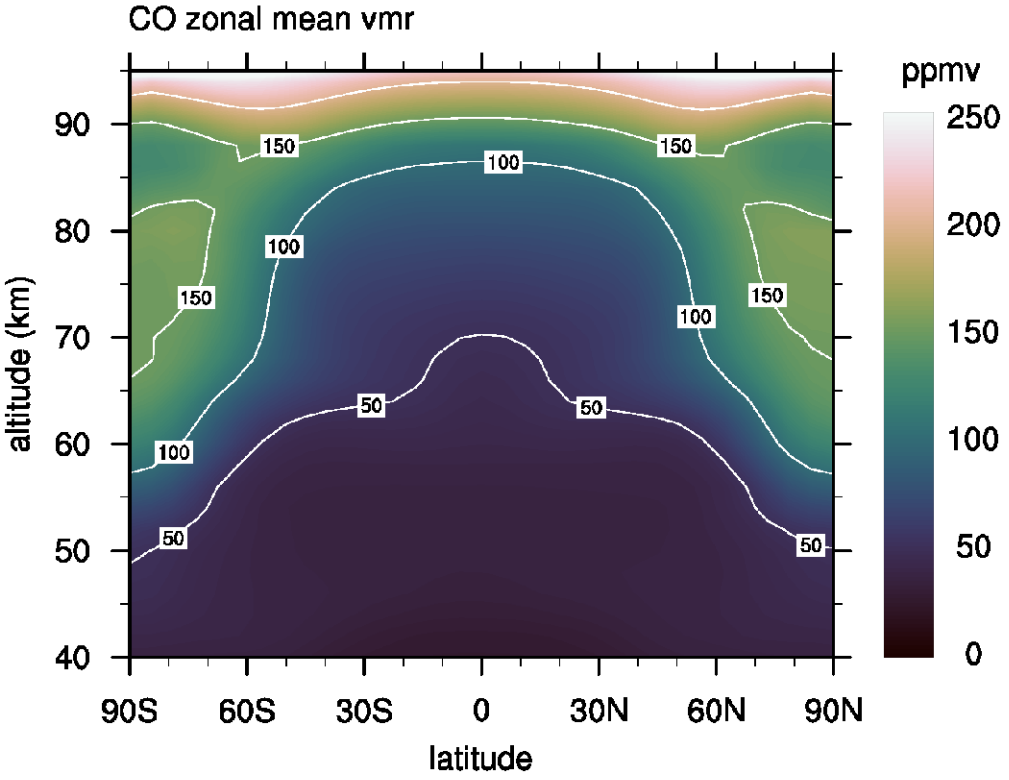

Figure 12: Carbon monoxide (CO) zonally-averaged mixing ratio. Unit is ppmv.

Near the cloud top (roughly from 65 km to 70 km), Irwin et al. (2008) found a CO vmr of 40 ± 10 ppmv for mid-latitudes using the spectrometer VIRTIS onboard *Venus Express*. At similar altitudes, Krasnopolsky (2010a) and Marcq et al. (2015) measured CO using the ground-based CSHELL spectrometer at the IRTF. Krasnopolsky (2010a) obtained CO mixing ratios of the order of 50 ppmv in the morning and 40 ppmv in the evening, whereas Marcq et al. (2015) reported values in the 25-45 ppmv range between 30ºN and 30ºS. At the cloud top, Connes et al. (1968) measured 45 ppmv of CO with a ground-based interferometer. These measurements of CO are compared to the Venus PCM in Fig. 13. The modeled CO mixing ratio between 30ºS and 30ºN is in general close to the observations. As observed by Krasnopolsky (2010a), the Venus PCM produces a slight increase in CO around the morning terminator (see Atlas A). In the model, this effect results from the diurnal thermal tide producing a downward motion of CO-rich air in the morning, and an opposite upward motion of CO-poor air in the evening.

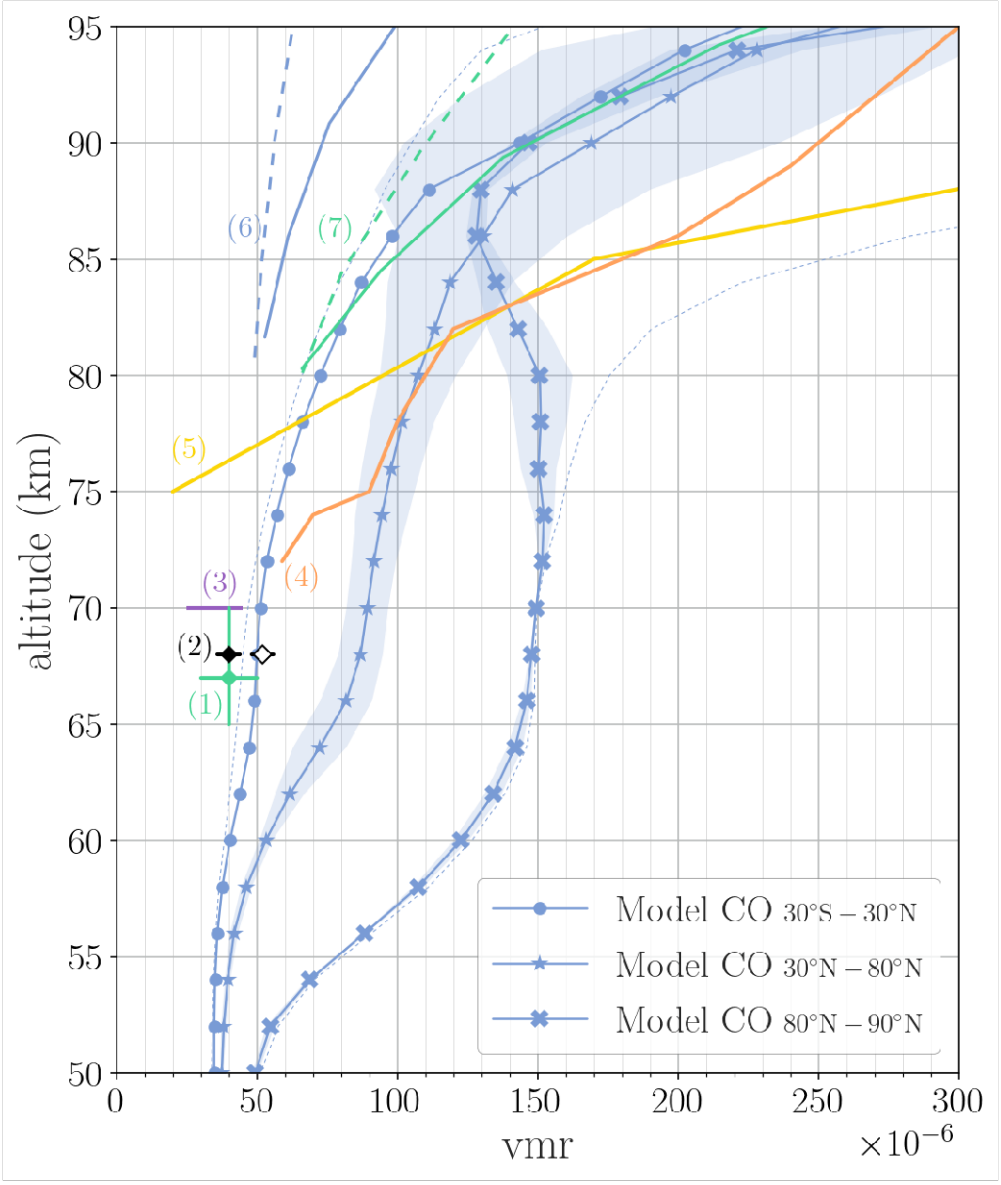

Figure 13: Observed and modelled vertical profile of CO. Blue curves: zonally-averaged Venus PCM profile. The colored areas correspond to the standard deviation in latitude and local time. The dotted lines indicate the minimum and maximum values. Circles: low latitudes (30ºS to 30ºN). Stars: mid-to-high latitudes (30ºN-80ºN). Crosses: Polar latitudes (80ºN-90ºN). The observations of CO are: (1) VEX/VIRTIS-M Irwin et al. (2008) ; (2) IRTF/CSHELL Krasnopolsky (2010a) observations near terminator. White: Morning. Black: Evening ; (3) IRTF/CSHELL Marcq et al. (2015) ; (4) VEX/SOIR Vandaele et al. (2016) vertical profile from 70° to 80° of latitude ; (5) IRAM ground-based mm-wave measurements Lellouch et al. (1994) ; (6) JCMT sub-mm measurements 2000-2002 disk average night/day (plain/dashed) Clancy et al. (2012). (7) JCMT sub-mm measurements 2007-2009 disk average night/day (plain/dashed) Clancy et al. (2012).

The mean CO profile calculated by the Venus PCM is also compared in Fig. 13 to various observations of the CO vertical distribution in the mesosphere (70-95 km). The measurements considered here are the IRAP millimeter-wave observations by Lellouch et al. (1994), the JCMT sub-millimiter data by Clancy et al. (2012), as well as the mean profile determined by the SOIR instrument onboard *Venus Express* (Vandaele et al., 2016). In general the observed CO in the Venus mesosphere displays a strong variability, with short term changes that can reach one order of magnitude on less than one month periods as shown by SOIR (Vandaele et al., 2016). This variability is less pronounced in the Venus PCM but, in average, the model calculates a CO vertical profile that is in good agreement with the mean

SOIR profile between 70°N-80°N (Fig. 13). Thus, in the light of the CO data currently available, our results suggest that full chemistry of the CO_2 cycle as implemented in the Venus PCM leads to a reasonable agreement with the observations. Regarding the ground-based observations, the mean CO vmr calculated by the model is between the values of Lellouch et al. (1994) and those of Clancy et al. (2012). Above 90 km, the distribution of CO starts to be influenced by thermospheric transport characterized by a rapid subsolar-to-antisolar circulation, named hereafter SS-AS (e.g., Clancy and Muhleman (1985)). This effect is somewhat visible in Atlas A, where nighttime CO values are significantly larger than during the day at 90 km. Nevertheless, a full description of the SS-AS transport obviously requires the extension to the thermosphere of the Venus PCM, as described by Gilli et al. (2017). In the absence of such extension in the version of the Venus PCM used here, the comparison between the observed and modeled CO values near the model top at 90-95 km must therefore be viewed with caution. For a detailed comparison of CO with available observations in the thermosphere, the reader is invited to consult the studies by Gilli et al. (2017) carried out with the same horizontal resolution as the present work (7.5°x5.6°) and by Gilli et al. (2021) at the increased resolution of 3.7°x1.9°.

3.3. Oxygen species

3.3.1. Ground-state molecular oxygen O_2

Above the clouds and up to 80 km, the main production path for molecular oxygen is the catalytic cycle involving the chlorine radicals Cl and ClO:

$$\begin{array}{rl} & Cl + O_3 \longrightarrow ClO + O_2 \\ & ClO + O \longrightarrow Cl + O_2 \\ \hline NET\ : & O + O_3 \longrightarrow 2\,O_2 \end{array} \tag{18}$$

Above 80 km, O_2 is mainly produced by the three-body association reaction:

$$O + O + CO_2 \longrightarrow O_2 + CO_2 \tag{19}$$

The efficiency of this reaction increases with altitude and explains the maximum O_2 volume mixing ratios approaching 100 ppmv at the top of the Venus PCM (see Fig. 14). O_2 is a long-term species as its photochemical lifetime varies between more than 10 venusian days (more than a thousand Earth days) at the cloud top to about a month around 90 km. Owing to this long photochemical lifetime, O_2 is transported downwards from the altitudes of production to the polar regions by the Hadley circulation. Thus, a general increase in O_2 with latitude is found down to altitudes of about 55 km in the model. Above the clouds, typical O_2 volume mixing ratios in the polar regions are of the order of 50 ppmv (see Fig. 14).

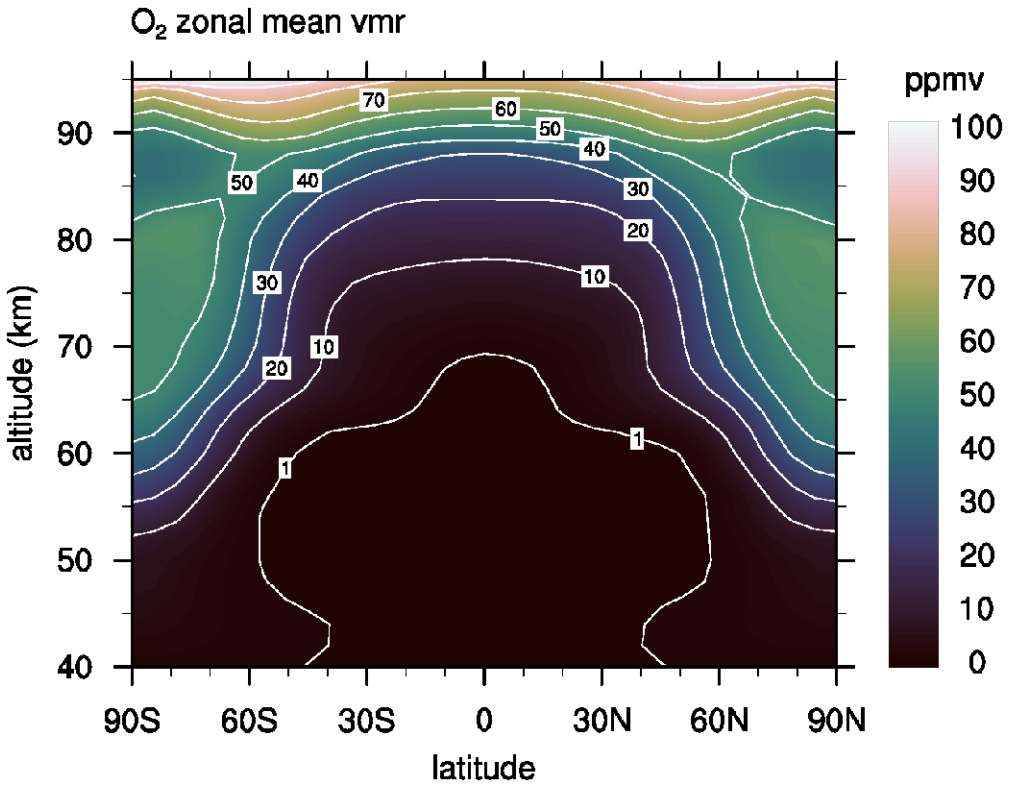

Figure 14: Molecular oxygen (O_2) zonally-averaged mixing ratio. Unit is ppmv.

Up to now, attempts to detect ground-state O_2 in the atmosphere of Venus have remained unsuccessful (Traub and Carleton, 1974; Trauger and Lunine, 1983; Mills, 1999). Using the HRF spectrometer of the *Anglo-Australian Observatory*, Mills (1999) calculated an upper limit for O_2 of 3 ppmv above 58 km and of 10 ppmv below 52 km. Although this latter observational constrain is met by the Venus PCM (about 1 ppmv is obtained at 52 km for mid latitudes), the model calculates O_2 mixing ratios that are much larger than 3 ppmv above 58 km, with vmr above 10 ppmv at mid latitude at the the cloud top and a background 20 ppmv minimum everywhere with peaks at 180 ppmv at 90 km (see Atlas A). The high O_2 amount is shared by all other photochemical models described in the literature (Yung and DeMore, 1982; Mills et al., 2013; Zhang et al., 2012; Krasnopolsky, 2012b; Parkinson et al., 2015; Bierson and Zhang, 2020; Shao et al., 2020) and calls for new attempts to detect ground-state O_2 on Venus in order to clarify a situation in stark contradiction with the current understanding of O_2 chemistry.

3.3.2. Ozone O_3

As in the Earth's stratosphere, ozone on Venus is quickly destroyed by the cycle (18) catalyzed by chlorine radicals. This cycle is mostly efficient above 70 km where ClO is the most abundant.

The discovery of ozone at cloud tops altitude was made with the SPICAV-UV experiment in nadir mode onboard *Venus Express* by Marcq et al. (2019). O_3 detection took place at high latitudes (> 50º) of both hemispheres. Northern and southern ozone amounts are comparable with an average mixing ratio of $11.4^{+4.2}_{-3.3}$ ppbv and $9.4^{+4.3}_{-3.7}$ ppbv respectively. This ozone layer restricted to high latitudes is predicted by the Venus PCM in the altitude range of 55-65 km as shown in Atlas A and in Fig. 15. Around 60 km, O_3 accumulates at latitudes greater than 40° due to the coincidence of O_2-rich air in the descending branch of the Hadley circulation and the large pressure at the cloud top increasing the rate of the third-body reaction $O + O_2 + M \longrightarrow O_3 + M$. This behavior is similar in nature to the polar ozone layer observed on Mars by Montmessin and Lefèvre (2013). Nonetheless, the ozone mixing ratio retrieved at the Venus cloud tops by Marcq et al. (2019) is about five times greater than the amount calculated by the Venus PCM. This quantitative discrepancy could be explained by an overestimation of the O_3 loss mechanism or an underestimation of

the O_2 amount at the cloud top in the Venus PCM. The latter hypothesis seems less reliable since the O_2 vmr in the Venus PCM at the cloud tops already exceeds the observational constrain of 3 ppmv (Mills, 1999).

Using SPICAV-UV in stellar occultation mode, Evdokimova et al. (2021) detected ozone down to 85 km on the night-side of Venus. Ozone measurements are sporadic and mostly occur at 30ºN ± 10º. The measured mixing ratios are between 1-30 ppbv at 85-90 km and 6-120 ppbv at 100-105 km. But, as mentioned in Evdokimova et al. (2021), those values are mostly representative of the ozone peak and do not represent the average content of ozone on the night-side of Venus. Nonetheless, the increase in the O_3 mixing ratio with altitude observed by SPICAV-UV is expected from a chemical species that is a side-product of CO_2 photodissociation. This behavior is reproduced by the Venus PCM as seen in Fig. 15, but the maximum O_3 mixing ratios do not reach the values measured at 85-90 km by Evdokimova et al. (2021). It is likely, however, that the accuracy of the model values is limited by the proximity of the model top at 95 km. We also note the absence of O_3 predicted by the Venus PCM near the antisolar point in Atlas A, a characteristic also found with SPICAM-UV by Evdokimova et al. (2021).

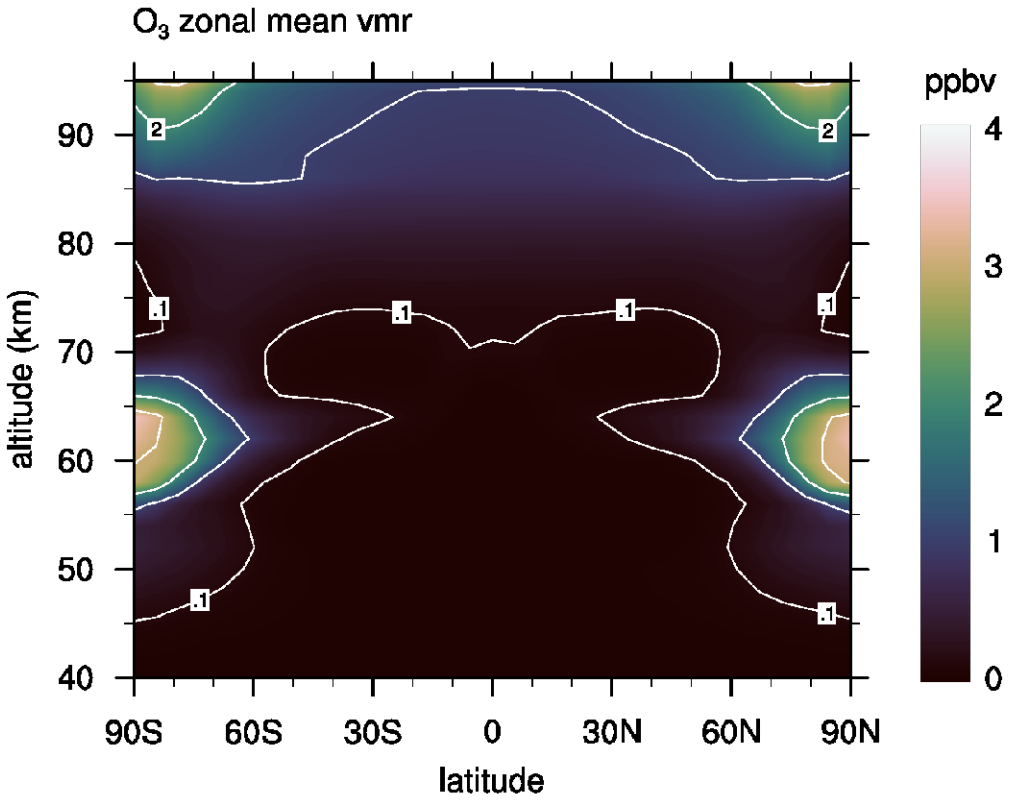

Figure 15: Ozone (O_3) zonally-averaged mixing ratio. Unit is ppbv.

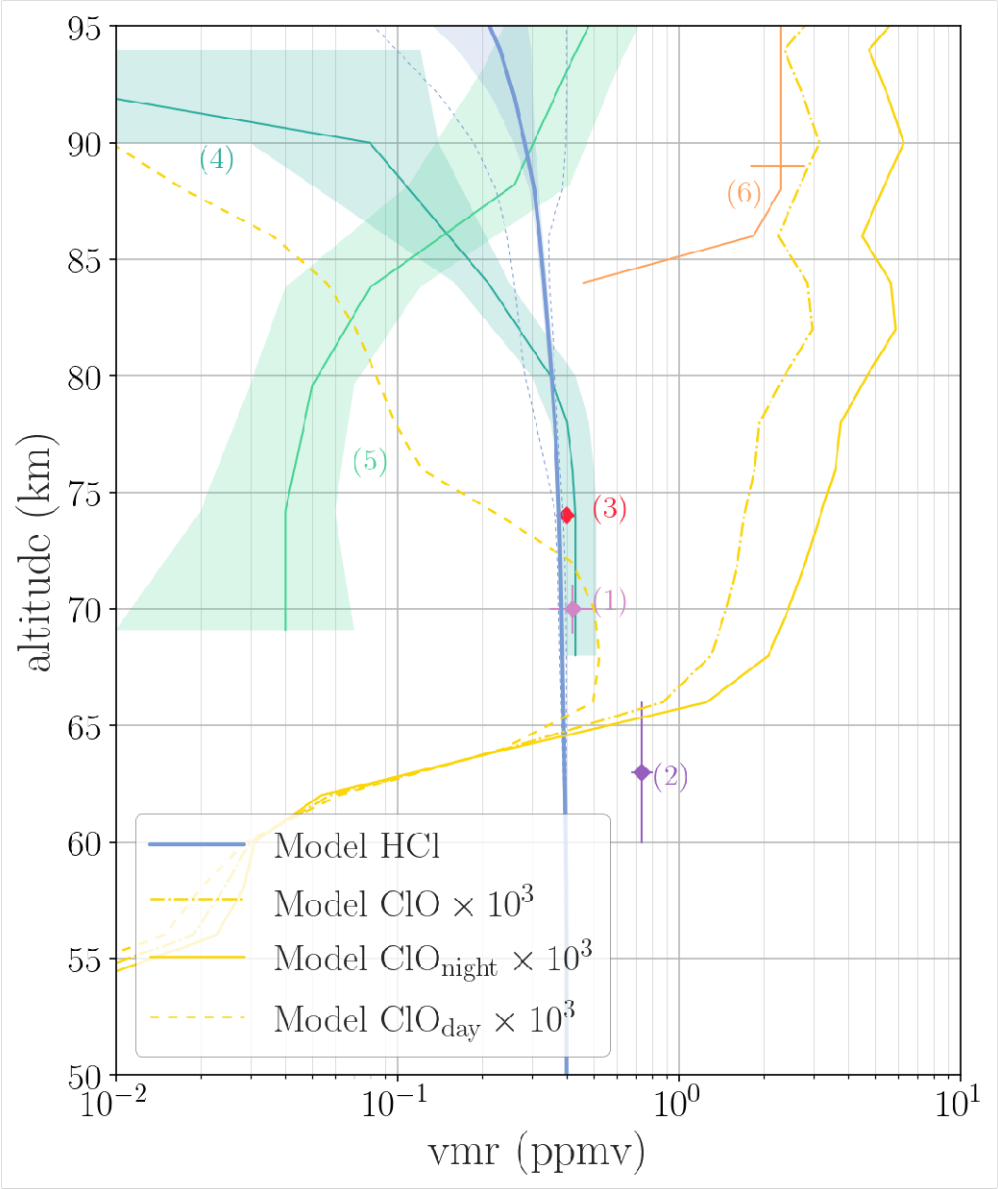

Figure 16: Modeled and observed HCl and ClO mixing ratio (ppmv) (ClO vmr is plotted $\times 10^3$ to fit in the same figure.). Blue curve: Venus PCM zonal mean averaged over all latitudes. The colored envelope correspond to the standard deviation in latitude and local time. The dotted lines represent the minimum and maximum values. Yellow curves: ClO Venus PCM zonal mean averaged over all latitudes with night/day as dashed/plain lines. The observations of HCl are: (1) Ground-based measurements compilation review (Young, 1972). (2) Ground-based IR spectroscopy (Iwagami et al., 2008). (3) CSHELL spectrograph at NASA IRTF (Krasnopolsky, 2010a). (4) Ground-based sub-mm observations at JCMT. Averaged vertical profile $\pm 1\sigma$ from Sandor and Clancy (2012). (5) SOIR vertical profile $\pm 1\sigma$ from Mahieux et al. (2015b). The observation of ClO is: (6) Ground-based sub-mm measurement of ClO (units in **ppbv**) in the night-side of Venus mesosphere using the James Clerk Maxwell Telescope (JCMT) from Sandor and Clancy (2018)

3.4. Chlorine species

Hydrogen chloride HCl is in principle the main reservoir of atmospheric chlorine on Venus and the source of Cl, ClO, ClCO and $ClCO_3$ through its photodissociation. Those short-lived chlorine species are believed to play a major role in the cycles of reactions that convert CO and O_2 into CO_2, although the precise identity of the so-called CO_2 cycle has not been resolved yet (see the reviews of Mills and Allen (2007); Marcq et al. (2018)).

3.4.1. Hydrogen chloride HCl*:*

The first ground-based measurements of HCl were carried out by Connes et al. (1967). The data were later corrected by Young (1972), who concluded to a HCl mixing ratio of 400 ± 70 ppbv at the cloud top. Using ground-based IR spectroscopy, Iwagami et al. (2008) found 740 ppbv ± 60 of HCl between 60-66 km. Krasnopolsky (2010a) measured the HCl mixing ratio to be 400 ppbv ± 30 near 74 km using the CSHELL spectrograph at IRTF. Sandor and Clancy (2012) observations at JCMT could determine the HCl vertical profile above the clouds. The mixing ratio ranged from 400 ppbv at the cloud top to less than 100 ppbv above 90 km. Therefore, the current consensus that emerges from ground-based data suggests a mixing ratio of about 400 ppbv below 75 km, although the measurements of Iwagami et al. (2008) disagree with that value.

The only satellite observations of HCl were provided by the SOIR instrument onboard *Venus Express* (Mahieux et al., 2015b). The HCl mean mixing ratio measured by SOIR near 70 km is smaller than that from ground-based observations by almost one order of magnitude (Fig. 16). Furthermore, SOIR detects an increase in HCl by a factor of 20 between 70 and 110 km, in stark disagreement with the ground-based sub-mm observations of Sandor and Clancy (2012). This discrepancy between the SOIR and the ground-based observations is up to now unexplained.

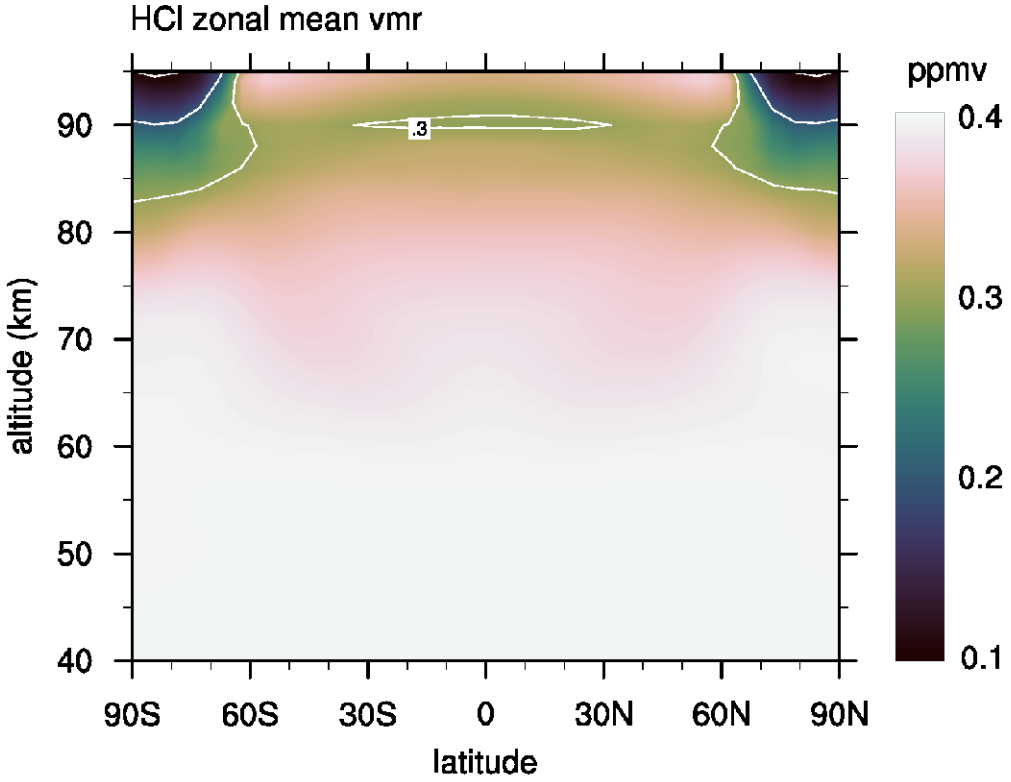

Figure 17: Hydrogen chloride (HCl) zonally-averaged mixing ratio. Unit is ppmv

The conventional chemistry implemented in the Venus PCM leads to a long lifetime for HCl below 75 km. Hence, at those altitudes, HCl is well-mixed in the Venus PCM. The HCl mixing ratio is uniform and remains equal to the initial value chosen at the beginning of the simulation, i.e. 400 ppbv as measured by ground-based instruments (Figs. 16 and 17). Above 75 km, the effect of HCl photolysis becomes visible in the Venus PCM. HCl shows a slight decrease up to the top of the model, where it is also affected by the SS-AS circulation (Atlas B). The HCl vertical distribution calculated by our model is in a good agreement with previous modelling studies (Krasnopolsky, 2012b; Zhang et al., 2012; Bierson and Zhang, 2020), but the HCl decrease near the model top is less pronounced than measured at sub-mm wavelengths by Sandor and Clancy (2012).

In contrast to the broad agreement found between the Venus PCM and the ground-based measurements of HCl, the shape of the modeled HCl profile is in clear disagreement with the SOIR data. If the HCl profiles measured by

SOIR data are confirmed to be representative of the standard HCl distribution, this would imply the existence of a strong sink of HCl near 70 km and a strong source near 100 km. Such processes are currently unknown. Further work is therefore needed to reconcile the HCl measurements and clarify an issue that could imply a deep reconsideration of our understanding of chlorine chemistry on Venus.

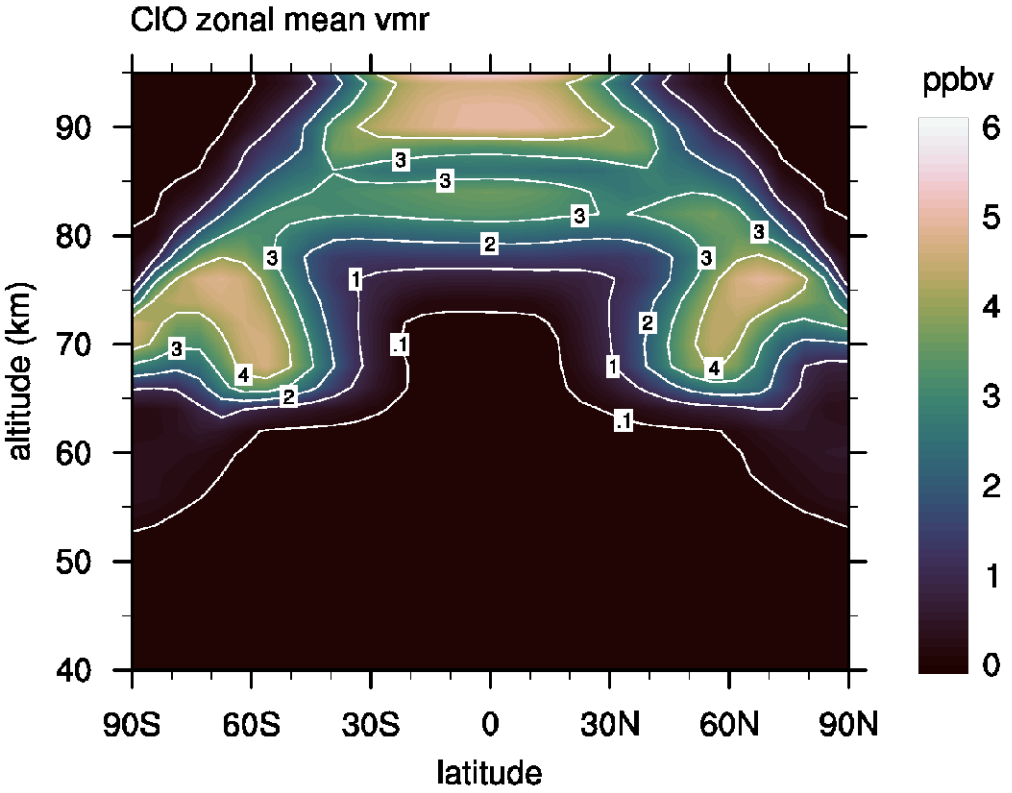

Figure 18: Chlorine monoxide (ClO) zonally-averaged mixing ratio. Unit is ppbv

3.4.2. Chlorine monoxide ClO

Chlorine atoms Cl and chlorine monoxide ClO are the primary products of HCl photochemistry above the Venus clouds. First measurements of ClO on Venus were carried out with the JCMT telescope by (Sandor and Clancy, 2018) who observed a mean mixing ratio of 2.6 ± 0.6 ppbv in the night-side mesosphere. The lower bound of the ClO layer was observed to be around 85 km. In general, ClO is a highly reactive species and is mainly influenced by the catalytic cycle of chlorine already mentioned in Eq. (18). Furthermore, the ClO mixing ratio is also affected by the products of SO_2 photolysis through SO and $ClSO_2$, which are important in determining the ClO amount at altitudes between 60-75 km. At low-to-mid latitudes, the ClO distribution calculated by the Venus PCM shows a mesospheric layer of ClO located between 80-95 km, in fairly good agreement with the observations by Sandor and Clancy (2018) and with mixing ratios of 2 to 6 ppbv. In the night-side of Venus, the modelled ClO mixing ratio is about two times larger than measured by Sandor and Clancy (2018) (see Fig. 16). According to Krasnopolsky (2012b), the reaction $NO + ClO \longrightarrow NO_2 + Cl$, not considered here, contributes to the loss of ClO and might explain the overestimation of ClO in the model. The decrease in ClO measured below 85 km by Sandor and Clancy (2018) is also represented by the model at mid-latitude (see Fig. 18) but is not as sharp as the observations suggest. The model also predicts the presence of a lower ClO layer restricted to high latitudes between 65-75 km. These polar layers of ClO are correlated to the slightly larger HCl mixing ratios visible in Fig. 17.

3.5. Water vapor $H_2O_{(g)}$

Water vapor on Venus is closely linked to two processes: the reaction with SO_3, leading to the production of H_2SO_4, and the simultaneous condensation of $H_2O_{(g)}$ and $H_2SO_{4(g)}$ in the form of binary liquid aerosols. From

a photochemical point of view though, the former process is slow, and $H_2O_{(g)}$ can be considered as a long-lived chemical species from the ground to about 90 km.

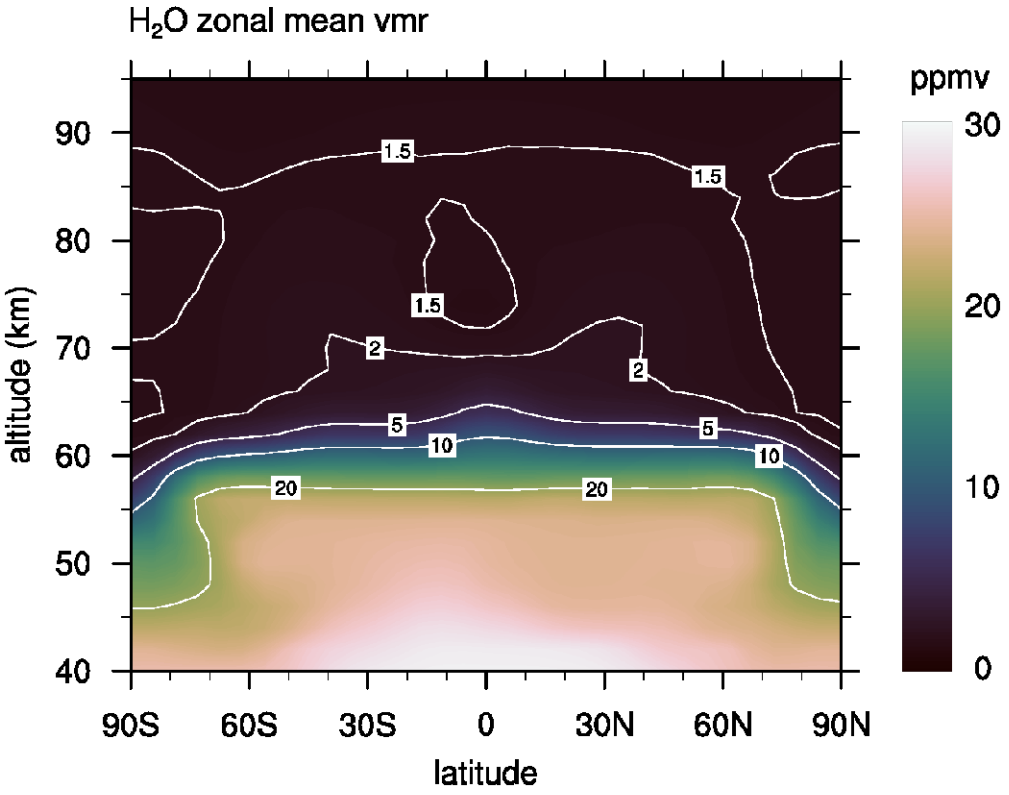

Figure 19: Gas-phase H_2O zonally-averaged mixing ratio. Unit is ppmv

Observations of the night side of Venus in the 2.3 µm band allows retrieving the $H_2O_{(g)}$ content below the clouds. Bézard et al. (1993); Crisp et al. (1991) and Pollack et al. (1993) found a mean mixing ratio around 30 ppmv below the cloud deck. Those measurements did not show a clear latitudinal variation and Drossart et al. (1993) concluded that those variations cannot exceed 10%. The 2.3 µm window was also used by the VIRTIS-H spectrometer onboard *Venus Express*, from which Marcq et al. (2008) found a mean $H_2O_{(g)}$ mixing ratio of 31 ± 2 ppmv below the clouds. In Fig. 19, The Venus PCM simulation also reproduces a roughly uniform $H_2O_{(g)}$ mixing ratio below the clouds, with only a moderate latitudinal variation caused by the Hadley cell circulation, in agreement with Drossart et al. (1993). The modelled low-to-mid latitudes mixing ratio is close to 30 ppmv and decreases to 27 ppmv at high latitudes.

Inside the cloud deck and at the cloud tops, retrievals of $H_2O_{(g)}$ have been performed by airborne infrared observations from the Earth (Fink et al., 1972), IR observation from the Earth with IRTF/CSHELL (Krasnopolsky et al., 2013), and from the Venus orbit with *Venera 15* (Ignatiev et al., 1999), *Venus Express*/VIRTIS-H (Cottini et al., 2012, 2015) and *Venus Express*/SPICAV IR (Fedorova et al., 2008, 2016). These data show that the $H_2O_{(g)}$ mixing ratio rapidly decreases from about 10 ppmv near 60 km to 1 ppmv close to the cloud top at 70 km. As seen earlier, this strong vertical gradient is satisfactorily reproduced by the Venus PCM (Fig. 10) and results in the model from the combined effect of the reaction with SO_3 and the condensation in the droplets. Thus, the Venus cloud deck acts as a barrier for water vapor that blocks about 90% of the quantity present in the lower atmosphere. One-dimensional models (Krasnopolsky, 2012a; Zhang et al., 2012; Bierson and Zhang, 2020; Shao et al., 2020, 2022) previously reproduced this decrease but the Venus PCM is the only model that tracks the liquid fraction of H_2O in the cloud droplets.

In the mesosphere, measurements of water vapor by SPICAV (Fedorova et al., 2008) and SOIR (Chamberlain et al., 2020) on *Venus Express* or ALMA (Encrenaz et al., 2015) show an average amount of 1 to 2 ppmv, with no

significant spatial variation with latitude. These observations are well reproduced by the Venus PCM, which shows an almost uniform H_2O mixing ratio of 1.5-2.0 ppmv from 70 km up to the top of the model (Fig. 19). At a given altitude, only a slight decrease is visible at high latitudes caused by the Hadley mean meridional circulation (Atlas B). However, the variability of H_2O with time is weaker in the Venus PCM than that measured with SOIR (Chamberlain et al., 2020) and by ground-based sub-millimeter measurements (Sandor and Clancy, 2005; Gurwell et al., 2007). The only noticeable short-timescale H_2O variation in the model is caused by the diurnal tide, leading to an upward flux of H_2O-rich air in the afternoon and increased mixing ratios at the cloud tops.

3.6. Sulfur species

3.6.1. Sulfur dioxide SO_2

Following the Venus Express mission and observations performed from the Earth, large progress have recently been achieved in the knowledge of the SO_2 distribution.

At the cloud top, measurements from SPICAV-UV (Marcq et al., 2020) and TEXES (Encrenaz et al., 2020) both indicate strong variations of SO_2 in time and space, with typical mixing ratios ranging from 10 pptv to a few hundred pptv. The statistical analysis of these data shows a general decrease in the SO_2 mixing ratio towards the poles. At low-to-mid latitudes, a SO_2 minimum is observed between 10 and 14 hour local solar time (LST), in contrast to a maximum at the terminators (Marcq et al., 2020; Encrenaz et al., 2020). Fig. 20 compares the Venus PCM SO_2 vertical distribution to available observations. At 70 km, the globally-averaged SO_2 mixing ratio calculated by the model is around 150 ppbv. This falls between the mean values determined by Marcq et al. (2020) and Encrenaz et al. (2020) and within the large range of mixing ratios determined from earlier SO_2 measurements (Esposito et al., 1997).

We find, however, that the mean equilibrium value of SO_2 at the cloud tops is very sensitive in our simulations to the initial values of SO_2 and H_2O adopted in the deep atmosphere. Similarly to Krasnopolsky (2012b) and Parkinson et al. (2015), a slight increase (10%) in SO_2 at the bottom of the clouds can quickly lead to a "runaway" effect such as SO_2 gets oxidized to SO_3 and exhausts all the available H_2O to form H_2SO_4. Deprived of its main photochemical sink, the SO_2 transported upwards from the deep layers can then freely pass through the cloud layer without being condensed into H_2SO_4, leading to highly overestimated SO_2 quantities in the mesosphere. The profiles of sulfur species obtained here are therefore the result of a subtle balance between the fine tuning of initial SO_2 and H_2O in the deep atmosphere, the vertical transport velocity, and the rate of H_2SO_4 formation in the cloud layers. On the quasi-horizontal plane, the poleward decrease of SO_2 is reproduced by the Venus PCM up to about 65 km (see Fig. 20 and Atlas A). This phenomenon is caused by the downwelling motion above the poles associated to the Hadley circulation, bringing down air poorer in SO_2 from the upper atmosphere. At low-to-mid latitudes, in agreement with the observations (Marcq et al., 2020; Encrenaz et al., 2020), the model also shows at the cloud tops a distinct SO_2 minimum between 10-14 LST, followed by a maximum in late afternoon until sunset. At these altitudes, the photochemical variation of SO_2 with local time is negligible and the changes calculated by the Venus PCM are entirely of dynamical origin. They result in the model from the upward transport of SO_2-rich air forced by the diurnal thermal tide, combined with the horizontal transport by the strong easterly winds at the cloud tops, which shift the SO_2 maximum towards the sunset terminator.

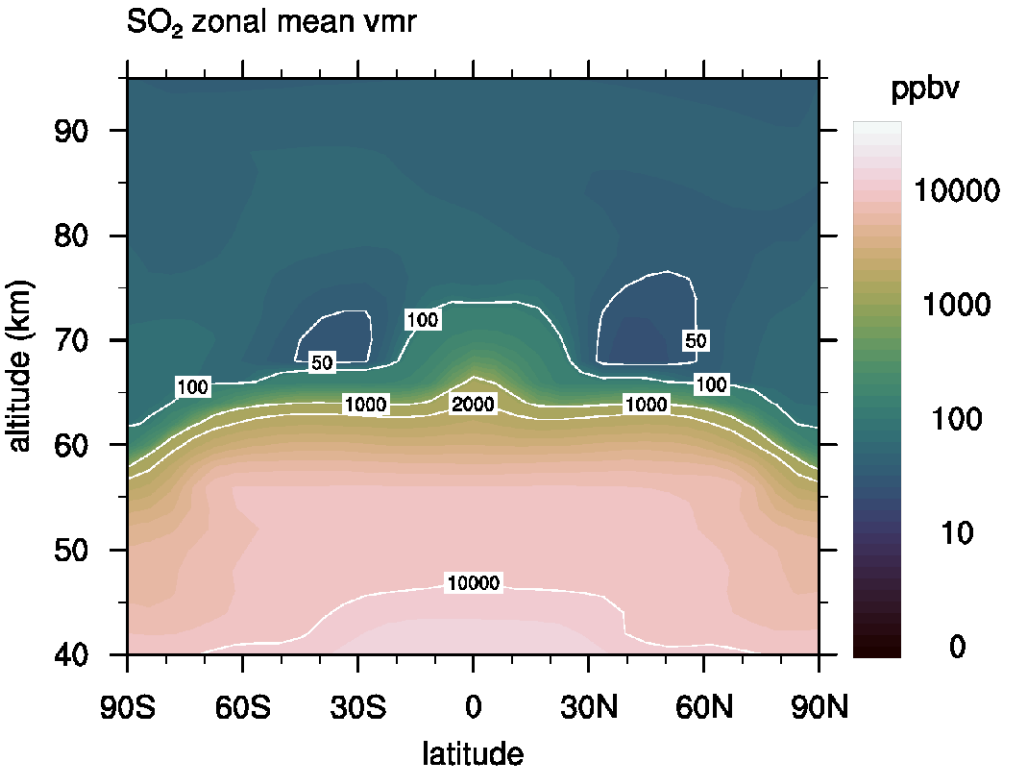

Figure 20: Sulfur dioxide zonally-averaged mixing ratio. Unit is ppbv

In the mesosphere, the distribution of SO_2 has been documented in recent years by the SOIR and SPICAV experiments onboard *Venus Express* (Belyaev et al., 2012; Mahieux et al., 2015a; Evdokimova et al., 2021), HST observations (Jessup et al., 2015) and JCMT ground-based measurements (Sandor et al., 2010). Around 80 km, the SOIR and HST data indicate SO_2 variable amounts of 40-100 ppbv. From 85 km upwards, a noticeable feature of the SPICAV data is the apparent increase in SO_2 with altitude (Belyaev et al., 2012), which is qualitatively consistent with the profile cut-off at 85 km derived from JCMT (Sandor et al., 2010), although the SPICAV abundances are significantly larger. These observations suggest the presence of a yet unidentified supply of sulfur at high altitudes. However, this hypothesis is tempered by the recent reprocessing of SPICAV nighttime data, which concludes to a roughly constant SO_2 mixing ratio of 135±21 ppbv between 84-102 km (Evdokimova et al., 2021). The SO_2 profile calculated by the Venus PCM is uniform above 75 km with a mixing ratio close to 100 ppbv, in rather good agreement with the SPICAV observations.

3.6.2. Sulfur monoxide SO

Sulfur monoxide is the primary product of SO_2 photolysis. Once produced, SO reacts rapidly with O (reaction R74) or ClO (reaction R79) to reform SO_2. Thus, in the Venus PCM, SO has a rather short lifetime of about 30 minutes above the clouds. It is in permanent photochemical equilibrium with SO_2 and follows its evolution during the day. At night, due to the absence of significant production, SO is entirely converted into SO_2. This explains the strong diurnal variation of SO calculated by the model above the clouds in Atlas A. Fig. 21 plots the daytime vertical distribution of SO calculated by the Venus PCM. SO shows a general increase with altitude and reaches an average value of about 25 ppbv at the model top at 95 km. Thus, at all altitudes, SO represents a minor fraction of the SO_x (SO + SO_2) family. During the day, the ratio $[SO_2]/[SO]$ calculated by the model decreases with altitude from a value of ~6 at 87 km to 3.6 at 95 km. These values are in the upper range of the SPICAV measurements, which indicate ratios of 5 ± 1 at 87 km and 2 ± 1 at 95 km (Belyaev et al., 2012). The $[SO_2]/[SO]$ ratios calculated by the Venus PCM are also in the high range of the values determined from sub-mm measurements by Sandor et al. (2010), who observed ratios between 0.6 and 3.8 averaged above 85 km.

3.6.3. Carbonyl sulfide OCS

In our simulations, the mixing ratio of OCS is initialized to 3 ppmv near the surface. This value is representative of the averaged mixing ratio reported at 33 km from VIRTIS-H spectra (Marcq et al., 2008). However, ground-based observations suggest that OCS decreases with altitude by almost two orders of magnitude between 30 and 40 km (Marcq et al., 2006; Bézard and de Bergh, 2007; Arney et al., 2014). This strong vertical gradient is notoriously difficult to reproduce by chemical models, in the absence of sufficient laboratory data regarding the chemistry of OCS in the conditions of the lower atmosphere of Venus (see the review by Marcq et al. (2018)). In our case, in the deep atmosphere, the Venus PCM only shows a moderate decrease of OCS with altitude up to the cloud base (Fig. 21). At 40 km, the OCS mixing ratio calculated by the model is larger than the observed 0.3-0.6 ppmv by at least a factor of four. This shortcoming is not surprising since the conventional chemistry implemented in the present version of the model does not include reactions playing a significant role in the OCS chemistry below the clouds.

Above the cloud tops, day side measurements with the IRTF/CSHELL allowed Krasnopolsky (2010b) to detect OCS near 65 km. The observed OCS mixing ratio at 65 km varies from 0.3 to 9 ppbv with a mean value of 3 ppbv. With a mean OCS mixing ratio of about 1 ppbv at 65 km, the Venus PCM is at the lower end of the observed values, but reproduces relatively well the two-order-of-magnitude decrease in OCS between the bottom and the top of the Venus clouds. This is an indication of a realistic treatment of the OCS photolysis in the model and, more generally, of the gradual extinction of the ultraviolet flux through the cloud layers.

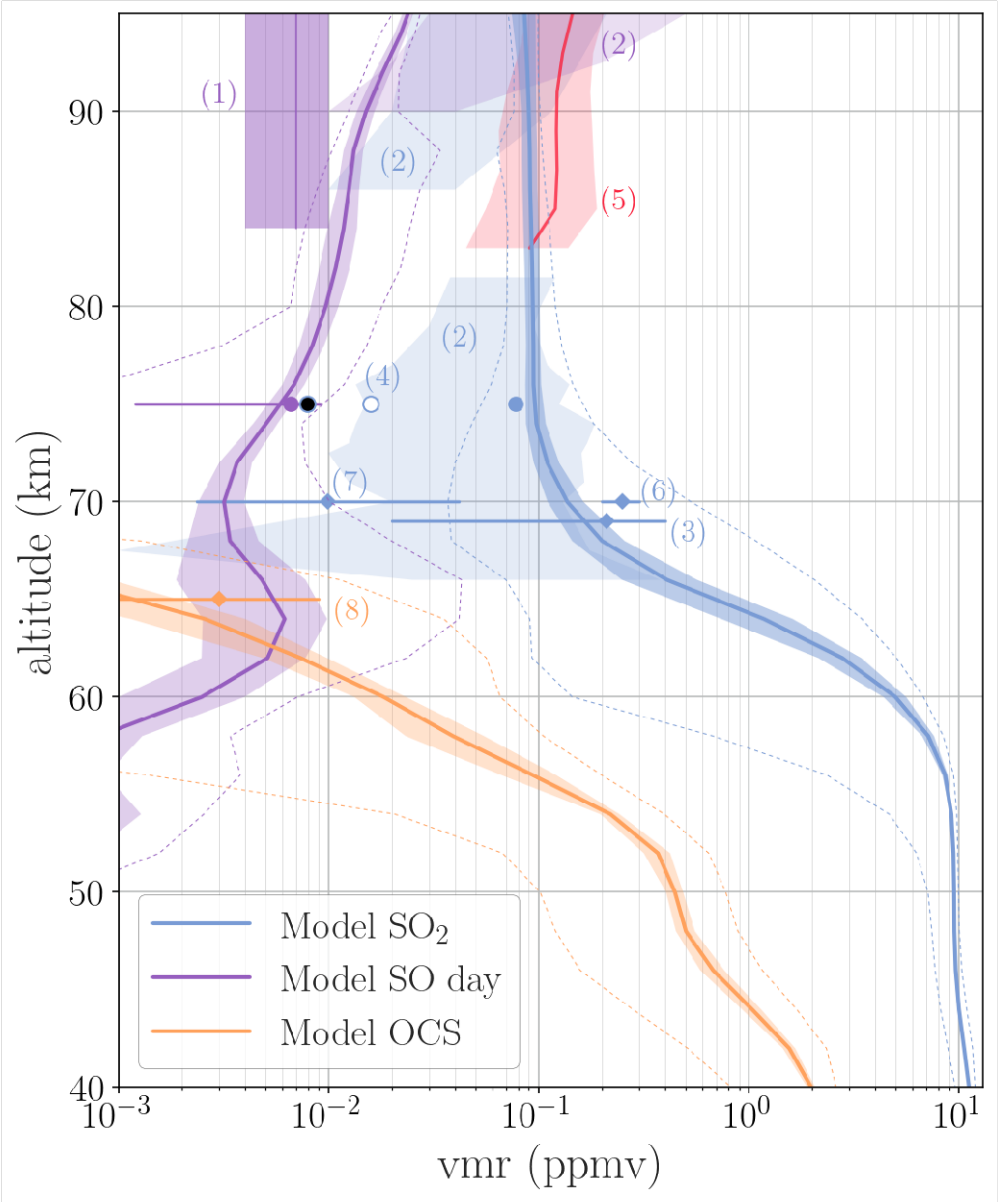

Figure 21: Modeled and observed vertical profiles of SO_2, SO, and OCS. Blue curve: Venus PCM SO_2 global average. Purple curve: Venus PCM SO averaged on the dayside. Orange curve: Venus PCM OCS global average. The colored envelopes correspond to the standard deviation in latitude and local time. The dotted lines represent the minimum and maximum values. Sulfur species measurements: (1) Purple: SO from JCMT, disk-averaged (Sandor et al., 2010). (2) Light blue: SO_2 at the terminators from SOIR, 68-82 km (Mahieux et al., 2015a; Belyaev et al., 2012) and from SPICAV, 85-95 km (Belyaev et al., 2012). Purple: SO at the terminators from SPICAV (Belyaev et al., 2012). (3) SO_2 from Pioneer Venus, Venera 15, HST and rocket data (Esposito et al., 1997).(4) SO_2 and SO from Hubble Space Telescope, dayside (Jessup et al., 2015). SO_2: Black circle: 27/01/2011. White circle: 22/01/2011. Blue circle: 28/12/2010. SO: Purple circle (5) SO_2 from SPICAV, nightside (Evdokimova et al., 2021). (6) SO_2 from TEXES (Encrenaz et al., 2020). (7) SO_2 from SPICAV nadir, dayside (Marcq et al., 2020).(8) OCS from IRTF/CSHELL (Krasnopolsky, 2010c).

3.6.4. Sulfuric acid $H_2SO_{4(g)}$

In the current state of knowledge, the formation of sulfuric acid, and its subsequent condensation, is the main identified sink for the large quantities of SO_2 transported upwards from the deep atmosphere. In the model, the amount of H_2SO_4 in the gaseous phase is calculated explicitly and is in permanent equilibrium with its condensed phase. The production of H_2SO_4 via reaction R78 depends on the availability of SO_3 and H_2O, whereas its condensation is

driven by its vapor pressure profile, i.e. by the temperature profile calculated by the Venus PCM. In our simulations, H_2SO_4 is almost completely condensed from the base of the cloud to the top of the atmosphere. This results in gas-phase amounts of only a few pptv above the clouds (Atlas B), which are thus largely below the upper limit of 3 ppbv determined from the sub-mm measurements of Sandor et al. (2012). Below the clouds, the modeled H_2SO_4 is present in appreciable quantities only in a layer between 35 and 45 km altitude (see Fig. 10b and Fig. 22). This vertical distribution is qualitatively similar to the radio frequency observations with the Very Large Array by Jenkins et al. (2002) and with VeRa onboard *Venus Express* by Oschlisniok et al. (2012, 2021). The latitudinal distribution of gas-phase H_2SO_4 calculated by the Venus PCM is also similar to the measurements of Oschlisniok et al. (2021) with two maxima located around 60° in each hemisphere. However, the quantitative agreement with the observations is less satisfactory. Below the clouds, Oschlisniok et al. (2021) indeed found variable H_2SO_4 amounts of 4 to 12 ppmv in the 43-47 km layer km, whereas the largest values in the Venus PCM reach only 2.5 ppmv at 42 km. These too low amounts result directly from the cold bias of about 20 K in the Venus PCM mentioned in Section 3.1.2, displacing the H_2SO_4 equilibrium towards the liquid phase. Nonetheless, our modelling of H_2SO_4 is in rather agreement with the model of Krasnopolsky (2013), which calculated 3.5 ppmv at the lower cloud base against roughly 2.5 ppmv in the Venus PCM (the cloud base is at 47 km in Krasnopolsky (2013) and ≈ 42 km in the Venus PCM).

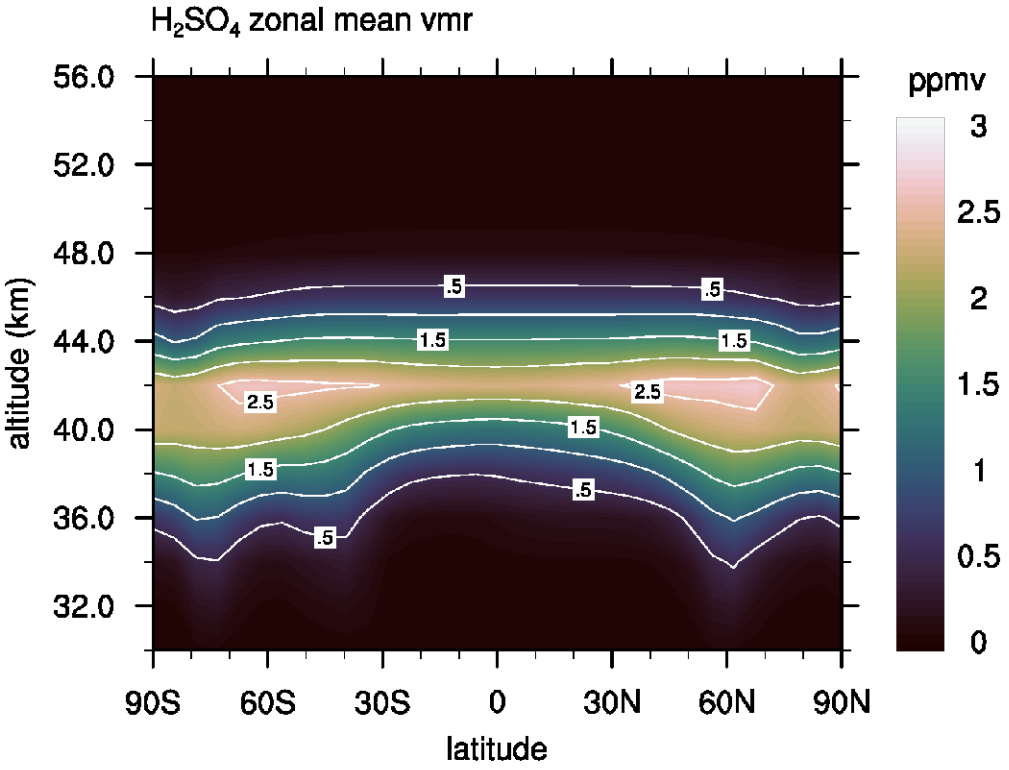

Figure 22: Sulfuric acid zonally-averaged mixing ratio. Unit is ppmv

4. Conclusion

We have presented the first three-dimensional simulations of the coupled photochemistry-cloud system in the atmosphere of Venus. The Venus PCM described here extends from the ground to the bottom of the thermosphere. It includes a comprehensive photochemical model and an equilibrium cloud model allowing continuous tracking of the H_2SO_4-H_2O condensed phase. Concerning the clouds, our results suggest that the largest particles (the so-called mode 3) observed by Knollenberg and Hunten (1980) are most likely not fully liquid. If one assumes that those particles contain a solid core, the sedimentation mass flux combined with the effect of vertical transport provide a profile of droplet number density consistent with the available observations. Regarding the photochemistry, the

Venus PCM simulations indicate that the distribution of long-lived species, such as CO or O_2, is mainly driven by the planetary Hadley cell circulation. On a given altitude level, enhanced mixing ratios are predicted at high latitudes due to the downwelling motion above the poles. The fact that the three-dimensional distribution of CO is in rather good quantitative agreement with the observations is indicative that the chlorine-catalyzed loss of CO is reasonably well reproduced by the model but a more robust confirmation will require long-term simulations. On the other hand, the Venus PCM calculates mixing ratios of ground-state O_2 that are far superior to the upper limit of 3 ppmv derived by Mills (1999). This issue is common to all photochemical models and remains unanswered at the present time (see Marcq et al., 2018, for a review). The main source of chlorine, HCl, has a modelled vertical distribution in agreement with ground-based observations but not with the Venus Express/SOIR data. Further work is therefore needed to first reconcile the difference among the observations and offer a robust reference for photochemical models. The water vapor vertical profile is well reproduced by the model and the condensation barrier combined with the production of H_2SO_4 is able to block 90% of the water vapor in the cloud deck. Regarding H_2SO_4, the Venus PCM simulations show that this species cannot be solely responsible for the observed SO_2 decrease of three orders of magnitude from below to above the clouds. In our simulations, the condensation of the binary $H_2SO_4 - H_2O$ droplets can only account for roughly 10% of the observed SO_2 mass below the clouds. Thus, the depletion of SO_2 cannot be explained by known chemistry and new chemical or physical paths must be explored. Recently, Rimmer et al. (2021) proposed that the presence of hydroxide salts in the cloud droplets could efficiently promote the dissolution of SO_2. This hypothesis may provide a viable solution but will probably require in-situ measurements of the droplet composition to be confirmed.

In the mean time, the implementation of the liquid-phase chemistry in the Venus PCM is one identified avenue of progress in the next years, as is the addition of polysulfur species (S_3 to S_8), which could also contribute to hold large amounts of sulfur below or within the clouds. Using the Venus PCM version extended to the thermosphere (Gilli et al., 2021), another planned improvement is the introduction of the nitrogen chemistry. This will allow to study the NO nightglow observed near 115 km (e.g., Stiepen et al. (2012, 2013)) and constrain the dynamics on the night side of Venus. Finally, we plan to couple to the Venus PCM the detailed microphysical model MAD-VenLA (Guilbon, 2018; Määttänen et al., 2022), which will allow to go one step further in the description of the life cycle of the droplets forming the clouds and their impact on the composition of the atmosphere of Venus.

5. Acknowledgments

We thank Slimane Bekki (LATMOS) and Olivier Boucher (LMD) for their contribution to the cloud model and their help on the evaluation of the sedimentation flux, first applied in Stolzenbach (2016). We thank Antoine Martinez (LATMOS) who provided the latitude interpolated VIRA vertical profiles and Kevin Mc Gouldrick (LASP) for the discussion about the mass loading. Finally, we want to thank the anonymous reviewer and Vladimir A. Krasnopolsky for their comments and helpful remarks during the review process.

References

Arney, G., Meadows, V., Crisp, D., Schmidt, S.J., Bailey, J., Robinson, T., 2014. Spatially resolved measurements of H_2O, HCl, CO, OCS, SO_2, cloud opacity, and acid concentration in the venus near-infrared spectral windows. Journal of Geophysical Research: Planets 119, 1860–1891.

Atkinson, R., Baulch, D., Cox, R., Crowley, J., Hampson, R., Hynes, R., Jenkin, M., Rossi, M., Troe, J., 2004. Evaluated kinetic and photochemical data for atmospheric chemistry: volume i-gas phase reactions of O_x, HO_x, NO_x and SO_x species. Atmospheric chemistry and physics 4, 1461–1738.

Ayers, G.P., Gillett, R.W., Gras, J.L., 1980. On the vapor pressure of sulfuric acid. Geophys. Res. Lett. 7, 433–436.

Barstow, J., Tsang, C., Wilson, C., Irwin, P., Taylor, F., McGouldrick, K., Drossart, P., Piccioni, G., Tellmann, S., 2012. Models of the global cloud structure on Venus derived from Venus Express observations. Icarus 217, 542–560.

Baulch, D., Bowman, C., Cobos, C., Cox, R., Just, T., Kerr, J., Pilling, M., Stocker, D., Troe, J., Tsang, W., et al., 2005. Evaluated kinetic data for combustion modeling: supplement ii. Journal of physical and chemical reference data 34, 757–1397.

Baulch, D., Cox, R., Hampson Jr, R., Kerr, J.A., Troe, J., Watson, R., 1980. Evaluated kinetic and photochemical data for atmospheric chemistry. Journal of Physical and Chemical Reference Data 9, 294–472.

Belyaev, D., Montmessin, F., Bertaux, J.L., Mahieux, A., Fedorova, A.A., Korablev, O.I., Marcq, E., Yung, Y.L., Zhang, X., 2012. Vertical profiling of SO_2 and SO above Venus clouds by SPICAV/SOIR solar occultations. Icarus 217, 740–751.

Bézard, B., de Bergh, C., 2007. Composition of the atmosphere of Venus below the clouds. Journal of Geophysical Research: Planets 112.

Bézard, B., de Bergh, C., Fegley, B., Maillard, J.P., Crisp, D., Owen, T., Pollack, J.B., Grinspoon, D., 1993. The abundance of sulfur dioxide below the clouds of Venus. Geophysical Research Letters 20, 1587–1590.

Bierson, C.J., Zhang, X., 2020. Chemical cycling in the venusian atmosphere: A full photochemical model from the surface to 110 km. Journal of Geophysical Research: Planets 125, e2019JE006159. doi:10.1029/2019JE006159.

Burkholder, J., Sander, S., Abbatt, J., Barker, J., Huie, R., Kolb, C., Kurylo, M., Orkin, V., Wilmouth, D., Wine, P., 2015. Chemical kinetics and photochemical data for use in atmospheric studies: evaluation number 18.

Burkholder, J.B., McKeen, S., 1997. UV absorption cross sections for SO_3. Geophysical research letters 24, 3201–3204.

Campbell, I., Gray, C., 1973. Rate constants for $O(^3P)$ recombination and association with $N(^4S)$. Chemical Physics Letters 18, 607–609.

Cariolle, D., Moinat, P., Teyssèdre, H., Giraud, L., Josse, B., Lefèvre, F., 2017. Asis v1.0: an adaptative solver for the simulation of atmospheric chemistry. Geoscientific Model Development Discussions 10, 1467–1485.

Chamberlain, S., Mahieux, A., Robert, S., Piccialli, A., Trompet, L., Vandaele, A.C., Wilquet, V., 2020. SOIR/VEx observations of water vapor at the terminator in the venus mesosphere. Icarus 346, 113819.

Chan, W., Cooper, G., Brion, C., 1993. The electronic spectrum of carbon dioxide. discrete and continuum photoabsorption oscillator strengths (6-203 ev). Chemical Physics 178, 401–413.

Cheng, B.M., Chew, E.P., Liu, C.P., Bahou, M., Lee, Y.P., Yung, Y.L., Gerstell, M.F., 1999. Photo-induced fractionation of water isotopomers in the martian atmosphere. Geophysical Research Letters 26, 3657–3660.

Christensen, L.E., Okumura, M., Sander, S.P., Salawitch, R.J., Toon, G.C., Sen, B., Blavier, J.F., Jucks, K.W., 2002. Kinetics of $HO_2 + HO_2 = H_2O_2 + O_2$: implications for stratospheric H_2O_2. Geophysical Research Letters 29, 13–1–13–4.

Chung, K., Calvert, J.G., Bottenheim, J.W., 1975. The photochemistry of sulfur dioxide excited within its first allowed band (3130 Å) and the "forbidden" band (3700–; 4000 Å). International Journal of Chemical Kinetics 7, 161–182.

Cimino, J., 1982. The composition and vertical structure of the lower cloud deck on Venus. Icarus 51, 334–357.

Clancy, R.T., Muhleman, D.O., 1985. Chemical-dynamical models of the Venus mesosphere based upon diurnal microwave CO variations. Icarus 64, 183–204.

Clancy, R.T., Sandor, B.J., Moriarty-Schieven, G., 2012. Thermal structure and CO distribution for the venus mesosphere/lower thermosphere: 2001 - 2009 inferior conjunction sub-millimeter CO absorption line observations. Icarus 217, 779–793.

Connes, P., Connes, J., Benedict, W., Kaplan, L., 1967. Traces of HCl and HF in the atmosphere of Venus. The Astrophysical Journal 147, 1230–1237.

Connes, P., Connes, J., Kaplan, L., Benedict, W., 1968. Carbon monoxide in the Venus atmosphere. The Astrophysical Journal 152, 731–743.

Cottini, V., Ignatiev, N., Piccioni, G., Drossart, P., 2015. Water vapor near venus cloud tops from VIRTIS-H/Venus Express observations 2006-2011. Planetary and Space Science 113–114, 219–225.

Cottini, V., Ignatiev, N., Piccioni, G., Drossart, P., Grassi, D., Markiewicz, W., 2012. Water vapor near the cloud tops of venus from Venus Express/VIRTIS dayside data. Icarus 217, 561–569.

Cotton, D.V., Bailey, J., Crisp, D., Meadows, V., 2012. The distribution of carbon monoxide in the lower atmosphere of Venus. Icarus 217, 570–584.

Crisp, D., 1986. Radiative forcing of the Venus mesosphere: I. solar fluxes and heating rates. Icarus 67, 484–514.

Crisp, D., Allen, D., Grinspoon, D., Pollack, J., 1991. The dark side of Venus: near-infrared images and spectra from the Anglo-Australian Observatory. Science 253, 1263–1266.

Drossart, P., Bézard, B., Encrenaz, T., Lellouch, E., Roos, M., Taylor, F., Collard, A., Calcutt, S., Pollack, J., Grinspoon, D., et al., 1993. Search for spatial variations of the H_2O abundance in the lower atmosphere of Venus from NIMS-GALILEO. Planetary and space science 41, 495–504.

Encrenaz, T., Greathouse, T.K., Marcq, E., Sagawa, H., Widemann, T., Bézard, B., Fouchet, T., Lefèvre, F., Lebonnois, S., Atreya, S.K., Lee, Y.J., Giles, R., Watanabe, S., Shao, W., Zhang, X., Bierson, C.J., 2020. HDO and SO_2 thermal mapping on Venus - V. Evidence for a long-term anti-correlation. Astronomy & Astrophysics 639, A69.

Encrenaz, T., Greathouse, T.K., Richter, M., DeWitt, C., Lacy, J., Widemann, T., Bezard, B., Fouchet, T., Atreya, S., Sagawa, H., 2015. Variability of SO_2 and HDO at the cloudtop of Venus from high-resolution infrared spectroscopy, in: European Planetary Science Congress, pp. EPSC2015–113.

Esposito, L., Bertaux, J., Krasnopolsky, V., Moroz, V., Zasova, L., 1997. Chemistry of lower atmosphere and clouds.. University of Arizona Press. p. 415.

Evdokimova, D., Belyaev, D., Montmessin, F., Korablev, O., Bertaux, J.L., Verdier, L., Lefèvre, F., Marcq, E., 2021. The spatial and temporal distribution of nighttime ozone and sulfur dioxide in the Venus mesosphere as deduced from SPICAV UV stellar occultations. Journal of Geophysical Research: Planets , e2020JE006625.

Eymet, V., Fournier, R., Dufresne, J.L., Lebonnois, S., Hourdin, F., Bullock, M.A., 2009. Net exchange parameterization of thermal infrared radiative transfer in Venus' atmosphere. Journal of Geophysical Research: Planets 114.

Fedorova, A., Korablev, O., Vandaele, A.C., Bertaux, J.L., Belyaev, D., Mahieux, A., Neefs, E., Wilquet, W.V., Drummond, R., Montmessin, F., Villard, E., 2008. HDO and H_2O vertical distributions and isotopic ratio in the venus mesosphere by solar occultation at infrared spectrometer on board venus express. Journal of Geophysical Research: Planets 113.

Fedorova, A., Marcq, E., Luginin, M., Korablev, O., Bertaux, J.L., Montmessin, F., 2016. Variations of water vapor and cloud top altitude in the venus' mesosphere from SPICAV/VEx observations. Icarus 275, 143–162.

Fink, U., Larson, H.P., Kuiper, G.P., Poppen, R.F., 1972. Water vapor in the atmosphere of Venus. Icarus 17, 617–631.

Garate-Lopez, I., Lebonnois, S., 2018. Latitudinal variation of clouds' structure responsible for Venus cold collar. Icarus 314, 1–11.

Giauque, W., Hornung, E., Kunzler, J., Rubin, T., 1960. The thermodynamic properties of aqueous sulfuric acid solutions and hydrates from 15 to 300K. J. Am. Chern. SOC 82, 62–70.

Gibson, S., Gies, H., Blake, A., McCoy, D., Rogers, P., 1983. Temperature dependence in the Schumann-Runge photoabsorption continuum of oxygen. Journal of Quantitative Spectroscopy and Radiative Transfer 30, 385–393.

Gierasch, P., Goody, R., Young, R., Crisp, D., Edwards, C., Kahn, R., Rider, D., Del Genio, A., Greeley, R., Hou, A., et al., 1997. The general circulation of the Venus atmosphere: An assessment. University of Arizona Press. pp. 459–500.

Gilli, G., Lebonnois, S., Gonzalez-Galindo, F., Lopez-Valverde, M.A., Stolzenbach, A., Lefèvre, F., Chaufray, J.L., Lott, F., 2017. Thermal structure of the upper atmosphere of Venus simulated by a ground-to-thermosphere GCM. Icarus 281, 55–72.

Gilli, G., Navarro, T., Lebonnois, S., Quirino, D., Silva, V., Stolzenbach, A., Lefèvre, F., Schubert, G., 2021. Venus upper atmosphere revealed by a GCM: II. Model validation with temperature and density measurements. Icarus 366, 114432. doi:10.1016/j.icarus.2021.114432.

Gmitro, J., Vermeulen, T., 1964. Vapor-liquid equilibria for aqueous sulfuric acid. A.I.Ch.E. Journal 10, 740–746.

Guilbon, S., 2018. Développement d'un modèle microphysique de nuages pour un modèle de climat global vénusien. Ph.D. thesis. Université de Versailles Saint-Quentin-en-Yvelines.

Gurwell, M.A., Melnick, G.J., Tolls, V., Bergin, E.A., Patten, B.M., 2007. Swas observations of water vapor in the Venus mesosphere. Icarus 188, 288–304.

Hermans, C., Vandaele, A., Fally, S., 2009. Fourier transform measurements of SO_2 absorption cross sections:: I. temperature dependence in the 24 000-29 000 cm^{-1} (345-420 nm) region. Journal of Quantitative Spectroscopy and Radiative Transfer 110, 756–765.

Herron, J.T., Huie, R.E., 1980. Rate constants at 298 k for the reactions SO + SO + M $\rightarrow$ S_2O_2+ m and SO+ S_2O_2 $\rightarrow$ SO_2 + S_2O. Chemical Physics Letters 76, 322–324.

Hintze, P.E., Kjaergaard, H.G., Vaida, V., , Burkholder, J.B., 2003. Vibrational and electronic spectroscopy of sulfuric acid vapor. The Journal of Physical Chemistry A 107, 1112–1118.

Hoffmann, W., Seeman, F.W., 1960. Schwefelsäure-wasser gemischen im temperaturbereich von 15 bis 25°C. Z. Physik. Chem. Neue Folge 24, 300–306.

Hourdin, F., Musat, I., Bony, S., Braconnot, P., Codron, F., Dufresne, J.L., Fairhead, L., Filiberti, M.A., Friedlingstein, P., Grandpeix, J.Y., Krinner, G., LeVan, P., Li, Z.X., Lott, F., 2006. The LMDZ4 general circulation model: climate performance and sensitivity to parametrized physics with emphasis on tropical convection. volume 27.

Ignatiev, N., Moroz, V., Zasova, L., Khatuntsev, I., 1999. Venera 15: Water vapour in the middle atmosphere of venus. Advances in Space Research 23, 1549–1558.

Imamura, T., Hashimoto, G., 2002. H_2SO_4 cycle in the venusian tropical atmosphere as constrained by a microphysical cloud model. Advances in Space Research 29, 249–254.

Irwin, P.G.J., de Kok, R., Negrão, A., Tsang, C.C.C., Wilson, C.F., Drossart, P., Piccioni, G., Grassi, D., Taylor, F.W., 2008. Spatial variability of carbon monoxide in Venus' mesosphere from Venus Express/visible and infrared thermal imaging spectrometer measurements. Journal of Geophysical Research: Planets 113.

Iwagami, N., Ohtsuki, S., Tokuda, K., Ohira, N., Kasaba, Y., Imamura, T., Sagawa, H., Hashimoto, G., Takeuchi, S., Ueno, M., Okumura, S., 2008. Hemispheric distributions of HCl above and below the venus clouds by ground-based 1.7 μm spectroscopy. Planetary and Space Science 56, 1424–1434.

Jacob, A., Winkler, C., 1972. Kinetics of the reactions of oxygen atoms and nitrogen atoms with sulphur trioxide. Journal of the Chemical Society, Faraday Transactions 1: Physical Chemistry in Condensed Phases 68, 2077–2082.

James, E., Toon, O., Schubert, G., 1997. A numerical microphysical model of the condensational Venus cloud. Icarus 129, 147–171.

Jenkins, J.M., Kolodner, M.A., Butler, B.J., Suleiman, S.H., Steffes, P.G., 2002. Microwave remote sensing of the temperature and distribution of sulfur compounds in the lower atmosphere of Venus. Icarus 158, 312–328.

Jessup, K.L., Marcq, E., Mills, F., Mahieux, A., Limaye, S., Wilson, C., Allen, M., Bertaux, J.L., Markiewicz, W., Roman, T., Vandaele, A.C., Wilquet, V., Yung, Y., 2015. Coordinated Hubble Space Telescope and Venus Express Observations of Venus' upper cloud deck. Icarus 258, 309–336.

Jones, J., 1924. On the determination of molecular fields. I. from the variation of the viscosity of a gas with temperature. Proceedings of the Royal Society of London A: Mathematical, Physical and Engineering Sciences 106, 441–462.

Joshi, A.V., Wang, H., 2006. Master equation modeling of wide range temperature and pressure dependence of CO + OH = products. International journal of chemical kinetics 38, 57–73.

Khatuntsev, I., Patsaeva, M., Titov, D., Ignatiev, N., Turin, A., Fedorova, A., Markiewicz, W.J., 2017. Winds in the middle cloud deck from the near-IR imaging by the Venus Monitoring Camera onboard Venus Express. Journal of Geophysical Research: Planets 122, 2312–2327.

Khatuntsev, I., Patsaeva, M., Titov, D., Ignatiev, N., Turin, A., Limaye, S., Markiewicz, W., Almeida, M., Roatsch, T., Moissl, R., 2013. Cloud level winds from the Venus Express Monitoring Camera imaging. Icarus 226, 140–158.

Knollenberg, R., Hunten, D., 1980. The microphysics of the clouds of Venus: results of the pioneer venus particle size spectrometer experiment. J. Geophys. Res. 88, 8039–8058.

Knollenberg, R.G., 1984. A reexamination of the evidence for large, solid particles in the clouds of Venus. Icarus 57, 161–183.

Krasnopolsky, V.A., 2006. A sensitive search for nitric oxide in the lower atmospheres of Venus and mars: Detection on Venus and upper limit for mars. Icarus 182, 80–91.

Krasnopolsky, V.A., 2007. Chemical kinetic model for the lower atmosphere of Venus. Icarus 191, 25–37.

Krasnopolsky, V.A., 2010a. Spatially-resolved high-resolution spectroscopy of Venus 1. variations of CO_2, CO, HF, and HCl at the cloud tops. Icarus 208, 539–547.

Krasnopolsky, V.A., 2010b. Spatially-resolved high-resolution spectroscopy of Venus 2. variations of HDO, OCS, and SO_2 at the cloud tops. Icarus 209, 314–322.

Krasnopolsky, V.A., 2010c. Venus night airglow: ground-based detection of OH, observations of O_2 emissions, and photochemical model. Icarus 207, 17–27.

Krasnopolsky, V.A., 2012a. Observation of DCl and upper limit to NH_3 on Venus. Icarus 219, 244–249.

Krasnopolsky, V.A., 2012b. A photochemical model for the Venus atmosphere at 47-112km. Icarus 218, 230–246.

Krasnopolsky, V.A., 2013. S_3 and S_4 abundances and improved chemical kinetic model for the lower atmosphere of Venus. Icarus 225, 570–580.

Krasnopolsky, V.A., 2015. Vertical profiles of H_2O, H_2SO_4, and sulfuric acid concentration at 45-75 km on venus. Icarus 252, 327–333.

Krasnopolsky, V.A., 2018. Disulfur dioxide and its near-UV absorption in the photochemical model of Venus atmosphere. Icarus 299, 294–299.

Krasnopolsky, V.A., Belyaev, D., Gordon, I., Li, G., Rothman, L., 2013. Observations of D/H ratios in H_2O, HCl, and HF on Venus and new DCl and DF line strengths. Icarus 224, 57–65.

Kulmala, M., Laaksonen, A., 1990. Binary nucleation of water-sulfuric acid system: Comparison of classical theories with different H_2SO_4 saturation vapor pressures. J. Chem. Phys. 93, 696–701.

Lafferty, W.J., Solodov, A.M., Lugez, C.L., Fraser, G.T., 1998. Rotational line strengths and self-pressure-broadening coefficients for the 1.27-μm, $a^1\Delta_g - \chi^3\Sigma g^-$, v= 0–0 band of O_2. Applied optics 37, 2264–2270.

Lebonnois, S., Hourdin, F., Eymet, V., Crespin, A., Fournier, R., Forget, F., 2010. Superrotation of Venus' atmosphere analyzed with a full general circulation model. J. Geophys. Res. 115.

Lebonnois, S., Sugimoto, N., Gilli, G., 2016. Wave analysis in the atmosphere of Venus below 100-km altitude, simulated by the LMD Venus GCM. Icarus 278, 38–51.

Lefèvre, F., Lebonnois, S., Montmessin, F., Forget, F., 2004. Three-dimensional modeling of ozone on Mars. Journal of Geophysical Research: Planets 109.

Lellouch, E., Goldstein, J.J., Rosenqvist, J., Bougher, S.W., Paubert, G., 1994. Global circulation, thermal structure, and carbon monoxide distribution in Venus' mesosphere in 1991. Icarus 110, 315–339.

Lewis, B., Vardavas, I., Carver, J., 1983. The aeronomic dissociation of water vapor by solar H Lyman α radiation. Journal of Geophysical Research: Space Physics 88, 4935–4940.

Limaye, S.S., 2007. Venus atmospheric circulation: Known and unknown. Journal of Geophysical Research: Planets 112.

Lovejoy, E.R., Hanson, D.R., Huey, L.G., 1996. Kinetics and products of the gas-phase reaction of SO_3 with water. The Journal of Physical Chemistry 100, 19911–19916.

Lu, C.W., Wu, Y.J., Lee, Y.P., Zhu, R.S., Lin, M.C., 2006. Experimental and theoretical investigation of rate coefficients of the reaction S(p3) + OCS in the temperature range of 298-985K. The Journal of Chemical Physics 125, 164329.

Määttänen, A., Guilbon, S., Burgalat, J., Montmessin, F., 2022. Development of a new cloud model for Venus (MAD-VenLA) using the Modal Aerosol Dynamics approach. Advances in Space Research .

Madronich, S., Flocke, S., 1999. The role of solar radiation in atmospheric chemistry, in: Boule, P. (Ed.), Environmental Photochemistry. Springer. The Handbook of Environmental Chemistry, pp. 1–26.

Mahieux, A., Vandaele, A., Robert, S., Wilquet, V., Drummond, R., Chamberlain, S., Belyaev, D., Bertaux, J., 2015a. Venus mesospheric sulfur dioxide measurement retrieved from SOIR on board Venus Express. Planetary and Space Science 113, 193–204.

Mahieux, A., Wilquet, V., Vandaele, A., Robert, S., Drummond, R., Chamberlain, S., Ribes, A.G., Bertaux, J., 2015b. Hydrogen halides measurements in the Venus mesosphere retrieved from SOIR on board Venus Express. Planetary and Space Science 113–114, 264–274.

Marcq, E., Baggio, L., Lefèvre, F., Stolzenbach, A., Montmessin, F., Belyaev, D., Korablev, O., Bertaux, J.L., 2019. Discovery of cloud top ozone on Venus. Icarus 319, 491–498.

Marcq, E., Bézard, B., Drossart, P., Piccioni, G., Reess, J.M., Henry, F., 2008. A latitudinal survey of CO, OCS, H_2O, and SO_2 in the lower atmosphere of Venus: spectroscopic studies using VIRTIS-H. Journal of Geophysical Research: Planets 113.

Marcq, E., Encrenaz, T., Bezard, B., Birlan, M., 2006. Remote sensing of Venus lower atmosphere from ground-based IR spectroscopy: Latitudinal and vertical distribution of minor species. Planetary and Space Science 54, 1360–1370.

Marcq, E., Lea Jessup, K., Baggio, L., Encrenaz, T., Lee, Y.J., Montmessin, F., Belyaev, D., Korablev, O., Bertaux, J.L., 2020. Climatology of SO_2 and UV absorber at Venus' cloud top from SPICAV-UV nadir dataset. Icarus 335, 113368.

Marcq, E., Lellouch, E., Encrenaz, T., Widemann, T., Birlan, M., Bertaux, J.L., 2015. Search for horizontal and vertical variations of CO in the day and night side lower mesosphere of Venus from CSHELL/IRTF observations. Planetary and Space Science 113–114, 256–263.

Marcq, E., Mills, F.P., Parkinson, C.D., Vandaele, A.C., 2018. Composition and chemistry of the neutral atmosphere of Venus. Space Science Reviews 214, 10.

McElroy, M.B., Dak Sze, N., Ling Yung, Y., 1973. Photochemistry of the Venus atmosphere. Journal of the Atmospheric Sciences 30, 1437–1447.

McGouldrick, K., Toon, O.B., 2007. An investigation of possible causes of the holes in the condensational Venus cloud using a microphysical cloud model with a radiative-dynamical feedback. Icarus 191, 1–24.

Mills, F.P., 1998. I. Observations and photochemical modeling of the Venus middle atmosphere. II. Thermal infrared spectroscopy of Europa and Callisto. Ph.D. thesis.

Mills, F.P., 1999. A spectroscopic search for molecular oxygen in the Venus middle atmosphere. Journal of Geophysical Research: Planets 104, 30757–30763.

Mills, F.P., Allen, M., 2007. A review of selected issues concerning the chemistry in Venus middle atmosphere. Planetary and Space Science 55, 1729–1740.

Mills, F.P., Esposito, L.W., Yung, Y.L., 2013. Atmospheric Composition, Chemistry, and Clouds. American Geophysical Union (AGU). pp. 73–100.

Mills, M.J., Toon, O.B., Vaida, V., Hintze, P.E., Kjaergaard, H.G., Schofield, D.P., Robinson, T.W., 2005. Photolysis of sulfuric acid vapor by visible light as a source of the polar stratospheric CN layer. Journal of Geophysical Research: Atmospheres 110.

Minschwaner, K., Anderson, G., Hall, L., Yoshino, K., 1992. Polynomial coefficients for calculating O_2 Schumann-Runge cross sections at 0.5 cm^{-1} resolution. Journal of Geophysical Research: Atmospheres 97, 10103–10108.

Montmessin, F., Lefèvre, F., 2013. Transport-driven formation of a polar ozone layer on mars. Nature Geoscience 6, 930–933.

Morgan, L.J., Davies, C.E., 1916. The properties of mixed liquids i, sulfuric acid-water mixtures. J. Am. Chem. Soc. 38, 555–568.

Moses, J.I., Zolotov, M.Y., Fegley, B., 2002. Photochemistry of a volcanically driven atmosphere on Io: sulfur and oxygen species from a Pele-type eruption. Icarus 156, 76–106.

Myhre, C.E., Nielsen, C.J., Saastad, O.W., 1998. Density and surface tension of aqueous H_2SO_4 at low temperature. J. Chem. Eng. Data 43, 617–622.

Naidoo, J., Goumri, A., Marshall, P., 2005. A kinetic study of the reaction of atomic oxygen with SO_2. Proceedings of the Combustion Institute 30, 1219–1225.

National Research Council, 1928. International critical tables of numerical Data Physics, Chemistry and Technoloy. volume 1. McGraw-Hill, New-York.

Navarro, T., Gilli, G., Schubert, G., Lebonnois, S., Lefèvre, F., Quirino, D., 2021. Venus' upper atmosphere revealed by a GCM: I. Structure and variability of the circulation. Icarus 366, 114400.

Nicholas, J.E., Amodio, C.A., Baker, M.J., 1979. Kinetics and mechanism of the decomposition of H_2S, CH_3SH and $(CH_3)_2S$ in a radio-frequency

pulse discharge. Journal of the Chemical Society, Faraday Transactions 1: Physical Chemistry in Condensed Phases 79, 1868–1875.
Nicovich, J., Kreutter, K., Wine, P., 1990. Kinetics and thermochemistry of ClCO formation from the Cl^+ CO association reaction. The Journal of Chemical Physics 92, 3539–3544.
Ogawa, S., Ogawa, M., 1975. Absorption cross sections of O_2 ($a^1\Delta_g$) and O_2 ($x^3\Sigma_g^-$) in the region from 1087 to 1700 Å. Canadian Journal of Physics 53, 1845–1852.
Ohta, T., 1983. Mechanism of chlorine catalytic oxidation of CO in the gas phase. Bulletin of the Chemical Society of Japan 56, 869–872.
Oschlisniok, J., Häusler, B., Pätzold, M., Tellmann, S., Bird, M., Peter, K., Andert, T., 2021. Sulfuric acid vapor and sulfur dioxide in the atmosphere of Venus as observed by the Venus Express radio science experiment VeRa. Icarus 362, 114405.
Oschlisniok, J., Häusler, B., Pätzold, M., Tyler, G., Bird, M., Tellmann, S., Remus, S., Andert, T., 2012. Microwave absorptivity by sulfuric acid in the Venus atmosphere: First results from the Venus Express radio science experiment vera. Icarus 221, 940–948.
Parkinson, C.D., Gao, P., Esposito, L., Yung, Y., Bougher, S., Hirtzig, M., 2015. Photochemical control of the distribution of venusian water. Planetary and Space Science 113–114, 226–236.
Parkinson, W., Rufus, J., Yoshino, K., 2003. Absolute absorption cross section measurements of CO_2 in the wavelength region 163-200 nm and the temperature dependence. Chemical Physics 290, 251–256.
Peralta, J., Hueso, R., Sánchez-Lavega, A., 2007. A reanalysis of venus winds at two cloud levels from galileo SSI images. Icarus 90, 469–477.
Phillips, L.F., 1981. Absolute absorption cross sections for SO between 190 and 235 nm. The Journal of Physical Chemistry 85, 3994–4000.
Pollack, J.B., Dalton, J., Grinspoon, D., Wattson, R.B., Freedman, R., Crisp, D., Allen, D.A., Bezard, B., DeBergh, C., Giver, L.P., Ma, Q., Tipping, R., 1993. Near-infrared light from Venus' nightside: A spectroscopic analysis. Icarus 103, 1–42.
Prinn, R.G., 1971. Photochemistry of HCl and other minor constituents in the atmosphere of Venus. Journal of the Atmospheric Sciences 28, 1058–1068.
Ragent, B., Esposito, L., Tomasko, M., Marov, M., Shari, V., Lebedev, V., 1985. Particulate matter in the Venus atmosphere. Advances in Space Research 5, 85–115.
Ridders, C., 1979. A new algorithm for computing a single root of a real continuous function. Circuits and Systems, IEEE Transactions on 26, 979–980.
Rimmer, P.B., Jordan, S., Constantinou, T., Woitke, P., Shorttle, O., Hobbs, R., Paschodimas, A., 2021. Hydroxide Salts in the Clouds of Venus: Their Effect on the Sulfur Cycle and Cloud Droplet pH. The Planetary Science Journal 2, 133. doi:10.3847/PSJ/ac0156.
Sabinina, L., Terpugow, L., 1935. Die oberflächenspannung des systems schwefelsure-wasser. Z. Phyzik. Chem. Abt. 173A, 237–241.
Sánchez-Lavega, A., Hueso, R., Piccioni, G., Drossart, P., Peralta, J., Pérez-Hoyos, S., Wilson, C.F., Taylor, F.W., Baines, K.H., Luz, D., Erard, S., Lebonnois, S., 2008. Variable winds on Venus mapped in three dimensions. Geophysical Research Letters 35.
Sander, S.P., Abbatt, J., Barker, J.R., Burkholder, J.B., Friedl, R.R., Golden, D.M., Huie, R.E., Kolb, C.E., Kurylo, M.J., Moortgat, G., Orkin, V.L., Wine, P.H., 2011. Chemical kinetics and photochemical data for use in atmospheric studies, evaluation no. 17.
Sander, S.P., Friedl, R., Golden, D., Kurylo, M., Moortgat, G., Keller-Rudek, H., Wine, P., Ravishankara, A., Kolb, C., Molina, M., et al., 2003. Chemical kinetics and photochemical data for use in atmospheric studies: evaluation number 14.
Sander, S.P., Friedl, R., Golden, D., Kurylo, M., Moortgat, G., Keller-Rudek, H., Wine, P., Ravishankara, A., Kolb, C., Molina, M., et al., 2006. Chemical kinetics and photochemical data for use in atmospheric studies: evaluation number 15.
Sandor, B.J., Clancy, R.T., 2005. Water vapor variations in the Venus mesosphere from microwave spectra. Icarus 177, 129–143.
Sandor, B.J., Clancy, R.T., 2012. Observations of HCl altitude dependence and temporal variation in the 70 - 100 km mesosphere of venus. Icarus 220, 618–626.
Sandor, B.J., Clancy, R.T., Moriarty-Schieven, G., 2012. Upper limits for H_2SO_4 in the mesosphere of Venus. Icarus 217, 839–844.
Sandor, B.J., Clancy, R.T., Moriarty-Schieven, G., Mills, F.P., 2010. Sulfur chemistry in the venus mesosphere from SO_2 and SO microwave spectra. Icarus 208, 49–60.
Sandor, B.J., Clancy, T.R., 2018. First measurements of ClO in the Venus atmosphere – Altitude dependence and temporal variation. Icarus 313, 15–24.
Schubert, G., 1983. General circulation and the dynamical state of the Venus atmosphere, in: Venus. University of Arizona Press, pp. 681–765.
Schürgers, M., Welge, K., 1968. Absorptionskoeffizient von H_2O_2 und N_2H_4 zwischen 1200 und 2000 Å. Zeitschrift für Naturforschung A 23, 1508–1510.
Seiff, A., Schofield, J., Kliore, A., Taylor, F., Limaye, S., Revercomb, H., Sromovsky, L., Kerzhanovich, V., Moroz, V., Marov, M., 1985. Models of the structure of the atmosphere of Venus from the surface to 100 kilometers altitude. Advances in Space Research 5, 3–58.
Shao, W.D., Zhang, X., Bierson, C.J., Encrenaz, T., 2020. Revisiting the Sulfur-Water Chemical System in the Middle Atmosphere of Venus. Journal of Geophysical Research: Planets 125, e2019JE006195. doi:10.1029/2019JE006195.
Shao, W.D., Zhang, X., Mendonça, J., Encrenaz, T., 2022. Local-time Dependence of Chemical Species in the Venusian Mesosphere. The Planetary Science Journal 3, 3. doi:10.3847/PSJ/ac3bd3.
Singleton, D., Cvetanović, R.J., 1988. Evaluated chemical kinetic data for the reactions of atomic oxygen O (3P) with sulfur containing compounds. Journal of physical and chemical reference data 17, 1377–1437.
Stamnes, K., Tsay, S.C., Wiscombe, W., Jayaweera, K., 1988. Numerically stable algorithm for discrete-ordinate-method radiative transfer in multiple scattering and emitting layered media. Appl. Opt. 27, 2502–2509.
Stark, G., Yoshino, K., Smith, P., Ito, K., 2007. Photoabsorption cross section measurements of CO_2 between 106.1 and 118.7 nm at 295 and 195 K. Journal of Quantitative Spectroscopy and Radiative Transfer 103, 67–73.
Stiepen, A., Gérard, J.C., Dumont, M., Cox, C., Bertaux, J.L., 2013. Venus nitric oxide nightglow mapping from SPICAV nadir observations. Icarus 226, 428–436. doi:10.1016/j.icarus.2013.05.031.
Stiepen, A., Soret, L., Gérard, J.C., Cox, C., Bertaux, J.L., 2012. The vertical distribution of the Venus NO nightglow: Limb profiles inversion and one-dimensional modeling. Icarus 220, 981–989. doi:10.1016/j.icarus.2012.06.029.
Stolzenbach, A., 2016. Étude de la photochimie de Vénus à l'aide d'un modèle de circulation général. Ph.D. thesis.
Thompson, B.A., Harteck, P., Reeves, R.R., 1963. Ultraviolet absorption coefficients of CO_2, CO, O_2, H_2O, N_2O, NH_3, NO, SO_2, and CH_4 between 1850 and 4000 Å. Journal of Geophysical Research 68, 6431–6436.

Thuillier, G., Floyd, L., Woods, T., Cebula, R., Hilsenrath, E., Hersé, M., Labs, D., 2004. Solar irradiance reference spectra for two solar active levels. Advances in Space Research 34, 256–261.
Toon, O.B., Ragent, B., Colburn, D., Blamont, J., Cot, C., 1984. Large, solid particles in the clouds of Venus: Do they exist? Icarus 57, 143–160.
Toon, O.B., Turco, R.P., Hamill, P., Kiang, C.S., Whitten, R.C., 1979. A one-dimensional model describing aerosol formation and evolution in the stratosphere: II. sensitivity studies and comparison with observations. Journal of the Atmospheric Sciences 36, 718–736.
Traub, W.A., Carleton, N.P., 1974. Observations of O_2, H_2O and HD in planetary atmospheres, in: Exploration of the planetary system. Springer, pp. 223–228.
Trauger, J., Lunine, J., 1983. Spectroscopy of molecular oxygen in the atmospheres of Venus and Mars. Icarus 55, 272–281.
Trolier, M., Mauldin, R.L., Ravishankara, A.R., 1990. Rate coefficient for the termolecular channel of the self-reaction of chlorine monoxide. The Journal of Physical Chemistry 94, 4896–4907.
Tsang, W., Hampson, R.F., 1986. Chemical kinetic data base for combustion chemistry. part I. methane and related compounds. Journal of Physical and Chemical Reference Data 15, 1087–1279.
Vandaele, A.C., Hermans, C., Fally, S., 2009. Fourier transform measurements of SO_2 absorption cross sections: II.: Temperature dependence in the 29 000 - 44 000 cm^{-1} (227 - 345 nm) region. Journal of Quantitative Spectroscopy and Radiative Transfer 110, 2115–2126.
Vandaele, A.C., Mahieux, A., Chamberlain, S., Ristic, B., Robert, S., Thomas, I.R., Trompet, L., Wilquet, V., Bertaux, J.L., 2016. Carbon monoxide observed in Venus atmosphere with SOIR/VEx. Icarus 272, 48–59.
Vehkamäki, H., Kulmala, M., Napari, I., Lehtinen, K.E.J., Noppel, M., 2003. Modelling binary homoheneous nucleation of water-sulfuric acid vapours: Parametrization for high temperature emissions. Environ. Sci. Technol. 107, AAC 3–1–AAC 3–10.
Vehkamäki, H., Kulmala, M., Napari, I., Lehtinen, K.E.J., Timmreck, C., Noppel, M., Laaksonen, A., 2002. An inmproved parametrization for acid-water nucleation rates for tropospheric and stratospheric conditions. J. Geophys. Res. .
Verwer, J.G., Simpson, D., 1995. Explicit methods for stiff ODEs from atmospheric chemistry. Applied Numerical Mathematics 18, 413–430.
Wilquet, V., Drummond, R., Mahieux, A., Robert, S., Vandaele, A.C., Bertaux, J.L., 2012. Optical extinction due to aerosols in the upper haze of Venus: Four years of SOIR/VEX observations from 2006 to 2010. Icarus 217, 875–881.
Wilquet, V., Fedorova, A., Montmessin, F., Drummond, R., Mahieux, A., Vandaele, A.C., Villard, E., Korablev, O., Bertaux, J.L., 2009. Preliminary characterization of the upper haze by SPICAV/SOIR solar occultation in UV to mid-IR onboard Venus Express. Journal of Geophysical Research: Planets 114.
Wilson, C.F., Guerlet, S., Irwin, P.G.J., Tsang, C.C.C., Taylor, F.W., Carlson, R.W., Drossart, P., Piccioni, G., 2008. Evidence for anomalous cloud particles at the poles of Venus. Journal of Geophysical Research: Planets 113.
Winick, J.R., Stewart, A.I.F., 1980. Photochemistry of SO_2 in Venus upper cloud layers. Journal of Geophysical Research: Space Physics 85, 7849–7860.
Wu, C.R., Yang, B., Chen, F., Judge, D., Caldwell, J., Trafton, L., 2000. Measurements of high-, room-, and low-temperature photoabsorption cross sections of SO_2 in the 2080 to 2950 Å region, with application to Io. Icarus 145, 289–296.
Yoshino, K., Cheung, A.C., Esmond, J., Parkinson, W., Freeman, D., Guberman, S., Jenouvrier, A., Coquart, B., Merienne, M., 1988. Improved absorption cross-sections of oxygen in the wavelength region 205–240 nm of the Herzberg continuum. Planetary and space science 36, 1469–1475.
Yoshino, K., Esmond, J., Parkinson, W., Ito, K., Matsui, T., 1996a. Absorption cross section measurements of water vapor in the wavelength region 120 to 188 nm. Chemical Physics 211, 387–391.
Yoshino, K., Esmond, J., Sun, Y., Parkinson, W., Ito, K., Matsui, T., 1996b. Absorption cross section measurements of carbon dioxide in the wavelength region 118.7 nm and 175.5 nm and the temperature dependence. Journal of Quantitative Spectroscopy and Radiative Transfer 50, 53.
Young, L.D.G., 1972. High resolution spectra of Venus: a review. Icarus 17, 632–658.
Yung, Y.L., DeMore, W.B., 1982. Photochemistry of the stratosphere of Venus: implications for atmospheric evolution. Icarus 51, 199–247.
Yung, Y.L., DeMore, W.B., 1998. Photochemistry of planetary atmospheres. Oxford University Press.
Zasova, L., Moroz, V., Linkin, V., Khatuntsev, I., Maiorov, B., 2006. Structure of the venusian atmosphere from surface up to 100 km. Cosmic Research 44, 364–383.
Zeleznik, F.J., 1991. Thermodynamics properties of the aqueous sulfuric acid system to 350K. J. Phys. Chem. Ref. Data 20, 1157–1200.
Zhang, X., Liang, M.C., Mills, F.P., Belyaev, D.A., Yung, Y.L., 2012. Sulfur chemistry in the middle atmosphere of Venus. Icarus 217, 714–732.

A. Evaluation of clouds physical properties

Evaluation of the surface tension θ_S.
The surface tension is described by the Eq. (A.1) where δW is the work to be provided in order to increase the surface of δS. The unit of θ_S is the J m^{-2}:

$$\theta_S = \frac{\delta \mathrm{W}}{\delta \mathrm{S}} \tag{A.1}$$

The range of temperatures in our model goes from 170 K at the top to 400 K at 40 km. We used data from Sabinina and Terpugow (1935), Morgan and Davies (1916), Hoffmann and Seeman (1960) and finally Myhre et al. (1998) for the evaluation of θ_S in a temperature range between 233 K and 323 K. Vehkamäki et al. (2002) gives the range of validity for their parametric equation of θ_S from 180 K to 323 K. In addition, Vehkamäki et al. (2003) extends this domain up to 400 K using another parameterized formula. The Table A.6 presents the functions used in our model to calculate the surface tension.

The variable x represent the weight ratio of sulfuric acid of the droplet $w_{H_2SO_4}$, ranging between 0 and 1.
Evaluation for $T < 305$K Vehkamäki et al. (2002)
$\theta_S(x,T) = a(x) + T\ b(x)$
$a(x) = 0.11864 - 0.11651\ x + 0.76852\ x^2 - 2.40909\ x^3 + 2.95434\ x^4 - 1.25852\ x^5$
$b(x) = -0.15709 \cdot 10^{-3}\ + 0.40102 \cdot 10^{-3}\ x - 2.3995 \cdot 10^{-3}\ x^2 + 7.611235 \cdot 10^{-3}\ x^3$ $-7.37386 \cdot 10^{-3}\ x^4 + 3.89722 \cdot 10^{-3}\ x^5$
Evaluation for $305\text{K} \leq T \leq 400$K Vehkamäki et al. (2003). The variable x_m represent the molar ratio of sulfuric acid in the droplet, ranging between 0 and 1.
$\theta_S(x_m,T) = (a(x_m) + T_1\ b(x_m))\ {T_1}^{1.256}$
$T_1(x_m,T) = 1 - {}^{T}/_{T_c}$
Where T_c is the pseudo-critical temperature of the binary solution (H_2O, H_2SO_4):
$T_c(x_m) = 647.15(1 - x_m)^2 + 900.0\ x_m^2 + 3156.186\ x_m\ (1 - x_m)$
With the coefficients $a(x)$ and $b(x)$:
$a(x_m) = 0.2358 - 0.529\ x_m + 4.073\ {x_m}^2 - 12.6707\ {x_m}^3 + 15.3552\ {x_m}^4 - 6.3138\ {x_m}^5$
$b(x_m) = -0.14738 + 0.6253\ x_m - 5.4808\ {x_m}^2 + 17.2366\ {x_m}^3 - 21.0487\ {x_m}^4 + 8.719\ {x_m}^5$

Table A.6: Evaluation of the surface tension θ_S, in $\mathrm{J\,m^{-2}}$

Evaluation of the density ρ_d.
The density ρ_d of the binary solution droplet (H_2O, H_2SO_4) depends on the temperature and fraction of sulfuric acid. We have adopted the parameterisation of Vehkamäki et al. (2002) which uses the data from National Research Council (1928) and Myhre et al. (1998). It is then a parameterized formula that takes into account the whole range of sulfuric acid fraction and extends the temperature from 220 K to 373 K. The Table A.7 describes the parameterization adopted in our model.

The variable x represent the weight ratio of sulfuric acid of the droplet $w_{H_2SO_4}$, ranging between 0 and 1. T is the atmospheric temperature in K.
$\rho_d(x,T) = a(x) + b(x)\ T + c(x)\ T^2$
$a(x) = 0.7681724 + 2.1847140\ x + 7.163002\ x^2 -$ $44.31447\ x^3 + 88.75606\ x^4 - 75.73729\ x^5 + 23.43228\ x^6$
$b(x) = 1.808225 \cdot 10^{-3} - 9.294656 \cdot 10^{-3}\ x -$ $0.03742148\ x^2 + 0.2565321\ x^3 - 0.5362872\ x^4 + 0.4857736\ x^5 - 0.1629592\ x^6$
$c(x) = -3.478524 \cdot 10^{-6} + 1.335867 \cdot 10^{-5}\ x + 5.195706 \cdot 10^{-5}\ x^2 - 3.717636 \cdot 10^{-4}\ x^3 +$ $7.990811 \cdot 10^{-4}\ x^4 - 7.458060 \cdot 10^{-4}\ x^5 + 2.58739 \cdot 10^{-4}\ x^6$
Vehkamäki et al. (2002) use of data from National Research Council (1928) and Myhre et al. (1998).

Table A.7: Evaluation of ρ_d, density of the calculated mixture (H_2O, H_2SO_4) of the droplet, in $\mathrm{g\,cm^{-3}}$.

Evaluation of the saturation vapour pressure of $H_2O_{(g)}$ over a planar liquid sulfuric acid surface, $p_{sat\,H_2O}$.
The Kelvin equation (7) needs the value of the saturated vapour pressure of water, $p_{sat\,H_2O}$. It is expressed thanks to the empirical formula derived from Gmitro and Vermeulen (1964) which uses thermodynamic properties from Giauque et al. (1960). The Table A.8 presents the formula used in the model.

B. Sedimentation flux evaluation

Using the definition for the condensed mass per volume of air with the log-normal law and the Stokes velocity, we then obtain the following expression for the instantaneous sedimentation flux F_{sed}:

$$F_{sed} = \frac{8}{27}\pi\rho_d(\rho_d - \rho_f)\frac{g}{\eta}\int_0^\infty R^5 \left(1 + 1,246\frac{\lambda}{R} + 0,42\frac{\lambda}{R}\ \exp\left(-0,87\ \frac{R}{\lambda}\right)\right) n_N(R)dR \tag{B.1}$$

General expression used
$\ln(\mathrm{p}_{sat\,\mathrm{H_2O}}) = A\ln(298/T) + B/T + C + DT$
With cœfficients:
$A = -3.67340 + {}^{1}/_{R}(C_\mathrm{p} - 298.15\alpha)$
$B = -4143.5 + {}^{1}/_{R}(L - 298.15C_\mathrm{p} + {}^{298.15^2}/_{2\alpha})$
$C = 10.24353 + {}^{1}/_{R}(C_\mathrm{p} + {}^{(F-L)}/_{298.15})$
$D = 0.618943 \cdot 10^{-3} - {}^{\alpha}/_{(2\cdot R)}$
Where:
T the temperature in K
R the perfect gas constant in $\mathrm{J\,mol^{-1}\,K^{-1}}$
And the other physical quantities interpolated from (Giauque et al., 1960)
are functions of $w_{\mathrm{H_2SO_4}}$
C_p the specific heat in $\mathrm{cal\,mole^{-1}\,K^{-1}}$
F the Helmotz free energy
L the partial molar enthalpy similar to the reaction enthalpy in $\mathrm{cal\,mole^{-1}}$
α the cœfficient corresponding to the temperature of derivative C_p, in $\mathrm{cal\,mole^{-1}\,K^{-2}}$

Table A.8: Evaluation of $\mathrm{p}_{sat\,\mathrm{H_2O}}$, the saturation vapour pressure of H_2O over a planar surface of H_2SO_4, in Pa.

The integral term in Eq. (B.1) can be separated into a sum of three integral as follow:

$$\int_0^\infty \mathrm{R}^5\, n_\mathrm{N}(\mathrm{R})\mathrm{dR} = m_5 \tag{B.2a}$$

$$\int_0^\infty 1,246\,\lambda\,\mathrm{R}^4\, n_\mathrm{N}(\mathrm{R})\mathrm{dR} = 1,246\,\lambda\, m_4 \tag{B.2b}$$

$$\int_0^\infty 0,42\,\lambda\,\mathrm{R}^4\, \exp\left(-0,87\,\frac{\mathrm{R}}{\lambda}\right) n_\mathrm{N}(\mathrm{R})\mathrm{dR} = \text{Unresolvable} \tag{B.2c}$$

The difficulty here comes from the exponential term in the Eq. (B.2c). We use a Taylor expansion in order to get terms in the form of power of R that we can evaluate. We use a third order one for accuracy purpose. We didn't deeply test the influence of order on the accuracy of the results since the third order provided results with a low relative error against highly accurate and computationally intensive discrete integral algorithm (see Stolzenbach (2016)). It goes as follow, with $c = {}^{0,87}/_{\lambda}$:

$$\begin{aligned}\exp(-c\mathrm{R}) \approx\ & \exp(-c\mathrm{R}^\star) - c\exp(-c\mathrm{R}^\star)(\mathrm{R}-\mathrm{R}^\star)\\ & + \frac{c^2}{2}\exp(-c\mathrm{R}^\star)(\mathrm{R}-\mathrm{R}^\star)^2\\ & - \frac{c^3}{6}\exp(-c\mathrm{R}^\star)(\mathrm{R}-\mathrm{R}^\star)^3 + o\left((\mathrm{R}-\mathrm{R}^\star)^4\right)\end{aligned}$$

Where $\mathrm{R}^\star$ is the value of R where we evaluate the Taylor expansion. We then get the approximation for $v_{st}(\mathrm{R})\cdot\mathrm{R}^k$

with $a = 1,246 \cdot \lambda$, $b = 0,42 \cdot \lambda$ and $c = {}^{0,87}/_{\lambda}$:

$$
\begin{aligned}
& v_{st}(\mathrm{R}) \cdot \mathrm{R}^k \approx \frac{2\,g\,(\rho_d - \rho_f)}{9\,\eta} \cdot \\
& \Bigg[\mathrm{R}^{1+k} \cdot \underbrace{\left(a + b\,\exp(-c\mathrm{R}^\star)\,\left(1 + c\,\mathrm{R}^\star + \frac{c^2}{2}\mathrm{R}^{\star\,2} + \frac{c^3}{6}\mathrm{R}^{\star\,3}\right)\right)}_{\text{Coefficient } A_1} \\
& + \mathrm{R}^{2+k} \cdot \underbrace{\left(1 - b\,\exp(-c\mathrm{R}^\star)\,\left(c + c^2\,\mathrm{R}^\star + \frac{c^3}{2}\mathrm{R}^{\star\,2}\right)\right)}_{\text{Coefficient } A_2} \\
& + \mathrm{R}^{3+k} \cdot \underbrace{\left(b\,\exp(-c\mathrm{R}^\star)\,\left(\frac{c^2}{2} + \frac{c^3}{2}\,\mathrm{R}^\star\right)\right)}_{\text{Coefficient } A_3} \\
& + \mathrm{R}^{4+k} \cdot \underbrace{\left(-b\,\exp(-c\mathrm{R}^\star)\,\left(\frac{c^3}{6}\right)\right)}_{\text{Coefficient } A_4} \Bigg]
\end{aligned}
$$

That can be rewritten as:

$$
v_{st}(\mathrm{R}) \cdot \mathrm{R}^k \approx \frac{2\,g\,(\rho_d - \rho_f)}{9\,\eta} \cdot \sum_{i=1}^{4} A_i\,\mathrm{R}^{i+k} \tag{B.3}
$$

We know all the terms in Eq. (B.3) and the sedimentation flux defined by the Eq. (B.1) can also be rewritten using Eq. (B.3):

$$
\begin{aligned}
F_{sed} &\approx \frac{8}{27}\pi\,\frac{\rho_d}{\eta}\,(\rho_d - \rho_f)\,\sum_{i=1}^{4} A_i\,\int_0^\infty \mathrm{R}^{i+3}\,n_{\mathrm{N}}(\mathrm{R})\mathrm{dR} \\
&\approx \frac{8}{27}\pi\,\frac{\rho_d}{\eta}\,(\rho_d - \rho_f)\,\sum_{i=1}^{4} A_i\,m_{i+3} \\
&\approx \frac{8}{27}\pi\,\frac{\rho_d}{\eta}\,(\rho_d - \rho_f)\,\mathrm{N}\,\sum_{i=1}^{4} A_i\,\overline{\mathrm{R}}_g^{\,i+3}\,\exp\left(\frac{1}{2}(i+3)^2\,\ln^2\sigma_g\right)
\end{aligned} \tag{B.4}
$$

The Eq. (B.4) allows us to evaluate the sedimentation flux, and generally every moment's instantaneous flux of the log-normal law, for each mode i, $\mathrm{F}_{sed\,i}$, of the radius size distribution and the total flux, $\mathrm{F}_{sed\,tot}$, by adding them together:

$$
\mathrm{F}_{sed\,tot} = \sum_{i=1}^{j} \mathrm{F}_{sed\,i} \tag{B.5}
$$

The part of $\mathrm{F}_{sed\,tot}$ allocated to the sulfuric acid $\mathrm{F}_{sed\,\mathrm{H_2SO_{4(l)}}}$ and water $\mathrm{F}_{sed\,\mathrm{H_2O_{(l)}}}$ are straightforwardly determined by $w_{\mathrm{H_2SO_4}}$:

$$
\mathrm{F}_{sed\,\mathrm{H_2SO_{4(l)}}} = w_{\mathrm{H_2SO_4}} \cdot \mathrm{F}_{sed\,tot} \tag{B.6a}
$$

$$
\mathrm{F}_{sed\,\mathrm{H_2O_{(l)}}} = (1 - w_{\mathrm{H_2SO_4}}) \cdot \mathrm{F}_{sed\,tot} \tag{B.6b}
$$

These terms are included in the tendency equations of the tracers $\mathrm{H_2O_{(l)}}$ and $\mathrm{H_2SO_{4(l)}}$ calculated by the Venus PCM. This method provides information of the cloud characteristics directly linked with the photochemical model and the Venus PCM with a degree of sophistication that no previous photochemical model has reached.